Hall A Status Report - 2008

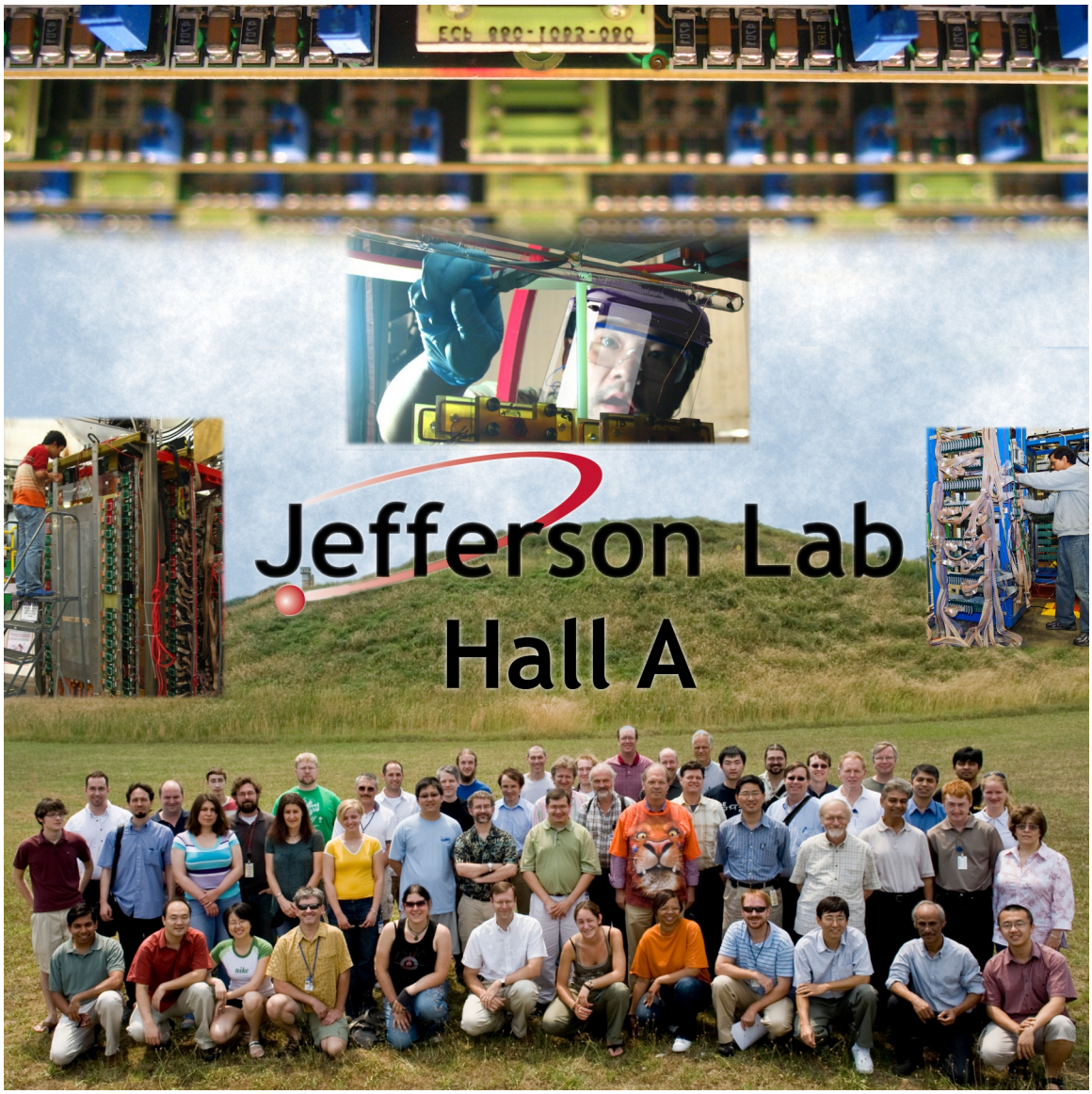

Edited by Kees de Jager and Bryan Moffit
Cover Art by Elena Long

Contents

List of Figures

List of Tables

1 Introduction

In 2008 essential progress was made with the research program in Hall A with the 12 GeV upgrade. For the SuperBigBite (SBS) project a Conceptual Design Report was written in preparation for a Technical Review. The, in general favorable, report of this review was used to support an MRI funding request to NSF, that has been submitted by Norfolk State University, the University of Virginia and the College of William and Mary. In parallel, three proposals were submitted to PAC34 to augment the measurement of the proton form factor that was approved as experiment E12-07-019 by PAC32. If the necessary funding is approved by NSF and in addition by DOE, this project will provide additional instrumentation for Hall A that will allow to perform in an open detector geometry at high luminosity a set of experiments at the core of the 12 GeV research program. Two proposals were submitted to PAC34 to study parity violation in electron scattering, each with a large dedicated set-up. One proposes to measure the parity-violating asymmetry A_{PV} in the scattering of longitudinally polarized 11 GeV electrons from the atomic electrons in a liquid hydrogen target (Møller scattering). A_{PV} is predicted to be 35.6 parts per billion (ppb) at the proposed kinematics. The goal is to measure A_{PV} to a precision of 0.73 ppb, using a dedicated redesigned upgrade of the E158 SLAC instrumentation. The other proposes to measure A_{PV} in the deep-inelastic scattering of polarized electrons (PVDIS) to high precision in order to search for physics beyond the Standard Model in lepton-quark neutral current interactions. The proposed accuracy will improve our knowledge of axial-hadronic currents by well over an order of magnitude. In order to perform such a precise test, possible novel hadronic physics, such as the violation of charge symmetry (CSV) at the quark level and the contributions from higher-twist operators, must be addressed. In this proposal, a design of a new spectrometer, called SoLID is presented, that is based on a large solenoidal magnet, with a resolution and luminosity that will provide the precision necessary for this broad program of electroweak studies. Both PV proposals require upgraded polarimetry at the level of 0.5%.

In the first half of January we completed the running for E05-110, the Coulomb Sum Rule experiment. Then, after installing specially configured lead targets, a series of tests were performed for the lead-parity experiment, E06-002, and some additional data were taken for E06-007, proton knock-out from ^{208}Pb. In February and March the BigBite spectrometer was successfully installed with the hadron detector package to allow running E04-007, a precision measurement of π^0-production on the proton near threshold. After replacing the hadron detector package with the electron package within a week in early May, the first part of E08-007, a highly accurate measurement of the proton form-factor ratio G_E^p/G_M^p at low Q^2-values was completed.

During the summer, early June through late September, preparations were made that were required to run E06-010, a measurement of transversity of the neutron through semi-inclusive pion (and kaon) production. The main component of the installation was of course the polarized ^{3}He target set-up. Through the use of a high-power narrow-band laser diode array the target polarization was further improved to close to 70% with a 15 μA beam through the target cell. In addition a gas Cerenkov detector was added to the BigBite detector package, specially designed for the upcoming d_2^n experiment and an upgraded version of the RICH detector was installed in the HRS-L focal plane. The transversity experiment then ran smoothly through the end of the year.

I would like to recognize the expertise, dedication and just plain hard work that made all this possible, by the design and engineering staff, Al Gavalya, Susan Esp, Joyce Miller, Macon Hodges and Paul Brindza and the technical staff, Ed Folts, Jack Segal, Heidi Fansler, Scot Spiegel, Todd Ewing and Gary Dezern.

2 Standard Hall A Facilities

2.1 Polarized ^{3}He Target

Status Report on the Polarized ^{3}He Target

Contributed by J. P. Chen for the polarized He3 group

The Hall A polarized ^{3}He target [1] was successfully used for experiments E94-010 [2] and E95-001 [3], E99-117 [4], E97-103 [5], E01-012 [6], E97-110 [7] and E02-013 [8]. It is current being used for the transversity (E06-010) [10] experiment.

The polarized ^{3}He target initially used optically pumped Rubidium vapor to polarize ^{3}He nuclei via spin exchange. Typical in-beam (10-15 μA) polarization steadily increased from 30% to over 40%. A new hybrid technique for spin-exchange which uses a K-Rb mixture [9] increased the in-beam polarization to over 50% (close to 60% without beam), due to the much higher K-^{3}He spin exchange efficiency. The new hybrid cells also achieved significantly shorter spin-up times (5 hours compared to 10 hours for pure Rb cell). Further improvement in polarization was achieved recently for the transversity experiment by using the recently available Comet high-power narrow-width diode lasers instead of the Coherent broad-width diode lasers that have been used in the previous experiments. The target polarization improved significantly to 65% with 12 μA beam and 20-minute spin-flip, and over 70% without beam (see figure 2).

The earlier experiments used two sets of Helmholtz coils which provided a 25 Gauss holding field for any direction in the scattering (horizontal) plane. The transversity experiment also needs vertical polarization. A third set of coils provide the field in this direction. These three sets of coils allow polarization in any direction in 3-d space. Target cells were up to 40 cm long with density of about 10 amg (10 atm at 0°). Beam currents on target ranged from 10 to 15 μA to keep the beam depolarization effect small and the cell survival time reasonably long ($>$ 3 weeks). The luminosity was about 10^{36} nuclei/s/cm^2. Two kinds of polarimetry, NMR and EPR (Electron-Paramagnetic-Resonance), were used to measure the polarization of the target. The uncertainty achieved for each method is 3% relative and the methods agree well within errors.

Fast target spin reversals are needed for the Transversity experiment (every 20 minutes). The fast spin reversal was achieved with Adiabatic Fast Passage (AFP) technique. The polarizing laser spin direction reversal was accomplished with rotating 1/4-wave plates. The polarization loss due to fast spin reversal is less than 10% relative depending on the AFP loss and the spin up time. The improvement of spin up time with the hybrid cell has significantly reduced the polarization loss due to the fast spin reversal. With the BigBite magnet nearby (1.5 m) and a large shielding plate, the field gradients are at the level of 20-30 mg/cm, which is about a factor of 2 larger than that without the BigBite magnet. These field gradients lead to about $0.5 - 0.7$% AFP loss. Correction coils could reduce the field gradients. However, it was found that when the field gradients reduced to less than 20 mg/cm, masing effects [11] started which caused significantly drop in the target polarization (from 70% to $<$ 60%). We had to leave the field gradients high by tuning off the correction coils to avoid the masing effect.

Most of the target components went through an upgrade for the transversity experiment and the subsequent experiments (d_2^n [12], A_y^n [13], $(e, e'd)$ [14]). The design group (Al Gavalya, Susan Esp et al.) worked over a year to ensure the upgraded system satisfy the stringent requirements of the experiments within a very tight space constraints. With a lot of hard work of a dedicated group of students, postdocs (C. Dutta, J. Huang, J. Katich, Y. Qiang, Y. Zhang) and other people, the new target system works very reliably. The oven system works stably at the high temperature of 230° required for the hybrid optical pumping. The new spin-flip and 3-d rotation control system works flawlessly. The new NMR system added features of automatic NMR at the pumping chamber

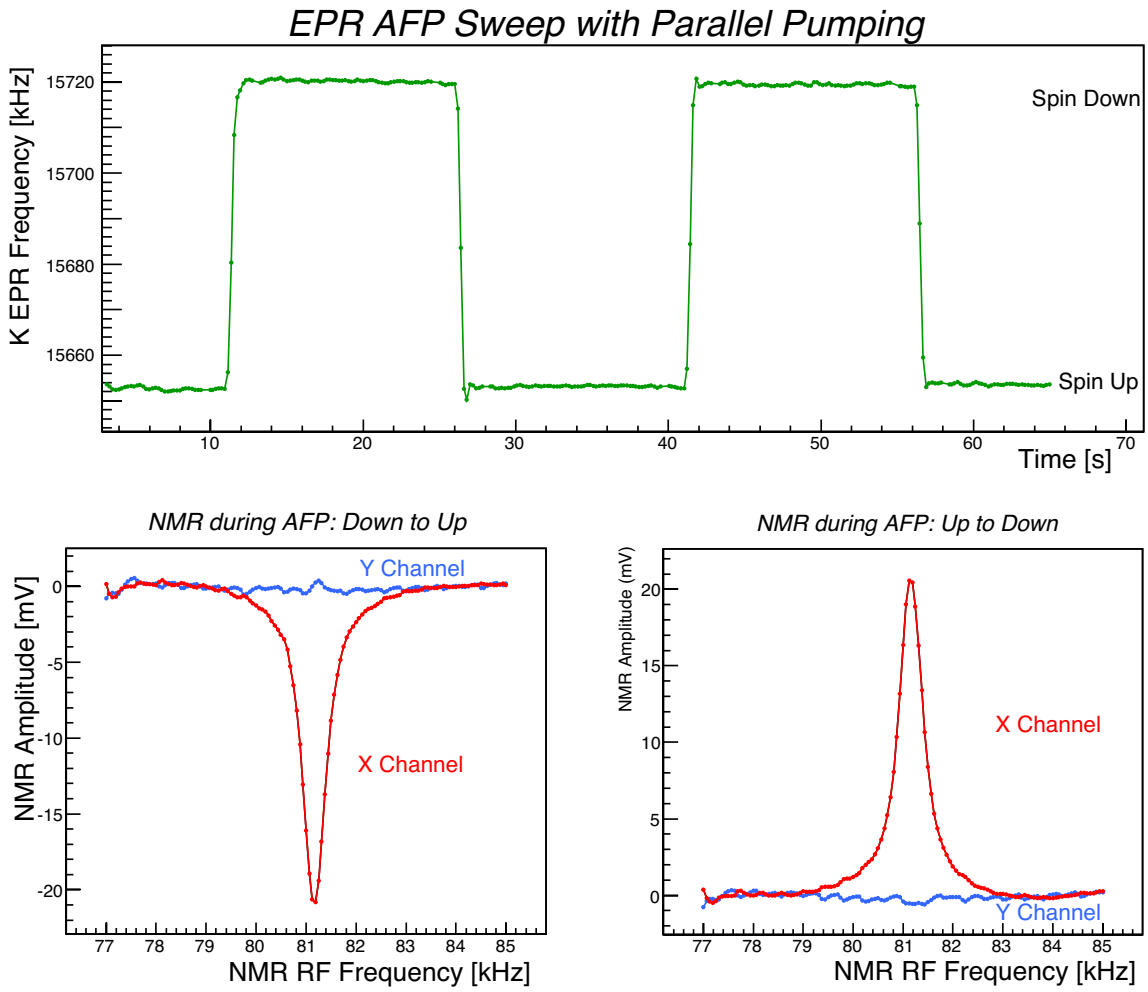

Figure 1: Typical NMR and EPR signals during the transversity experiment.

during spin-flip. The new EPR system initially had a problem of not enough RF power due to the increased distance from the EPR RF coil to the pumping cell. By moving the EPR RF coil to be very close to the pumping cell, the new EPR system works very well. Figure 1 shows typical NMR and EPR signals. The preliminary analysis of the EPR measurements show that the results reached 3% precision already. It may be further improved with off-line analysis. Two NMR water calibrations were performed right before the transversity experiment started. However, due to a target ladder problem, the pick-up coils were moved after the water calibrations. New water calibrations are planned during the Christmas-New Year down time and after the completion of the experiments. The polarimetry results were cross-checked with a measurement of the e-^{3}He elastic asymmetry. A preliminary analysis of the elastic asymmetry showed an agreement with the target polarization analysis at a level of about 5%.

To accommodate all four experiments with minimum change-over, a number of modifications and upgrades were implemented in the new design, including six optics line (two for each polarizing direction) and a compact layout in the pivot area. Total of fifteen long optical fibers connect the lasers from the upstairs laser room to the hall. Three 5-to-1 optical fiber combiners and the new laser optics system allow optical pumping for 3 directions (longitudinal, transverse and vertical)

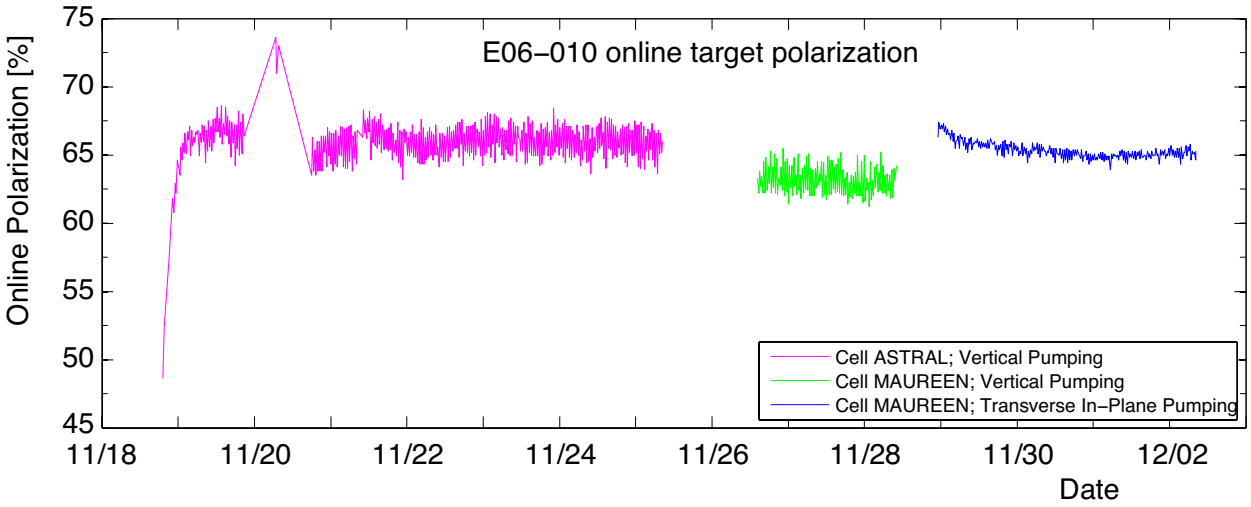

Figure 2: The polarized ^{3}He target performance with 12 μA and spin-flip during the transversity experiment. The rise in the middle corresponds to the time when beam was off.

with minimum change-over time. Changing over from the first direction to the second direction can be accomplished remotely without access into the hall. However, to change to the third direction, an access is needed to change connecting fibers and optics setup. For each pumping direction, 3 higher-power (30 W) diode lasers are used. In addition to the existing ten Coherent (broad-width) lasers, three new Comet (narrow-width) lasers were purchased right before the transversity experiment started. The laser beam is polarized after passing through a set of polarizing optics. It then gets reflected into the pumping cell by two mirrors. For transverse and vertical pumping directions, the two mirrors are in a polarization preserving configuration. However, they are not in this condition for the longitudinal direction (which is required for the d_2^n and $(e, e'd)$ experiments). A possible solution is to purchase polarization preserving mirrors, which are usually expensive and difficult to manufacture. A solution was found and tested by using two 1/4-wave plates pre-tuned in front of the two mirrors to compensate the phase change. This solution was tested to work very well for the Comet laser due to it's narrow-width spectrum.

About 18 cells were manufactured by the William and Mary and the UVa groups with glass cells supplied by by a glass blower from Princeton University. Because the thick pull-off blocks laser light, each cell can accommodate two directions of optical pumping. Nine cells are for transverse and vertical pumping (for the transversity and the A_y experiments) and the other nine are for longitudinal and transverse (for the d_2^n and the ^{3}He$(e, e'd)$ experiments). Initial tests with Coherent lasers (broad-width) showed that most of the cells have polarizations around 50% with maximum reached 60%. New tests on a few cells with Comet lasers (narrow-width) showed significant (20% relative) improvement in polarization, reached 70% without beam. Two cells used in transversity running reached 65% polarization with 12 μA beam and spin-flip (see figure 2).

A compass system developed by the University of Kentucky group is being used to measure both vertical and transverse field directions. The performance has reached designed goal.

References

[1] http://hallaweb.jlab.org/targets/polhe3/polhe3_tgt.html;
and tech notes in http://www.jlab.org/e94010/.

[2] M. Amarian *et al.*, Phys. Rev. Lett. 89, 242301 (2002); 92, 022301 (2004); 93, 152301 (2004); Z. Meziani,*et al.*, Phys. Lett. B 613, 148 (2005).

[3] W. Xu, *et al.*, Phys. Rev. Lett. 85, 2900 (2000); F. Xiong, *et al.*, Phys. Rev. Lett. 87, 242501 (2001).

[4] X. Zheng, *et al.*, Phys. Rev. Lett.92, 012004 (2004); Phys. Rev. C 70, 065207 (2004).

[5] K. Kramer, *et al.*, Phys. Rev. Lett. 95, 142002 (2005).

[6] P. Solvignon, *et al.*, Phys. Rev. Lett. 101, 182502 (2008).

[7] JLab E97-110, Spokespersons, J. P. Chen, A. Deur and F. Garibaldi.

[8] JLab E02-013, Spokespersons, G. Cates, N. Liyanaga and B. Wojtsekhowski.

[9] E. Babcock, *et al.*, Phys. Rev. Lett. 91, 123003 (2003).

[10] JLab E06-010/E06-011 Spokespersons, J. P.Chen, E. Cisbani, H. Gao, X. Jiang and J. C. Peng.

[11] M. V. Romalis, Ph. D thesis, Princeton University (1998).

[12] JLab 06-014, Spokespersons, S. Choi, X. Jiang, Z.-E. Meziani, B. Sawatzky.

[13] JLab E05-015, Spokespersons, T. Averett, J. P. Chen and X. Jiang.

[14] JLab E05-102, Spokespersons, S. Gilad, D. Higinbotham, W. Korsch, B. Norum, S. Sirca.

2.2 Compton Polarimeter Upgrade

The Compton Polarimeter Upgrade

Contributed by Sirish Nanda

2.2.1 Overview

The Hall A Compton Polarimeter provides electron beam polarization measurements in a continuous and non-invasive manner via Compton scattering of polarized electrons from polarized photons trapped in a Fabry-Perot cavity. A schematic layout of the Compton polarimeter is shown in Fig.3. The electron beam is transported through a vertical magnetic chicane consisting of four dipole magnets. At present, a high-finesse Fabry-Perot cavity injected by a 240 mW, 1064 nm infrared laser serves as the photon target. Intra-cavity power remains stable at about 500 W. The Compton back-scattered photons are detected in an electromagnetic calorimeter consisting of lead tungstate crystals. The recoil electrons, separated from the primary beam by the fourth dipole of the chicane are detected in a silicon micro-strip detector. The electron beam polarization is deduced from the counting rate asymmetries of the detected particles.

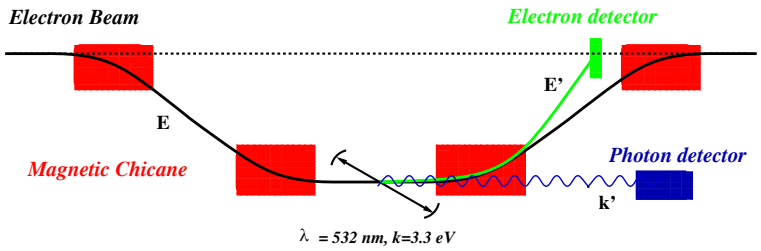

Figure 3: Schematic layout of the Hall A Compton polarimeter.

2.2.2 Upgrade

A performance upgrade of the Compton Polarimeter, in accordance with the conceptual design report [1], is presently under implementation. The upgrade is motivated by upcoming high accuracy experiments with very demanding requirement on the beam polarization. Defining k as the photon energy and E as the electron beam energy, the Figure Of Merit (F.O.M.) of a Compton measurement scales with $k^2 \times E^2$, making high accuracy polarimetry a real challenge at low energy. The proposed upgrades are thus driven by the requirement of the Lead Parity experiment [2] of 1% relative accuracy at 850 MeV. The present infra-red system, while capable of achieving such accuracies at higher energy ($\geq$ 6 GeV), falls far short at lower energies. We plan to upgrade the existing Fabry-Perot cavity operating at 1064 nm (IR) with about 1.5 kW power to a 532 nm (green) cavity with similar power.

In addition, improvements to the electron detector and photon calorimeter combined with the development of a new integrated method shows promise of absolute accuracies approaching 1% at 0.85 GeV beam energy. The main parameters of the green Compton upgrade are shown in Table.1

The conceptual design of the green Compton polarimeter utilizes much of the design philosophy and the existing infrastructure of the present Compton polarimeter. In the following, the subsystems under upgrade are described.

Parameter	Present	Upgrade
Wavelength (nm)	1064	532
Cavity Power (W)	1500	1500
Cavity Q	1.0×10^{11}	1.8×10^{11}
FOM (σ.A^2) @.85GeV	0.57	2.2
Energy Range (GeV)	2 - 6	0.8 - 6
$\delta P_e/P_e$ @.85GeV	-	1%

Table 1: Main design parameters of the green Compton polarimeter upgrade compared to the present infra-red system.

2.2.3 Electron Detector

The electron detector upgrade is being carried out by Laboratoire de Physique Corpusculaire IN2P3/Université Blaise Pascal, Clermont-Ferrand. The new detector has 4 planes of 192 silicon micro-strip with 240 μm pitch. The expected resolution is about 100 μm. A high precision vertical motion of 120 mm for the detector has been incorporated to the design so as to facilitate covering the recoil electrons corresponding to the Compton edge over a broad range of energies. Motion control system as well as remote control computer interfaces for the detector have been successfully developed by the EPICS group . Illustrated in Fig. 4 is the electron detector silicon micro-strip assembly. The electron detector as well as its support structure and vacuum chamber

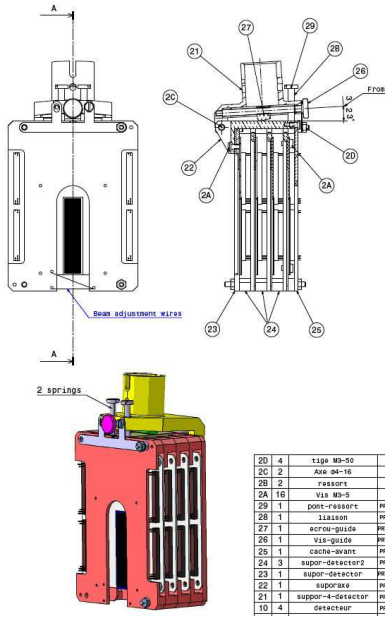

Figure 4: The new electron detector silicon micro-strip assembly.

were fabricated and later assembled at Clermont-Ferrand in early 2008. The package was delivered to Jefferson Lab in summer 2008. Installation of the new detector in the Hall A beam line was carried out by a team visiting from Clermont-Ferrand and Jefferson Lab engineering services group during August-September 2008. Fiducialization of the detector with respect to the vacuum

chamber and alignment of the detector chamber was carried out by the Jefferson lab survey and alignment group. The new installation successfully completed vacuum test and basic electronics signal checkout in October 2008. The CEBAF electron beam was successfully transported through the Compton chicane at 5.9 GeV through the new installation.

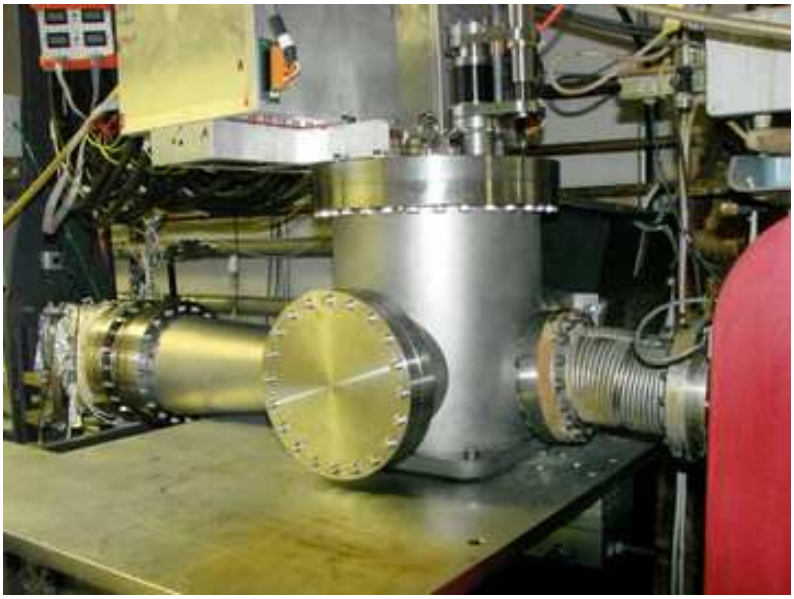

Figure 5: The new electron detector installed in Hall A beam line.

Commissioning of the electron detector is in progress. Alexander Camsonne is in the process of developing CODA interface to the new ETROC trigger module supplied by Clermont-Ferrand. Analysis software for the electron detector is under implementation by Richard Holmes, Syracuse University.

2.2.4 Photon Detector

The new photon detector consists of a single GSO crystal, 60 mm in diameter and 150 mm in length. The GSO crystal was delivered by Hitachi Chemicals Ltd. to Carnegie Mellon University (CMU) in March 2008. The compete photon calorimeter as shown in Fig. 6, was put together at CMU lead by Gregg Franklin. During the summer of 2008, the calorimeter was tested at the HIGS facility of the Free Electron Laser Lab at Duke University. Absolute energy calibration of the calorimeter was performed over a range of photon energies from 2 to 20 MeV at HIGS. Better than 2% energy resolution was obtained with the calorimeter.

The GSO calorimeter was installed in Hall A beam line in November 2008. Commissioning of the detector with the existing Compton Polarimeter DAQ in counting mode, as well as the Flash ADC based integrating DAQ is in progress. Preliminary spectrum of Compton scattered photons from 5.9 GeV polarized electron beam obtained with the detector is shown in Fig. 7. The spectrum shows a sharp Compton edge indicative of the high energy resolution of the new detector. Spin asymmetry as a function scattered photon energies are shown in Fig. 8. The red and blue points are for right-handed and left handed polarization of the laser beam while the green points are background data with the laser off. Data analysis is being carried out by Diana Parno, CMU and Richard Holmes, Syracuse U.

Figure 6: GSO Calorimeter assembled and tested at Carnegie-Mellon University.

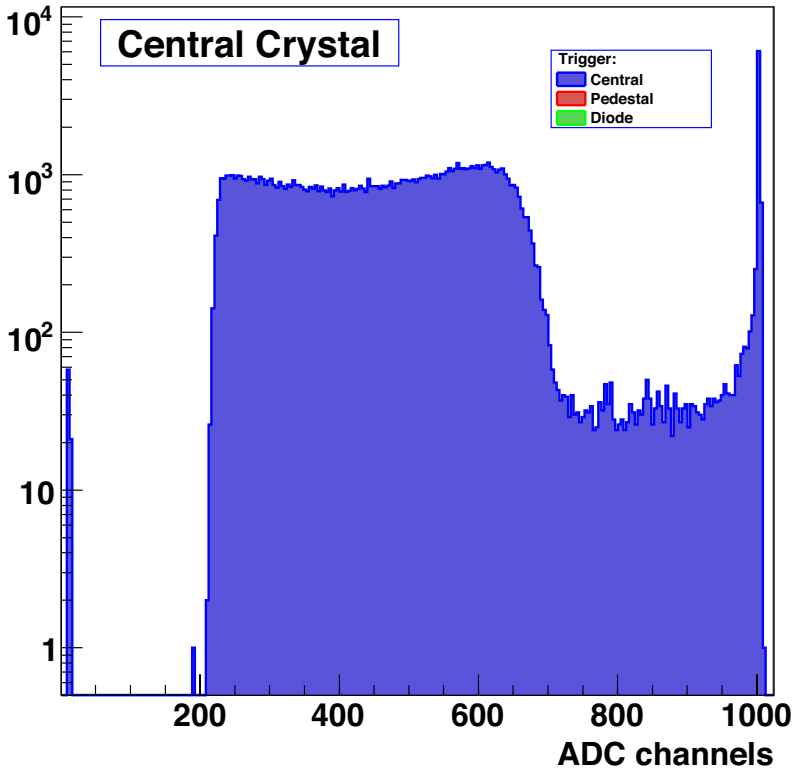

Figure 7: Compton scattering spectrum of 5.9 GeV electrons with the new GSO Calorimeter.

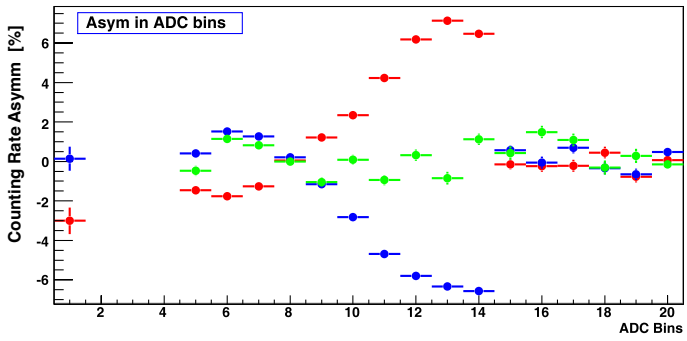

Figure 8: Asymmetry of Compton scattering measured with the GSO calorimeter at 5.9 GeV.

2.2.5 Fabry-Perot Cavity

A schematic layout of the optical setup for the upgrade is shown in Fig. 9. The heart of the upgrade plan is to replace the infrared cavity with a 532 nm green cavity fed by the new laser. Recent advances in the manufacturing of high reflectivity and low loss dielectric mirrors as well as availability of narrow line width green lasers facilitates the feasibility of our challenging design goal. High gain cavities at 532 nm have been successfully constructed by the PVLAS[3] group that has geometry and gain comparable to our proposed design here.

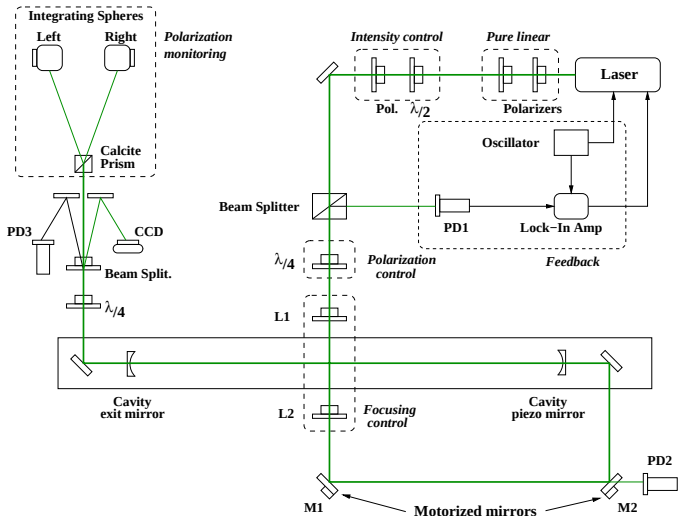

Figure 9: Optics table of the green Compton polarimeter.

Significant progress has been achieved in the development of the green Fabry-Perot cavity during 2008 with participation from Abdurahim Rakhman, graduate student from Syracuse University. Earlier in 2007 we were successful in lock acquisition with the stock CVI mirrors, Prometheus green laser, and the home-made Pound-Drever-Hall feedback servo system electronics system. However, cavity power was substantially below expectations due to high loss in the mirrors. This was attributed to lack of clean room conditions in the ARC laser lab.

In summer of 2008, a major effort was launched to convert the laser lab into a clean room. The

HVAC system for the room was modified to achieve positive pressure in the room. A clean tiled acoustic ceiling as well as HEPA fan filter units were installed in the lab. This led to achieving Class 1000 level environment for the whole lab. For cavity mirror handling, cleaning and storage, a class 100 clean bench was procured from Air Clean Systems. In addition, a portable soft-wall clean room with additional HEPA filter units were installed surrounding the optics table and the clean bench. This improved the environment in the optics table and cavity to better than Class 100. Illustrated in Fig. 10 is the new clean room environment of the laser lab.

Figure 10: Clean room setup in the Compton Polarimetry Lab.

New super-polished cavity mirrors substrates with better than 0.5 $\mathring{A}$ finish were ordered from General Optics in the Summer of 2008. Three sets of low loss HR at 532 nm coatings were also ordered. The transmittance of the three sets of mirrors was specified to be 50, 100, and 240 ppm with less than 10 ppm scattering and absorption loss. The new cavity mirrors were delivered to the Lab in October 2008. Shown in Fig. 11 is the measured data for surface roughness of the substrates as deviation from the specified surface over the central region of the mirror covering a circle of 1 mm in perimeter. The rms deviation was measured to be 0.2$\mathring{A}$, better than our specification. Transmittance of the 50 ppm mirrors as a function of wavelength is show in Fig. 12.

The 240 ppm mirrors were mounted in the cavity in November 2008. In order to improve the electronics noise figures experienced in the feedback servo electronics, Lawrence Lee, a summer student from Rutgers University, and Dan Sexton from Jefferson Lab FEL electronics group, participated in the enhancement of the Cavlock electronics. We successfully acquired lock on the TEM_{00} cavity mode. Illustrated in Fig. 13 is the oscilloscope traces of the cavity signals demonstrating the beginning of a lock sequence. The upper blue trace is the photodiode signal from laser power reflected from the cavity, the lower yellow curve is the photodiode signal from the laser power transmitted through the cavity, the red trace is the error signal fed back to the laser to sustain lock. As seen from these curves,there are some oscillations in the transmitted and reflected power. Work is in progress to further tune the Cavlock servo electronics to improve the stability of the lock. We measured the intra-cavity power to be 150 W with a gain of about 3000. While the mirrors performed quite well, the coupling efficiency to the cavity was not optimal. We are in the process

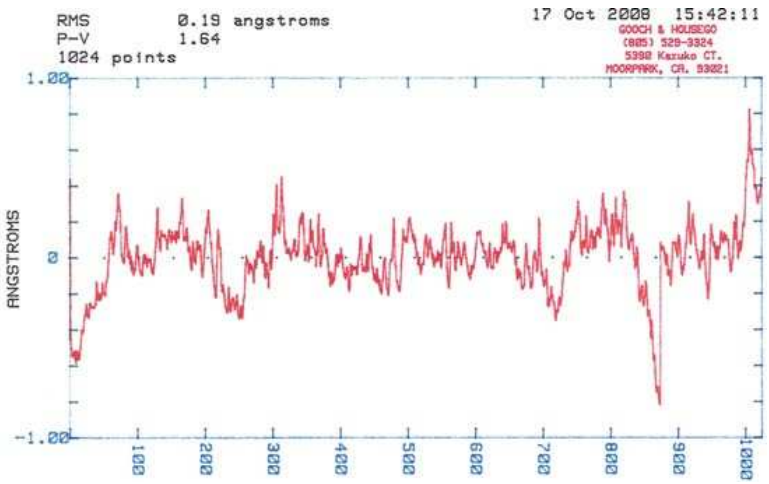

Figure 11: Surface deviation of the mirror substrates fabricated by General Optics.

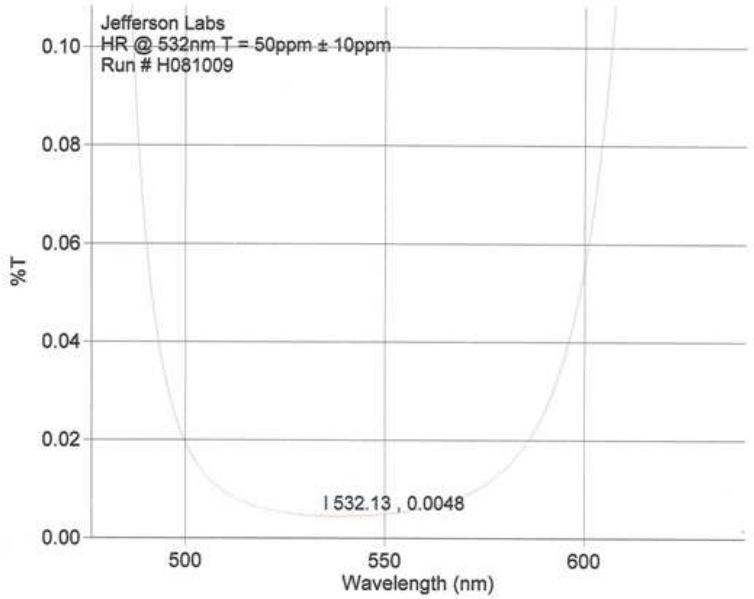

Figure 12: Transmittance of the high finesse GSI mirrors as a function of wavelength.

of tuning optics to enhance coupling efficiency.

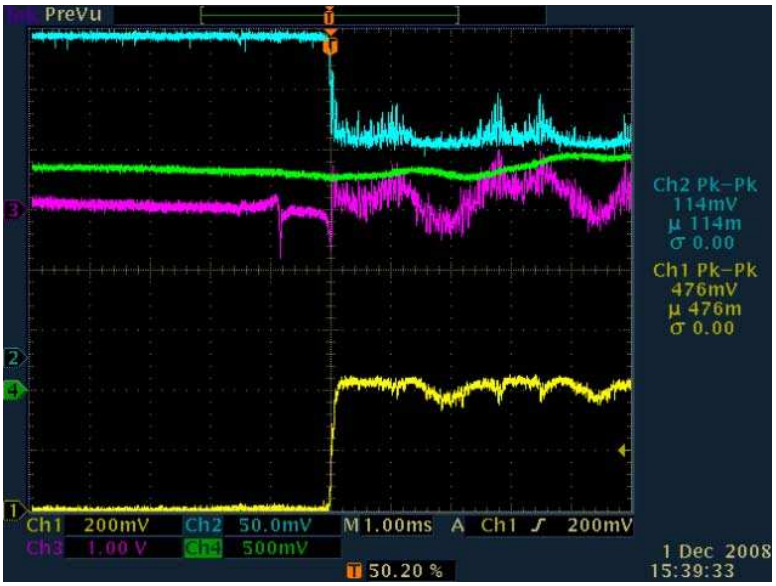

Figure 13: Scope trace of cavity lock acquisition with the GSI 240 ppm mirrors and the Prometheus laser.

2.2.6 Conclusion

We have demonstrated that the newly acquired GSI mirrors, the conversion of the laboratory to clean room environment, and improvements to locking electronics, high gain cavity performance is possible. We have also successfully coupled the IR beam of the Prometheus laser through a fiber to the IPG Ytterbium fiber amplifier to pump the PPLN crystal and produce more than 1 Watt of green power. Future plan include acquiring lock of this fiber amplified beam coupled to the GSI mirror cavity with higher cavity power levels.

References

[1] S. Nanda and D. Lhuillier, Conceptual Design Report for Hall A Compton Polarimeter Upgrade, Unpublished.

[2] Jlab Experiment E06002, Paul Souder (Syracuse), Robert Michaels (JLab), Guido Urciuoli (INFN) spokespersons.

[3] M. Bregant *et al.*, arXIV:hep-ex/0202046 v1 28 Feb 2002.

2.3 RICH Upgrade

Rich Upgrade

Contributed by Evaristo Cisbani

Successfully operated in the Hypernuclear Spectroscopy Experiment, the original Hall A Proximity Focusing RICH detector has been upgraded to provide an effective pion-kaon rejection at 2.4 GeV/c for the Transversity experiment [1].

The upgraded RICH reuses most of the original RICH (spare) parts. The photon detector surface has been enlarged from 0.77 to 1.3 m^2, in order to extend the proximity gap of $\sim$ 70%, without loosing photons, and consequently improve the Cherenkov angle reconstruction.

The relevant characteristics of the original (old) and upgrades (new) detectors are presented in table 2.

Table 2: The characteristics of the original (old) and upgraded RICH (new).

Component	Unit	Old	New	Detail
Proximity Gap	mm	100	159	Filled with Methane at STP
Pad Panels		3	5	
Photon Detector	m^2	0.77	1.3	Planar surface of pad panels
FE Electronics		11520	19200	Analog, multiplexed T&H
Radiator Thickness	mm	15		Liquid Freon (C_6F_{14}, n=1.29)
Photon converter	nm	300		CsI film coated on Pad Planes
Pad Panel Size	mm^2	645×403		Rotated by 90^o in new version
Pad Size	mm^2	8×8.4		

The photo-sensible CsI has been evaporated on the 5 pad panels in July 2008 at Stony Brook University where the INFN evaporation facility is now operated for the production of the Hadron Blind Detector components of the PHENIX experiment at BNL. The results of the evaporation is reported on fig. 15 for the 4th panel (the other 4 panels show comparable quality); the average measured quantum efficiency is at the level of 25%, few percent above the typical values obtained for the original RICH.

Each evaporated pad panel (which must be kept in dry atmosphere), has been stored in a dedicated chamber continuously flushed with inert gas. The compact multi-chamber storage system has been designed for the optimal on-ground transportation from Stony Brook to JLab.

The evaporated pad planes, the reused liquid radiator vessel and the new larger multiwire chamber have been assembled at JLab inside the controlled atmosphere of the existing glove box.

Cosmics data have been acquired in the EEL building to verify the functionality of the multiwire proportional chamber and related electronics.

The tested detector has been installed in the HRS detector stack in October 2008 and connected to the liquid freon recirculation and the CH_4 gas systems.

The very first observed ring is presented in fig. 16.

Detailed calibration and characterization are in progress.

References

[1] E. Cisbani *et al.*, *"Upgrade of the proximity focusing RICH at JLab"*, NIM A596 (2008) 44-46

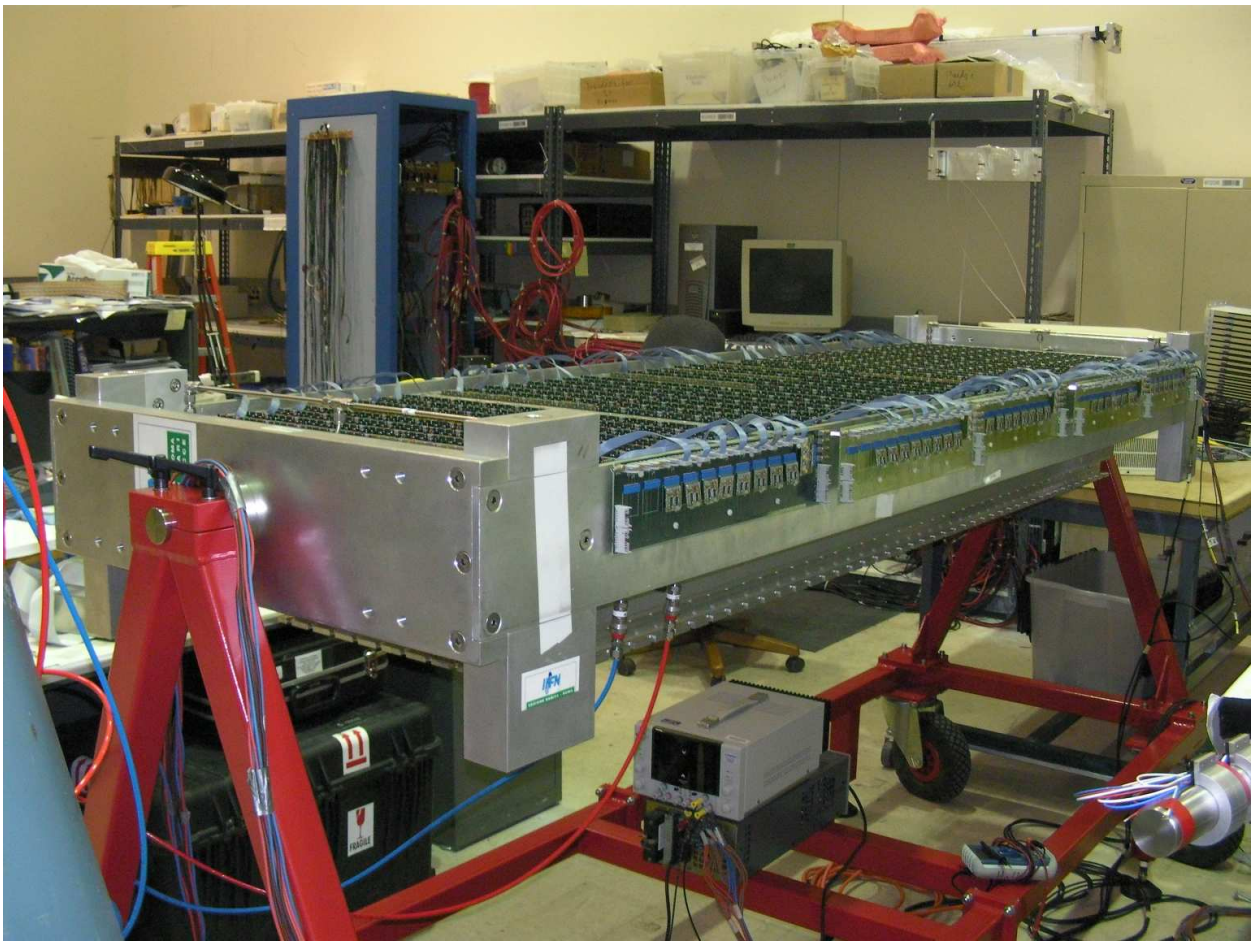

Figure 14: The RICH detector in the EEL building during the chamber cosmics test, in August 2008, before installation.

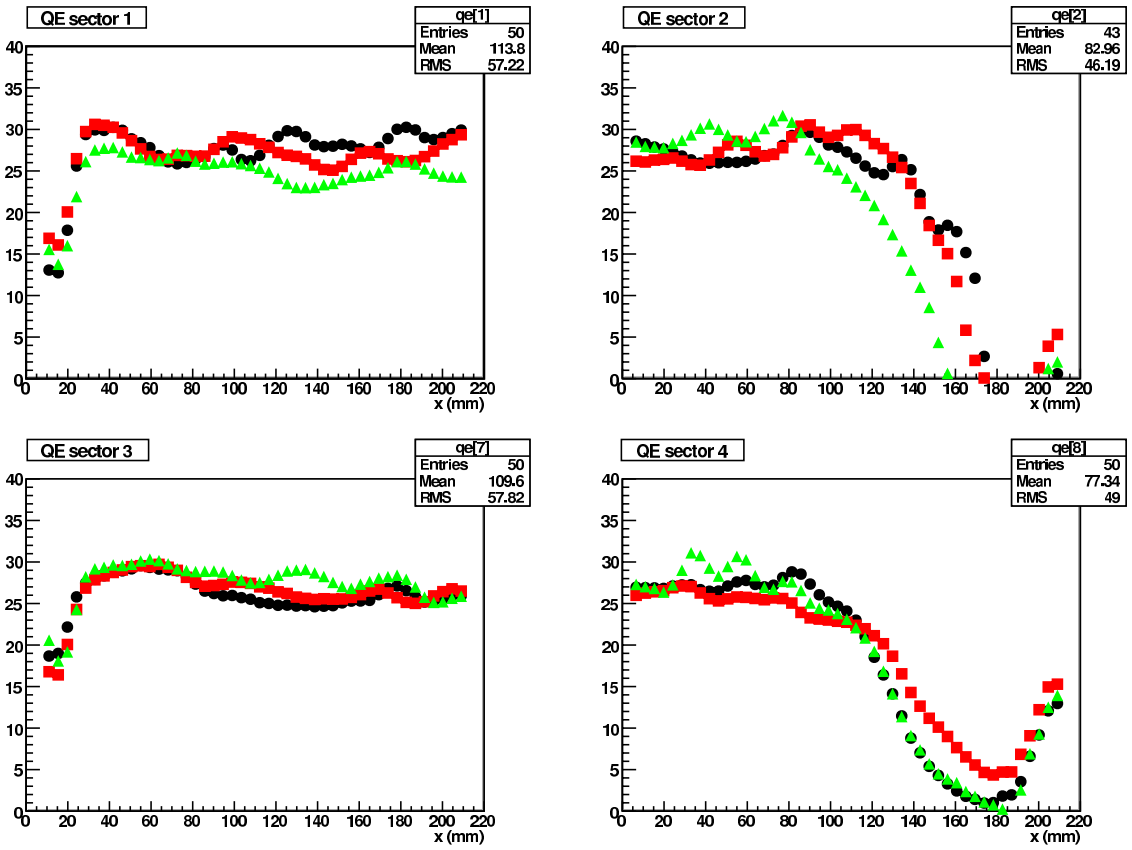

Figure 15: Post CsI evaporation, quantum efficiency measurement on pad panel 4 (out of 5) at 160 nm; the 4 plots represent 4 different complementary regions on the pad panel, approximately corresponding to the 4 plot areas. Each curve corresponds to a horizontal scan in the region.

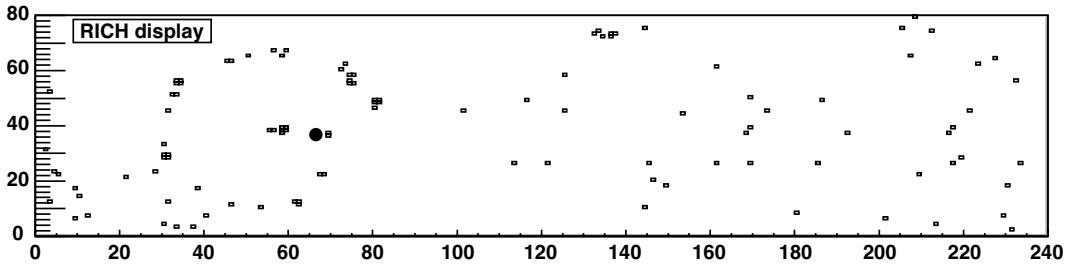

Figure 16: Very first ring, produced by an electron at plateau, observed on the upgraded RICH during the commissioning of the detector. Mapping and calibration were not optimized.

2.4 Data Analysis

Data Analysis
Contributed by J.-O. Hansen

2.4.1 Podd (ROOT/C++ Analyzer)

Version 1.5 of our C++ analysis software, Podd, was released, as planned, in the spring of 2008. This release includes a number of improvements needed for the new BigBite tracking software (see below) and by current experiments:

- The database system's capabilities were significantly expanded. Now supported are integer and string data, arrays, matrices, continuation lines, and in-line comments. Entries may be up to 16k characters long, up from 256. Error messages are more descriptive. Database keys are now case-sensitive for consistency with ROOT (and C/C++). Multiple variables can now be parsed and loaded with a single database request, resulting in a major simplification of `ReadDatabase` functions.
- Detector maps may contain more information. In particular, the support for "reference channels" of pipeline TDCs was expanded. The entire detector map, encoded as a string, can now be read with a single function call. Error checking has been much improved.
- The helicity decoder classes have been restructured for greater clarity. Different helicity decoding schemes are now implemented as independent classes rather than one large catch-all "helicity class".
- Support for current Linux and ROOT versions (including ROOT 5.20 and Fedora 9).
- Intelligent handling of split CODA run files. Support for input files larger than 2 GB in size.
- Small bug fixes (formulas, output, database, scalers). Details can be found in the `ChangeLog` file included in the distribution.

All experiments that ran during 2008 used Podd 1.5, resulting in very well tested code. The current version is 1.5.7. Many of the bug fixes and the changes for newer platforms were also backported to the previous production release, which is now at version 1.4.12.

As was already mentioned last year, we consider Podd to be "mature" at this point in time. As a result, the active development by Hall A staff of new features for the core analyzer has essentially ended. Of course, troubleshooting and porting to new platforms will continue, as needed. However, major improvements and new features are expected to be contributed by the user community.

2.4.2 BigBite Tracking Software

In the fall of 2007, we began a project to re-write the track reconstruction software for the BigBite spectrometer. This was motivated by the relatively slow performance and poor scalability of the existing tracking code that had been written for the G_E^n experiment, E02-013.

The new reconstruction software uses a recursive template matching algorithm, also known as "Tree Search" [1]. This algorithm has been used successfully in HERMES [2] with similar chambers and under similar conditions as BigBite in Hall A. The core Tree Search algorithm was already discussed at length in last year's Hall A annual report and was already working at that time. In early 2008, the remaining parts of the reconstruction were implemented. The tracking code was finished in April 2008, in time for experiment E04-007, which was the first to employ the BigBite wire chambers since E02-013.

During the final phase of the development, it became evident that the basic Tree Search pattern recognition represents only one (although a very important one) of the algorithms necessary for track reconstruction. The output of Tree Search is not only a single bit pattern per track, but *almost always* a set of similar (usually neighboring) patterns which all describe the same track. There are several reasons for this: (1) the left-right ambiguity of the position measurement in the drift chambers; (2) the finite resolution of the position measurement, which may require two adjacent bins to be set if a measured position is near a bin boundary; (3) noise hits or crosstalk between adjacent wires, which may activate nearby bins; and (4) the need to allow for missing hits in one or more planes due to unavoidable chamber inefficiencies.

As a result, a single track, even in the absence of noise and crosstalk, may activate between 0–4 bins in each wire plane. Depending on the spacings between the planes and the number of planes allowed to have missing hits, there are typically $\mathcal{O}(10)$ combinations of these active bins that will match patterns consistent with a straight line in the Tree Search phase.

To avoid the generation of "clone tracks" (duplicates with very similar parameters), it is necessary to detect groups (clusters) of patterns that describe the same track. This is known as a clustering problem in computer science. There are no exact but only statistical solutions, especially since the number of clusters to be found is a priori unknown.

In early 2008, we implemented a heuristic solution to the pattern clustering and track cloning problem. In this approach, clusters are formed from patterns which share common hits. The hit positions within each cluster are fit, and the best fit is kept, resulting in a single 2D track projection for each wire direction (u, v, x). Track projections of the three different directions are then matched in 3D: for each pair of u and v coordinates, there must be a matching x coordinate nearby, otherwise the combination is discarded. Next, the hits from each matching 3-tuple of 2D track projections are fit in 3D space, using the linear minimization algorithm (Cholesky decomposition) implemented in ROOT's `TLinearFitter` class. Finally, the resulting 3D tracks are ordered by χ^2, and sharing of any hits between different tracks is disallowed, *i.e.* if several tracks share any hit(s), only the one with the best χ^2 survives.

The method just described is the one that has been used for the analysis of the production experiments so far, It appears to give reasonable results and good tracking efficiency ($> 80\%$). With the E02-013 data from 2006, when 15 wire planes were used in BigBite, the reconstruction speed is very fast, close to 1 kHz on current hardware, and pattern clustering appears straightforward. On the other hand, in experiment E04-007, only 12 wire planes (two groups of six, *i.e.* 2×2 planes for each wire direction) were available. This low number of planes is not well suited for TreeSearch reconstruction; a very large number of clone (and ghost) patterns is produced because there is no center wire plane to eliminate ambiguities. Consequently, the burden of the actual track reconstruction is shifted to the clustering and fitting stages. Although the code is still successful in finding good tracks with high efficiency, the reconstruction speed suffers significantly (by up to a factor of 10) because these secondary algorithms scale unfavorably with increasing amount of input data. While TreeSearch scales approximately linearly (or better) with the number of hits per event, N, the heuristic clustering method runs roughly like $N_p^2 \log N_p$, where N_p is the number of patterns, which is roughly proportional to N if TreeSearch does not discriminate patterns well. All following algorithms (2D fitting, 3D combination, 3D fitting, 3D de-cloning) also grow at least like N_k^2, where the N_k again are proportional to N, but with small proportionality constants of order 10^{-3} to 10^{-1}. With $N \approx 200$ to 300 in E04-007, the performance of the clustering algorithm becomes the bottleneck of the entire reconstruction.

To address the slow performance with the 12-plane E04-007 data, we developed an alternative clustering algorithm in the summer of 2008 as part of a SULI summer student project. The resulting algorithm can be shown to scale (almost) linearly with input complexity, N, is noticeably faster, and

otherwise yields results that are essentially identical to those obtained with the original algorithm [3]. Some further testing is required. We plan to include this algorithm in the official Tree Search library in the next few months.

To illustrate the reconstruction performance obtained so far, we show several representative results. Figure 17 plots the horizontal position y vs. horizontal track angle ϕ at the front plane of BigBite for E04-007 data taken with a point target. Note that BigBite is non-dispersive in the horizontal plane, resulting in a clean linear correlation for tracks from the target, smeared only by the reconstruction resolution. The track multiplicity per event is histogrammed in Figure 18. Shown in Figure 19 are typical per-plane residuals for the same data set. Finally, Figure 20 displays the distribution of χ^2 of good tracks compared to a fit to the theoretical χ^2 distribution. One observes an excess of larger χ^2 values, due to still imperfect calibrations and missing corrections.

Reconstruction of the tracks to the target coordinates has been implemented, in preliminary form, by Jin Huang, also in spring/summer of 2008 [4]. Extensive calibration work was done subsequently by Sergey Abrahamyan [5]. Still missing in the core reconstruction code are a number of corrections known to be important, in particular the $1/\cos\theta$ drift-time correction and corrections for trigger timing and magnet fringe fields.

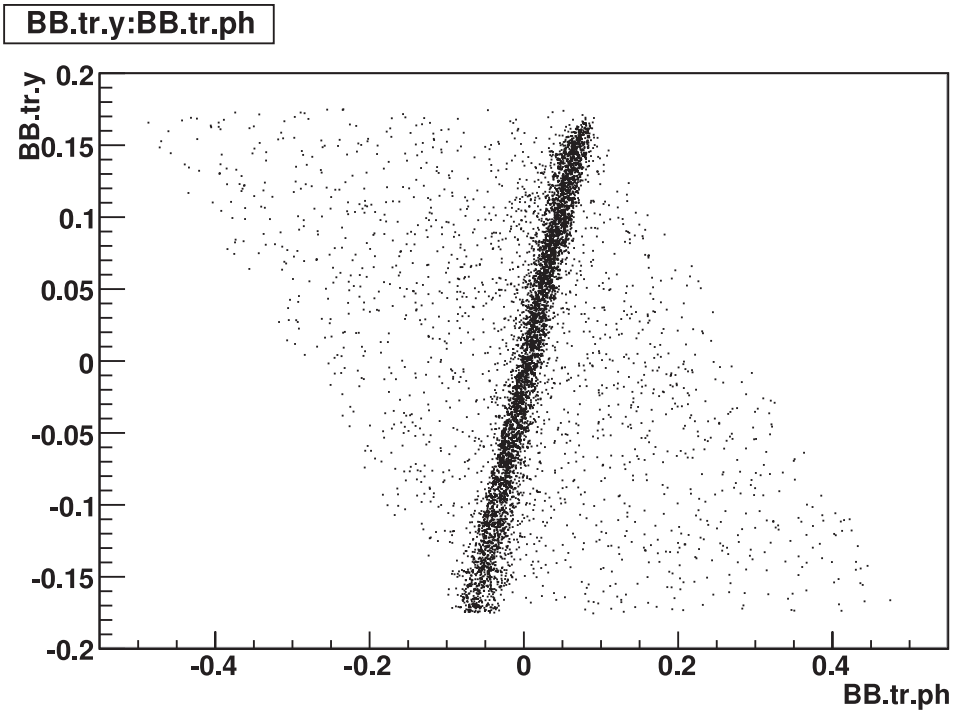

Figure 17: Horizontal position y vs. horizontal angle ϕ for good tracks at the front plane of BigBite, reconstructed with the Tree Search tracking software.

2.4.3 Analysis Workshops

Beginning in January 2007, we have resumed regular Hall A Data Analysis Workshops. These are one-day meetings that are held semi-annually in conjunction with the main Hall A collaboration meetings. They consist of a number of general-interest talks about recent progress with Hall A data analysis, followed by reports from currently active experiments that focus on technical data analysis issues. Talks are published on the Web and can be found at `http://hallaweb.jlab.org/data_reduc/`.

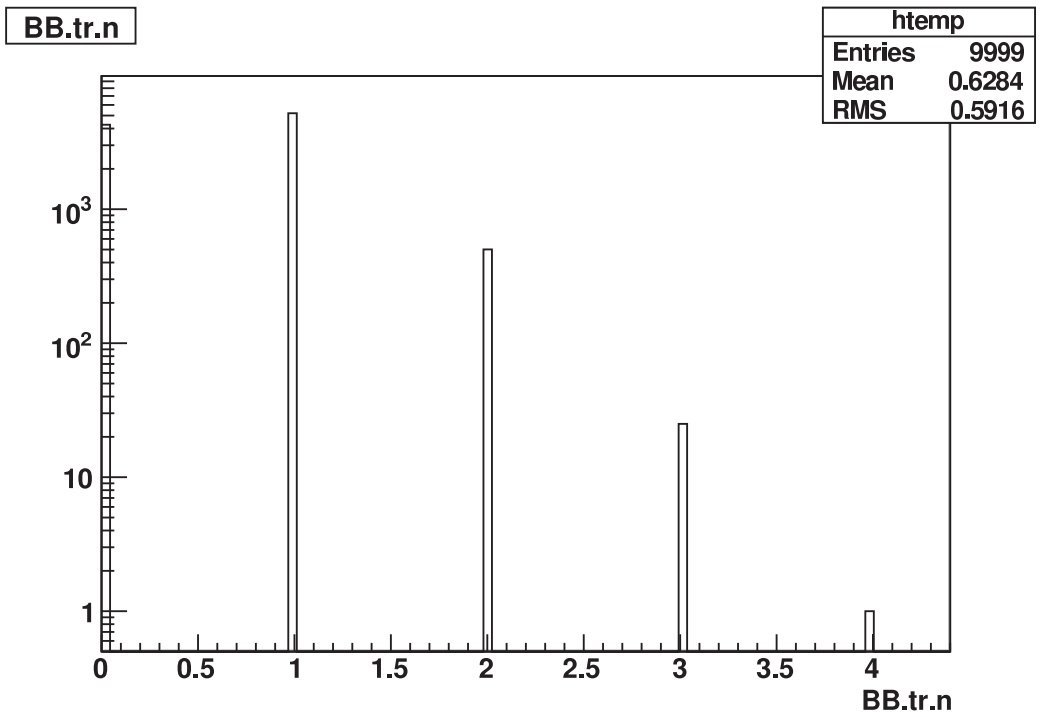

Figure 18: BigBite track multiplicity per event for noisy E04-007 data, obtained with the Tree Search tracking software

Participation from anyone involved in Hall A data analysis is encouraged. The most recent workshop was successfully broadcast via EVO internet video conferencing, allowing even collaborators who are unable to travel to participate passively or actively in the meeting.

References

[1] M. Dell'orso and L. Ristori, Nucl. Instr. Meth. in Phys. Res. A **287**, 436 (1990).

[2] K. Ackerstaff *et al.*, Nucl. Instr. Meth. in Phys. Res. A **417**, 230 (1998).

[3] A. Lundin, "Improving De-Cloning Algorithms for Jefferson Lab's Hall A BigBite Spectrometer", internship paper, Jefferson Lab, summer 2008 (unpublished)

[4] J. Huang, "An Online Optics Module for BigBite Spectrometer", talk at June 2008 Hall A data analysis workshop, `http://hallaweb.jlab.org/data_reduc/AnaWork2008a/bb-optics.pdf`

[5] S. Abrahamyan, "BigBite Drift Chamber Time and Position Optimization", talk at December 2008 Hall A data analysis workshop,
`http://hallaweb.jlab.org/data_reduc/AnaWork2008b/bb_optimization_sergey.pdf`

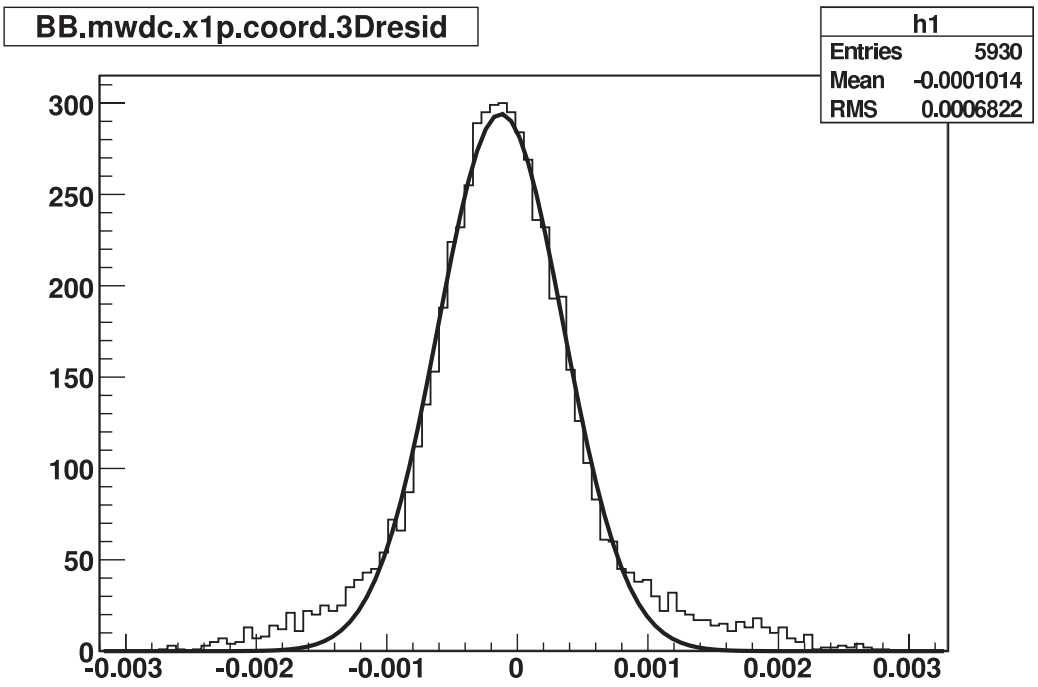

Figure 19: Position residuals in BigBite wire plane x'_1, obtained with the Tree Search track reconstruction software.

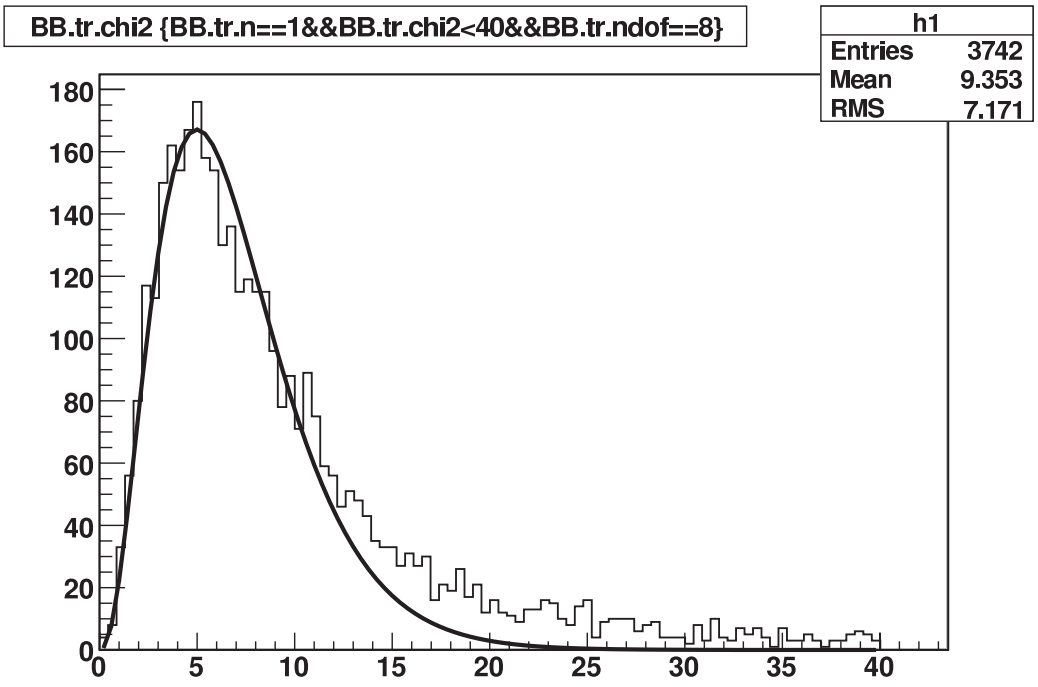

Figure 20: Distribution of the χ^2 of fits for good reconstructed tracks in BigBite, obtained with noisy E04-007 data and the Tree Search track reconstruction software.

2.5 BigBite Spectrometer

New Equipment for the BigBite Spectrometer

D. W. Higinbotham on behalf of the BigFamily of Experiments

2.5.1 Introduction

With the first two BigBite spectrometer experiments complete, one that probed short-range correlations [1] and the other that determined the electric form factor of the neutron at high Q^2 [2], 2008 brought with it the start of the BigFamily of BigBite experiments [3]. Of this large series of experiments, the threshold π^0 experiment [4] and proton form factor experiment [5] were completed and at the end of the year the Transversity experiments were underway [6, 7, 8]. Early next year, we will switch over to a d2n measurement [9] . As of the written of this document, it is not clear if the funding will be in place to allow us to run the remaining three quasi-elastic experiments [10, 11, 12], but if the money arrives, the experiment will be ready to run. The new wirechamber and referbished shower detectors that were reported on in the 2007 annual report have both functioned as expected.

2.5.2 BigBite Installation

In 2008 the BigBite equipment was moved from the Test Lab building into the Hall. Shown in Fig. 21 is the BigBite detector package as it looked during the π^0 experiment. After the π^0 experiment was complete, we switched from the hadron detector package shown in the photo to the much heavier electron detector package as soon in Fig. 22. The hadron package is comprised solely of two chambers and two layers of scintillator, while the electron package is comprised of three wire chambers, a lead glass preshower detector, timing scintillators, and finally a shower detector.

2.5.3 BigBite Sieve

In order to improve the optics of the BigBite spectrometer, a 1.5" thick (238 lb.) Pb sieve was designed primarily by Xin Qian and Xiaodong Jiang for the Transversity experiment. The π^0 used a simpliar device though their sieve was made out of Tungsten and located on the scattering chamber instead of on the BigBite field clamp. Both devices moves in and out of the BigBite acceptance with a pulley system. Fig. 23 shows a photo of the sieve as well a very preliminary result of sieve data. Though no changes had yet been made to the database, the sieve pattern as found during the start-up of the Transversity experiment was already quite clear with the holes and slits matching up nicely. The Transversity Pb sieve, which was made completely by lead shielding manufacture Kolgashield, is currently showned on the vendors web site under recent projects: http://www.kolgashield.com/Recent.html as one of their highlighted projects.

2.5.4 BigBite Cherenkov

In order to run BigBite in a single arm mode of the d2n experiment [9], a gas Cherenkov detector was designed by Brad Sawatzky of Temple University. An exploded view diagram of the detector is shown in Fig. 24. The detector was completed in the Test Lab and installed between during the proton form factor experiment [5]. During that experiment, no real signal was found in the TDC spectrums from the phototubes. This was tracked down to insufficient magnetic shielding for operating near the BigBite dipole when the dipole was operated at its maximum field of 1.2T.

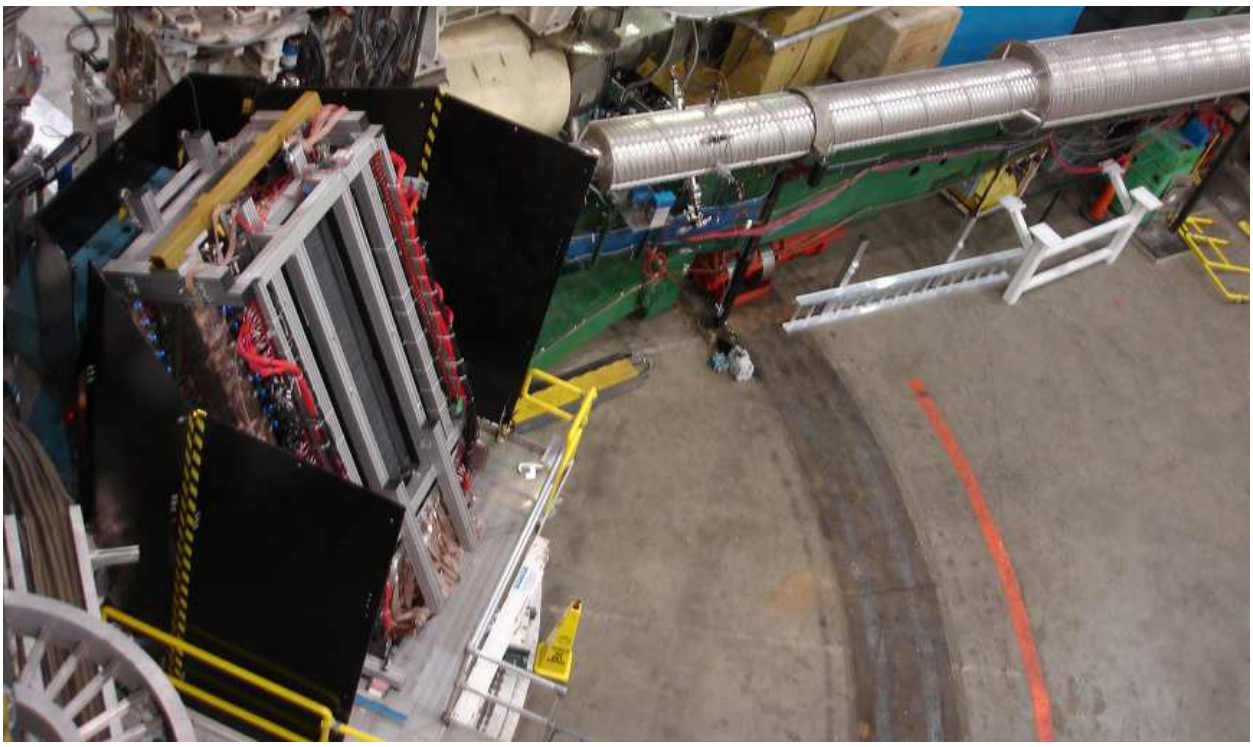

Figure 21: Shown on the left side of the photo is the BigBite spectrometer with its hadron detector package and black, steel shielding walls. The silver exit beam line and part of the left HRS are visible in the background.

At this field strength, the fringe fields are relatively strong and the 5" photomultier tubes are particularly sensitive to magnetic fields.

To fix this problem, extra magnetic shielding was designed and installed. The new shielding did require that the phototubes be pulled back from their idea position. New measurements that have being done during the Transversity experiment [6, 7] and now show a nice Cherenkov signal, though the signal strength it is approximately a factor of two lower then expected. In order to make sure that all surfaces are as reflective as the detector's design calls for, reflectivity tests are being done on samples of all of the mirror surfaces. Tests are also planned with CO_2 gas instead of the C_4F_8O that is currently being used. With the change in gas, a further reduction of the signal by a factor of two is expected.

2.5.5 Acknowledgments

Many many people helped with the installation of the BigBite equipment in the Hall A and they all contributed to the sucess of the running of the BigFamily of experiments. In particular, the students Xin Jiang (Duke) and Kalyan Allada (Kentucky) became masters of the detectors and electronics. Thanks to the Guy Ron and Tel Aviv group for helping with cabling. Mitra (UVa), with her steady hands, was master full at fixing broken wires in the BigBite chambrs. Thank you to Miha Mihovilovic (Slovenia) for his graphics package for BigBite and Jin Huang (MIT) for his work on BigBite optics. Postdocs Brad Sawatzky (Temple) and Bryan Moffit (MIT) were indispensable at making sure everything got done. And thanks to Xiaodong Jiang (LANL) whose

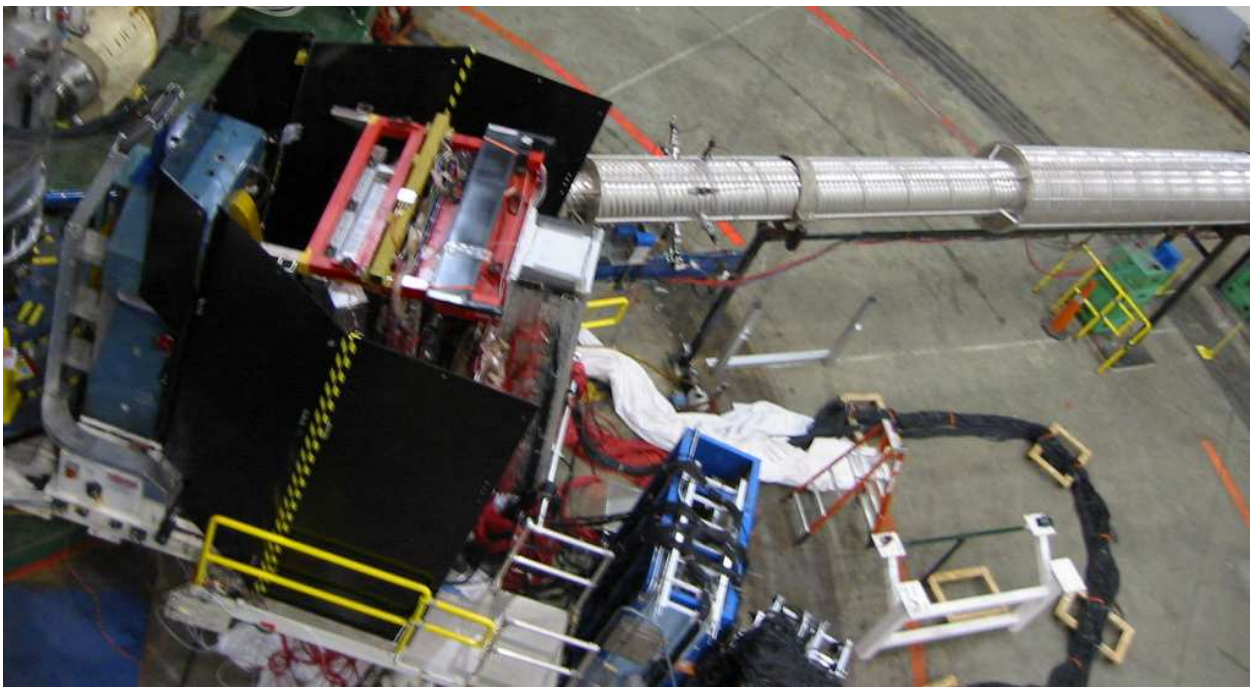

Figure 22: Shown on the left side of the photo is the BigBite spectrometer with its electron detector package during the proton form factor measurement [5]. The cables from the front end electrons are visible on the floor as well as the silver exit beam line.

constant pushing for improvements and ability to track down equipment truly helped make the entire program a success.

References

[1] S. Gilad, D. Higinbotham, E. Piasetzky, J. Watson and S. Wood, spokespersons, JLab Experiment E01-015, *Studying the internal small-distance structure of Nuclei via the triple coincidence (e,e'p+N) measurement.*

[2] G. Cates, N. Liyanage and B. Wojtsekhowski, spokespersons, JLab Experiment E02-013,

[3] http:hallaweb.jlab.org/experiment/BigFamily *Measurement of the neutron electric form factor* G_n^E *at high* Q^2.

[4] J. Annand, D.W. Higinbotham, R. Lindgren, B. Moffit, B.E. Norum and V. Nelyubin, spokespersons, JLab Experiment E04-007, *Precision measurement of electroproduction of* π^0 *near threshold: a test of chiral QCD dynamics.*

[5] J. Arrington, D. Day, R. Gilman, D.W. Higinbotham, G. Ron, A. Sarty, spokespersons, JLab Experiment E08-007, *The proton form factor ratio at low* Q^2.

[6] J.P. Chen, X. Jiang and J.C. Peng, spokespersons, JLab Experiment E06-010, *Measurement of single target-spin asymmetry in semi-inclusive 3He(e,e'pi-) reaction on on a transversely polarized* ^{3}*He target.*

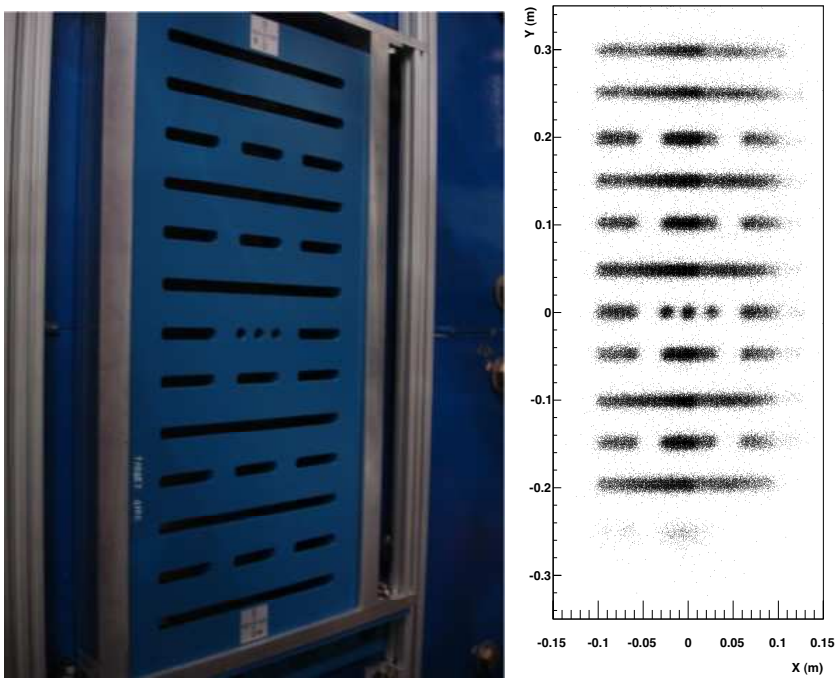

Figure 23: On the left is a photo of the BigBite sieve installed in front of the BigBite dipole. On the right is some preliminary data where matching slits and holes of the sieve can be seen.

[7] E. Cisbani, H. Gao and X. Jiang, spokespersons, JLab Experiment E06-011, *Measurement of single target-spin asymmetry in semi-inclusive 3He(e,e'pi+) reaction on on a transversely polarized ^{3}He target.*

[8] T. Averett, R. Gilman, T. Holmstrom and X. Jiang, spokespersons, JLab Experiment E06-012, *A Parasitic Measurement during E03-004 for Target Single-Spin Asymmetry in Inclusive DIS (e,e') Reaction on a Vertically Polarized 3He Target.*

[9] S. Choi, X. Jiang, Z.E. Meziani, and B. Sawatzky, spokespersons, JLab Experiment E06-014, *Precision Measurements of the Neutron d2: Towards the Electric and Magnetic Color Polarizabilities.*

[10] T. Avertt, J.P. Chen, and X. Jiang, spokespersons, JLab Experiment E05-015, *Measurement of the Target Single-Spin Asymmetry in Quasi-Elastic 3He$\hat{}$(e,e').*

[11] S. Gilad, D.W. Higinbotham, W. Korsh, B.E. Norum and S. Širca spokespersons, JLab Experiment E05-102, *Measurement of A_x and A_z asymmetries in the quasi-elastic polarized ^{3}He($\vec{e}$,e'd) reaction.*

[12] T. Avertt, D.W. Higinbotham and V. Sulkosky, spokespersons, JLab Experiment E08-005, *Measurements of the Target Single-Spin Asymmetry in the Quasi-Elastic polarized 3He(e,e'n) Reaction.*

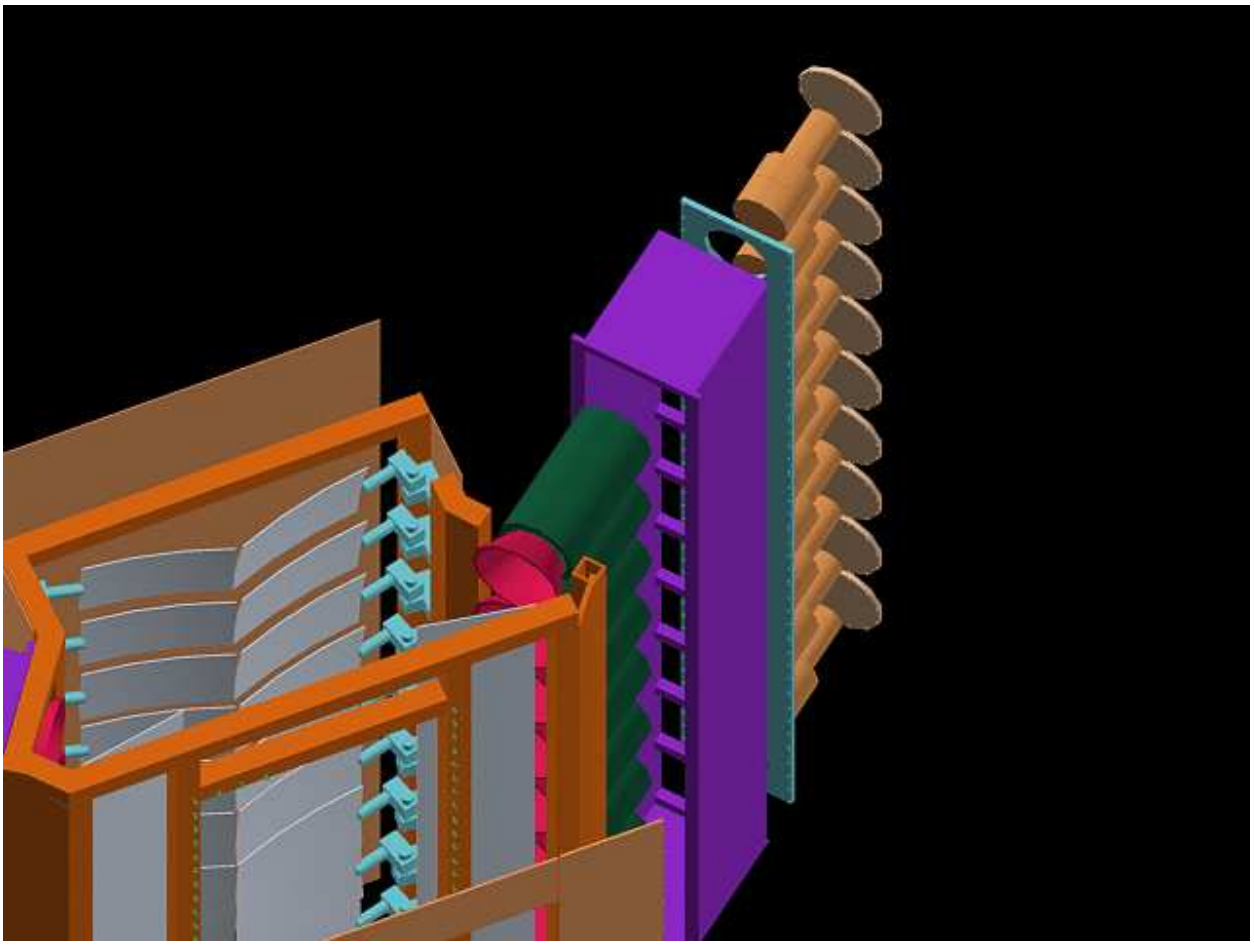

Figure 24: Shown is an exploded view diagram of the BigBite Cherenkov detector showing the mirrors , PMTs, and Winston cones. The primary spherical mirrors are 31 cm wide by 21 cm tall with a radius of 116 cm and a focal length of 58 cm. The secondary mirrors are 24 cm wide by 20 cm tall. The light is finally detected by 5" photomultiplier tubes.

3 General Hall Developments

3.1 12 GeV DAQ Upgrade

Hall A 12 GeV DAQ Upgrade

Robert Michaels, Alexandre Camsonne, Jack Segal, Dave Abbott

3.1.1 Introduction

The 12 GeV upgrade plan includes possible funding for an upgrade of the Hall A HRS DAQ. There are two themes to this upgrade: 1) Replace obsolete components, and 2) Achieve a much higher DAQ rate using full pipelining, possibly 200 kHz with practically zero deadtime. Such a rate increase could open the door to a number of new experiments. The higher rate is achievable for two primary reasons: 1) The frontend digitizers have a pipeline (large buffer) and minimal conversion processing time (≤ 5 μs); and 2) The frontends will support blocking of events and a new trigger distribution system (TS) will block trigger data. This anticipated higher speed still needs to be demonstrated in a test stand.

This document describes the result of our project engineering (PED) effort. Section II describes the existing system and section III outlines the upgrade design, while section IV provides an estimate of the costs and the timescale.

3.1.2 Description of Existing Hall A DAQ

The data-acquisition (DAQ) systems in Hall A use CODA (CEBAF On-line Data Acquisition System) developed by the JLab Data Acquisition group.

The hardware elements include commercial front-end Fastbus and VME digitization devices (ADCs, TDCs, scalers), the Struck Fastbus Interface (a VME interface to Fastbus), single-board VME computers, Ethernet networks (100 Mbit at the frontend), Unix or Linux workstations, and a mass storage tape silo (MSS) for long-term data storage. Custom hardware elements made at JLab include the trigger supervisor which synchronizes the read-out of the front-end crates and handles the dead-time logic of the system, as well as interface cards for the Fastbus and VME crates which facilitate communication between the trigger supervisor and the front-end crates. CODA also includes a number of custom software components, like the event builder, etc. Because of the modular nature of CODA and its emphasis on commercially available components, data-acquisition systems can be built and reconfigured rapidly.

The present DAQ is shown schematically in fig. 25. On each HRS we have two Fastbus crates which are nearly full. They contain TDCs (obsolete LeCroy models 1877 and 1875) and ADCs (1881M). In addition, each HRS DAQ has a VME crate with scalers primarily and some miscellaneous I/O. Various third-arm spectrometers are deployed for different experiments. For example, the BigBite DAQ has three Fastbus crates with mostly 1877 and a few 1881M, and two VME crates with CAEN TDCs and a third VME crate with F1 TDCs. Other major third-arm systems have been the RCS calorimeter, the DVCS detector system, and the BigHand detector.

The typical performance for a 2 kHz trigger rate results in a $\sim 20\%$ dead time in coincidence mode. If compromises are made, as appropriate for some experiments, e.g. drop the slow TDC 1875 modules, the speed can be approximately doubled. We believe we can improve the rate capability to ~ 200 kHz with the future design (next section).

The trigger system is built from commercial CAMAC and NIM discriminators, delay units, logic units, and memory lookup units (MLU). The primary trigger is formed from a coincidence between scintillator detector planes. Sometimes other detectors, e.g. gas Čerenkov detectors, are

involved in forming various types of triggers. The trigger modules are remotely programmed by CAMAC commands sent from a software control package. The electronic deadtime is measured with a custom-made pulsing system that adds signals to the PMT pulses.

One major concern with the current system is that both the DAQ and the trigger contain many hardware elements which are obsolete and would be difficult if not impossible to repair or replace in case of failures. In the next section we identify replacement components.

3.1.3 12 GeV Upgrade Plan

We need to replace all our Fastbus and CAMAC modules. For the Fastbus, the present plan is to use the JLab-built VME-based F1-TDCs and FADCs, or suitable commercial units. These also have the important upgrade potential of allowing pipelining and higher rates. Some commercially available VME units might become competitive, in particular TDCs and FADCs from CAEN, and the FADCs from SISGmbH. The F1-TDC can be run in either a low-resolution mode (120 ps) or high-resolution mode (60 ps); the former is a replacement for the model 1877 Fastbus TDC, and the latter replaces the 1875. The JLab-FADC will be a replacement for the 1881M ADC. This FADC will be a 250 MHz 12 bit unit. We might need preamps and shaping to get the resolution. In the next few years, we will be using the JLab-built units as well as commercial VME units in various setups, e.g. BigBite and Compton. The experience will help us evaluate what is best for the future.

To take full advantage of faster frond-end readout we will also need VME64X crates, Gigabit ethernet, and a new Trigger and Clock Distribution System that is being designed by the DAQ group. The frontend VME cpus will need to be fast (supporting higher VME transfer modes, 2eVME and 2eSST), multicore, and have Gigabit ethernet, and will have the option of using embedded Linux.

We also need to replace our CAMAC trigger modules with NIM and VME based electronics. It is doubtful that CAMAC has much of a future. However, we will keep one CAMAC crate in each HRS with "legacy" modules. This will house our EDTM system and we will make available CAMAC delay and discriminators that may still exist. The strategy is to eliminate our reliance on CAMAC, but we can still use the existing modules where convenient.

Our quantity of CAMAC spare modules is dangerously low and the modules are either difficult or impossible to fix since they are based on obsolete components. Note, the danger is not quite as bad with Fastbus because we've obtained a large supply of excessed material from other labs, so as the old modules go bad they can be swapped out. This strategy should help us survive the next few years with Fastbus.

3.1.4 Estimates of Cost and Time

We have identified replacement items for all the trigger modules if we had to buy them "tomorrow", see table 3. A notable exception is the programmable delay (LeCroy model 4518), for which there is no currently available commercial replacement. Therefore we have requested the JLab electronics group to build a programmable delay module in VME format with the same features (plus small improvements) over the existing ones. A specification has been written and Chris Cuevas's group has accepted responsibility for building this delay unit.

Figure 27 is a possible schematic of our future trigger and fig. 26 shows the future DAQ layout. Table 3 is a snapshot of what's available now on the market, and it is somewhat uncertain how this will change in the next few years. Also in table 3 is an estimate of the costs for upgrading the HRS DAQ and trigger. The rough estimate of the total cost is 833 k$.

Table 3: **HRS DAQ and Trigger 12 GeV Upgrade**

Item	Replacement	Num. Units	Cost Each (K$)
DAQ			
TDC 1877 (0.5 nsec)	F1 TDC or CAEN 1190	80	4
TDC 1875 (0.05 nsec)	F1 TDC or CAEN 1190 or 1290A	8	4
ADC 1881M	JLab FADC, STR3320, or CAEN1720	50	5
Crates	Wiener or CAEN 64x	6 (have 2)	8
VME cpus	Motorola	6	5
Trig. Supervisor	JLab electronics	1	5
Distribution Module	JLab electronics	1	5
Trig. Interface	JLab electronics	8	2
Fiber Cable			10
Gigabit Ethernet			25
Trigger			
LeCroy 4518 delay	JLab custom delay	10	2
LeCroy 4413 discr	Phillips 706 or CAEN 895	10	1.5
LeCroy 4516 logic	Phillips 758, 756, 757	22 (tot)	1.5
LeCroy 2373 MLU	CAEN V1495	6	4
TOTAL COST			833 k$

The schedule is somewhat flexible. Since the greatest danger we face is our obsolete CAMAC, we could upgrade the trigger first (38 k$ per HRS) starting with one HRS. To spread the cost over time, we could replace a few items at a time. We will need a test area of about $3 \times 3m^2$ ($\sim 10' \times 10'$) to test the trigger/DAQ. This will minimize downtime and check the less-certain items before making a major financial commitment. Table 4 is a schedule suggested for discussion.

3.1.5 Appendix – Experience from Hall B

Experience from the Hall B upgrade (Sergey Boyarinov) may be relevant. They have replaced their 1872 and 1875A TDCs with CAEN 1180 and 1290. This alone has led to an improvement in speed because the 1872/75A are the slowest of the fastbus modules. Hall B also plans to use the JLab-built FADC to replace the 1881M. Hall B has also made software improvements to their readout and to the event builder which improves the buffering. Where applicable, these improvements are being incorporated into CODA version 3 and will benefit Hall A when we upgrade our frontend hardware. CODA 3 will be available on the timescale of this upgrade.

Table 4: **Possible Timeline for DAQ/Trigger Upgrade**

Time (years)	Task	Cost (k$)
0	purchase trigger	75
0.5	trigger test stand	
0.7	deploy trigger	
1	purchase most F1TDC for 1 HRS	120
1	purchase some crates and cpus	43
1	purchase a couple FADCs	10
1	trigger distrib. system and fiber	36
1.5	F1TDC/FADC test stand	
1.7	deploy F1TDC for 1 HRS	
2	purchase remaining F1TDC	200
1	purchase remaining crates and cpus	30
3	purchase hi-res TDCs	32
3	partial purchase FADCs	68
3.5	test stand hi-res TDCs	
3.7	deploy hi-res TDCs, FADCs	
4 & 5	purchase remaining equipment	219

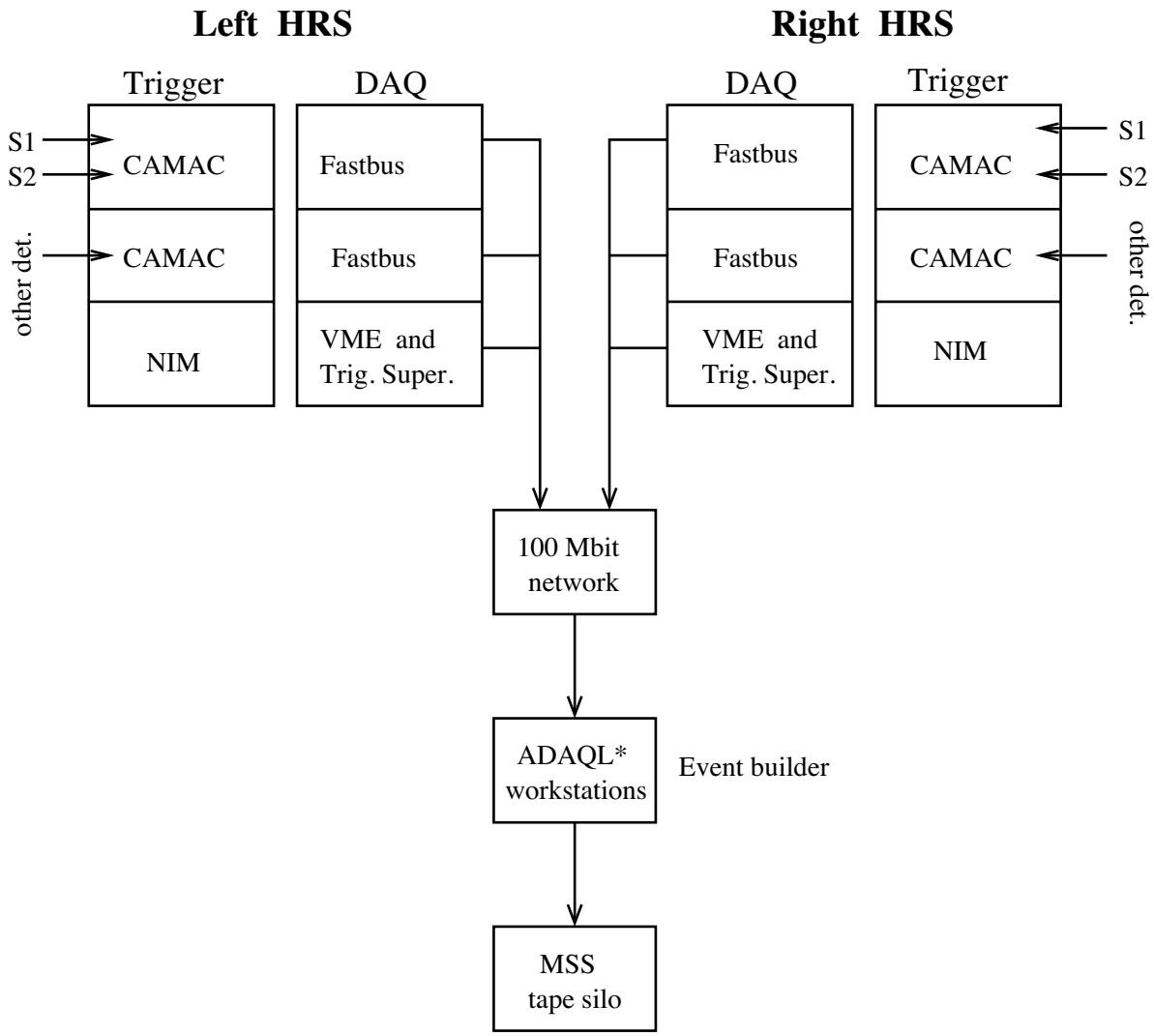

Figure 25: Overview Schematic of Present DAQ/Trigger.

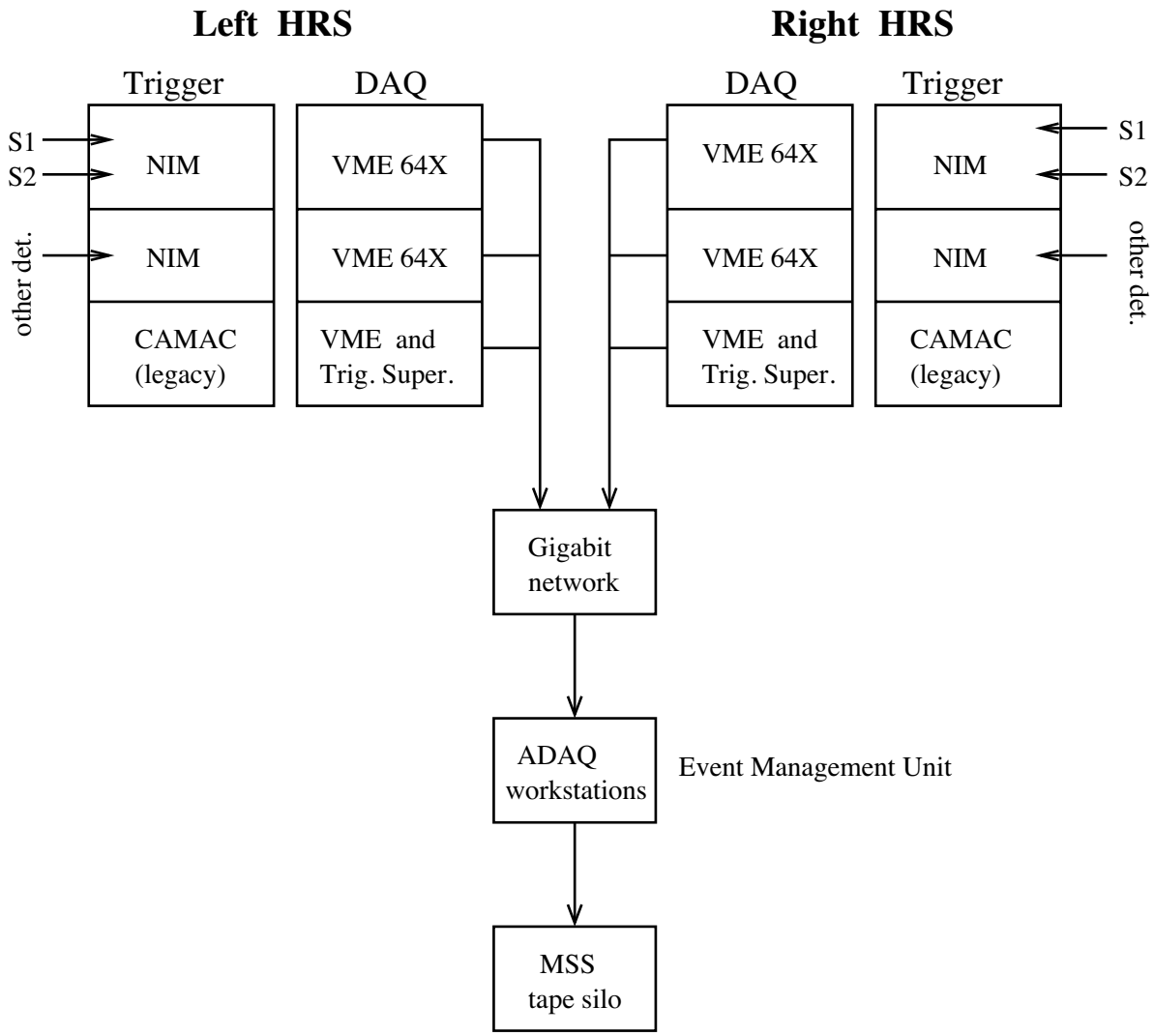

Figure 26: Schematic of 12 GeV DAQ/trigger.

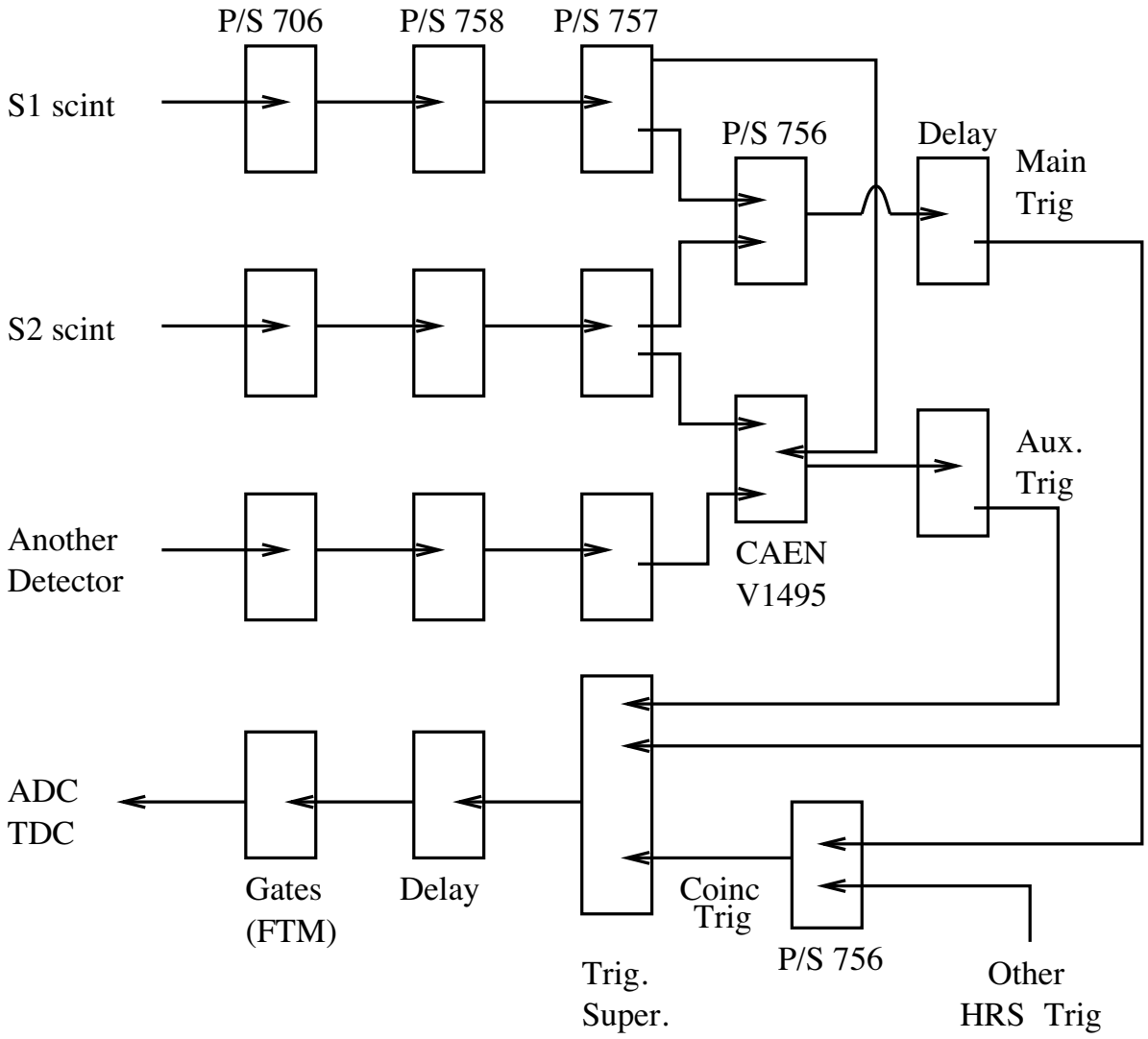

Figure 27: Schematic of 12 GeV Trigger using Phillips Modules (P/S) as an example.

3.2 Spin Manipulation

Spin Manipulation

contributed by D.W. Higinbotham.

Longitudinally polarized electron beams are produced in the CEBAF injector [1, 2] and required for a large fraction of the Jefferson Lab nuclear physics experiments. Spin transport from the injector to the experimental halls is complicated by the fact that the lab runs with different energies and even with different bend angles to the various halls. In the past, once a beam energy was established, the only parameter that could be changed to manipulate the spin was the Wien angle at the beginning of the machine. A simple example of CEBAF spin precession is shown in Fig. 28. In this example, the spin direction starts at the inject along the velocity direction ends in the three end stations with an angles of $2\phi + \beta, 2\phi$, and $2\phi - \beta$ respectively. This precession is determined by the formula:

$$\Delta\phi = E/440.65 \text{ MeV} \times \Delta\theta \tag{1}$$

where E is the energy of the beam and $\Delta\theta$ the bend angle in the ARC and then into the Hall. Since Jefferson Lab is a race track accelerator, E changes with each pass down a linac. This changing energy must be taken into account when determining the spin precession. The relation between the beam energy and the amount of precession has been used to help determine the beam energy at Jefferson Lab [3].

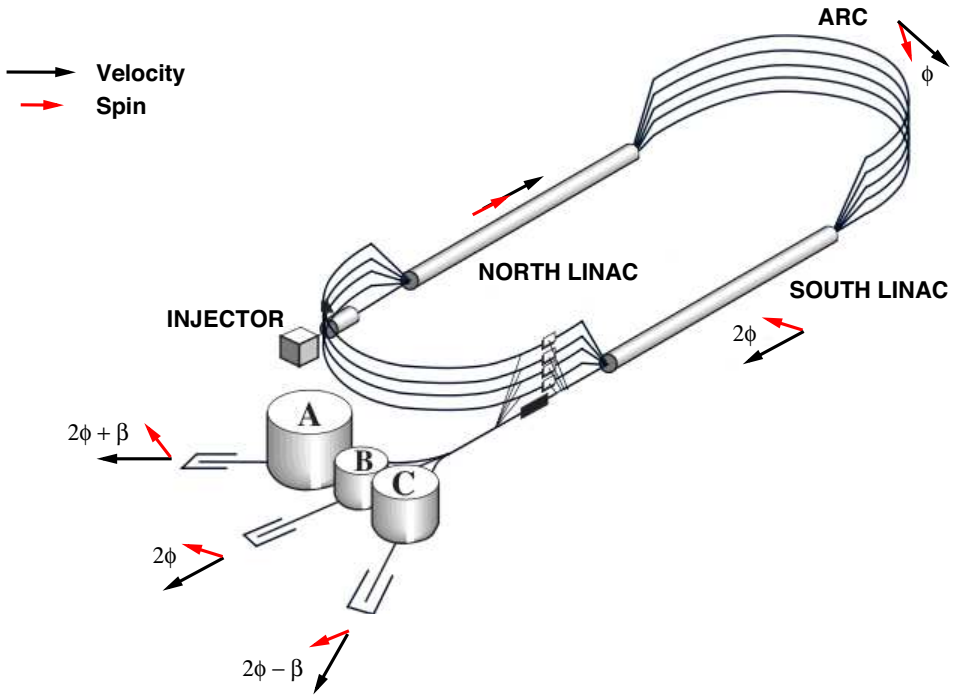

Figure 28: Shown is a simple example of spin precession in CEBAF. In this example first pass beam is being sent to all three halls. The velocity and spin directions start out parallel at the injector and continue parallel through the north linac. As the beam passes through the arc, spin precession causes the two vectors to start to point in different directions. By the time the beam has arrived at the three different end stations, the angle between the velocity and spin has taken on a different value, $2\phi + \beta, 2\phi$, and $2\phi - \beta$, for each hall.

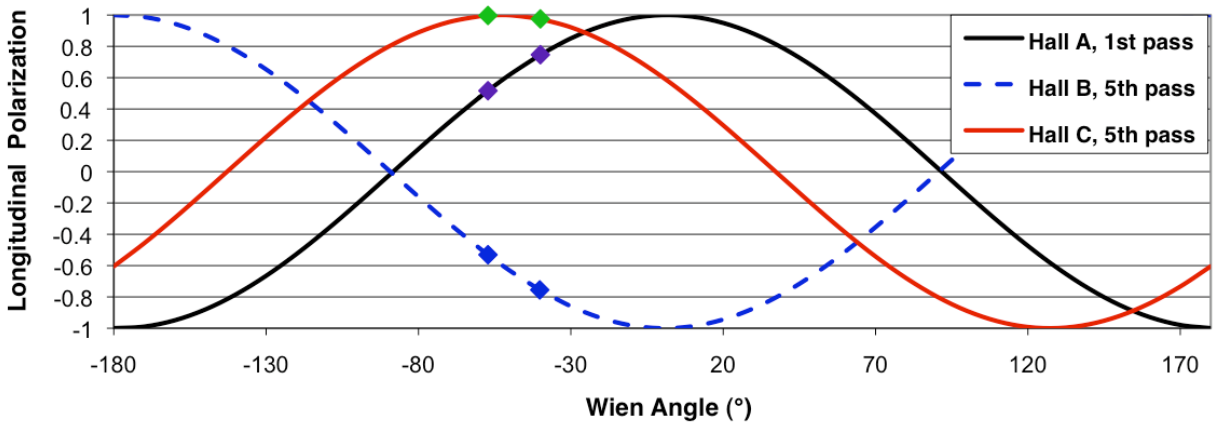

Figure 29: Shown is the degree of longitudinal polarization to the end stations for CEBAF setup with the injector set to 63.5 MeV and each of the linacs set to a gain of 565 MeV per pass. The points represent normalized Møller measurements done by the various Halls at different Wien settings. During this run period, in the Summer of 2008, Hall C was the only experiment running which required the highest polarization.

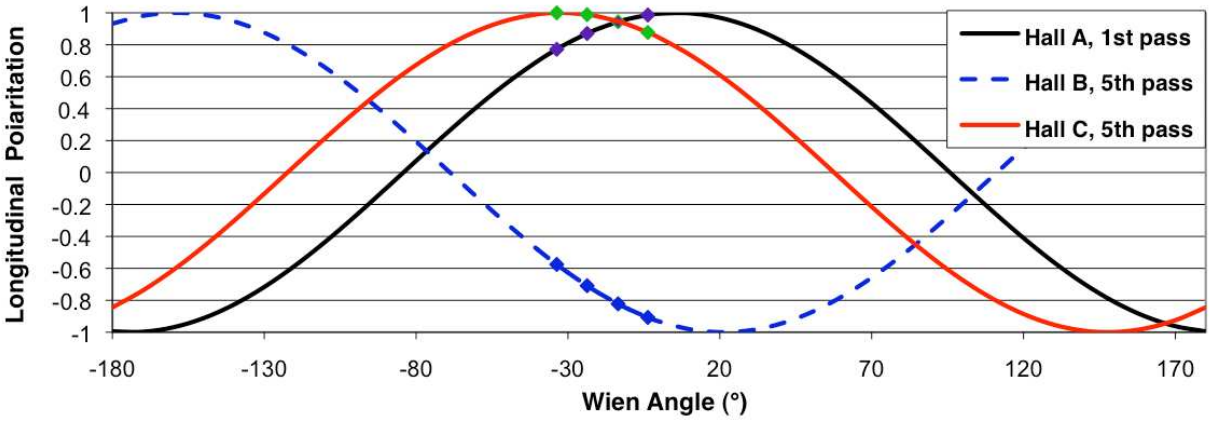

Figure 30: By reducing the north linac by 10 MeV and increasing the south linac by 10 MeV, we were able to deliver high polarization to both Halls A and C for the second half of the summer 2008 run period while not changing the beam energy Hall B was receiving. The points represent normalized Møller measurements done by the various Halls at different Wien settings.

In the summer of 2008, the machine was running with only one Hall requiring high polarization as shown in Fig. 29. Near the end of this same run period, both Hall A & C required high polarization; but Hall B required that the beam energy stay fixed. The Wien was the only classic parameter to change; but this would have only provided a P^2 of only 0.8 to Halls A & C and thus effectively caused a 10% hit in beam time. By having accelerator division imbalance the energy gain of the north and south linacs, the accelerator was able to provide a P^2 of 0.9 to both Halls A & C, as shown in Fig. 30 while still mantaining the same beam energy. This is summarized in Tab. 5.

Table 5: Shown are the conditions before and after imbalancing the CEBAF linacs. With Halls A and C both doing polarization transfer experiments, being able to keep both Halls at a P^2 of 0.9 prevented an effective 10% reduction in beam time.

	Injector	North Linac	South Linac	P^2
Balanced	63.5 MeV	565 MeV	565 MeV	0.8
Unbalanced	63.5 MeV	555 MeV	575 MeV	0.9

Now that this new method of changing the spin precession has been demonstrated, MCC is now working on investigating using it in the future. With two degrees of freedom (Wien and linac imbalance), the halls should be able to achieve higher longitudinal polarization then previously achievable.

References

[1] C. Hernandez-Garcia, M. L. Stutzman and P. G. O'Shea, Phys. Today **61N2**, 44 (2008).

[2] C. K. Sinclair *et al.*, Phys. Rev. ST Accel. Beams **10**, 023501 (2007).

[3] J. M. Grames *et al.*, Phys. Rev. ST Accel. Beams **7**, 042802 (2004).

3.3 A Room Temperature Septum Magnet for PREX

A Room Temperature Septum Magnet for PREX

John J. LeRose, Paul Brindza, and Bob Michaels

A new room temperature septum magnet has been designed and is being built for the PREX, E06-002, experiment. This new magnet, while being limited in its maximum central momentum, will make it possible to use the HRSs at central angles as small as 5° with uncompromised momentum and angular resolution and significantly higher luminosity than possible with the present superconducting septa. In fact, this magnet will not be a limiting factor in determining the maximum achievable luminosity. Acceptance, which will depend on the details of any particular experimental setup, will remain about the same as with the superconducting septa.

The general layout is illustrated in fig. 31. Notice that this magnet features a monolithic iron yoke with two separate coil and pole packages. Different central angles are attained by simultaneously moving the target position and rotating both HRS's around the pivot while keeping the septum fixed. With this magnet one is limited to using the same central angles on the left and right sides. However, any combination of polarities is possible.

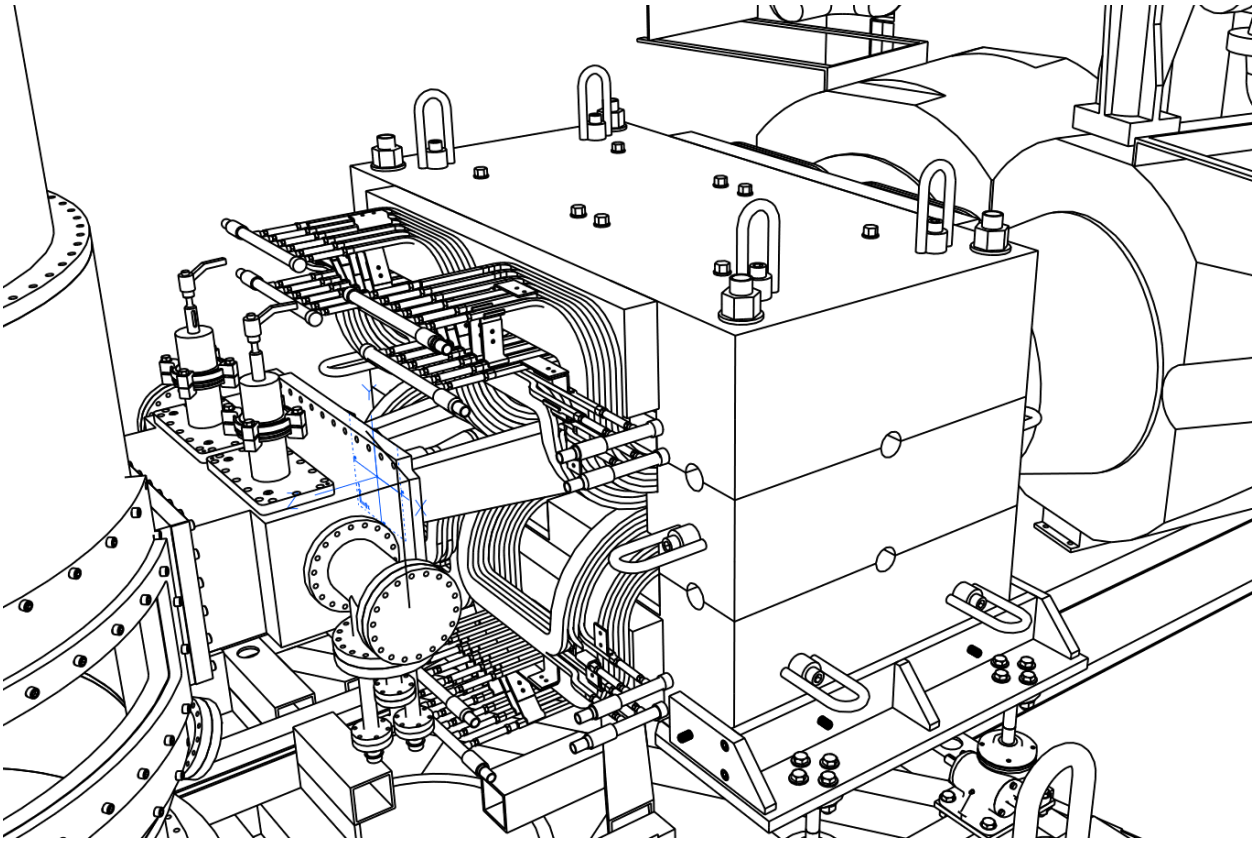

Figure 31: PREX Room Temperature septum magnet, 5° configuration, on the pivot with scattering chamber (foreground left) and HRSs (background right).

Since the PREX experiment relies on the physical separation of the elastic and first excited state (2.6 MeV) peaks of lead just behind the VDC's, a central concern in designing this magnet

for the experiment was the preservation of good hardware resolution. Many iterations of TOSCA [1] calculations followed by raytracing with SNAKE [2] through the TOSCA generated septum maps and the HRS magnets for varying magnet configurations ultimately gave the momentum resolution illustrated in Figure 32. Achieving this very good hardware resolution for PREX will require a special low field configuration of the magnet where the central momentum at 5° will be limited to just over 1 GeV/c. Going to higher fields will require the removal of some iron filler pieces and the addition of a supplemental coil pack. In the higher field configuration hardware momentum resolution will be degraded by roughly a factor of two but central momenta of the order of 2 GeV/c at 5° will be achievable. The running parameters for this septum in the PREX experiment are shown in Table 6.

Table 6: Room temperature septum running parameters for the PREX experiment, 5° and 1.05 GeV/c.

p_0 [GeV/c]	$\int Bdl$	turns	I [A]	current density
1.05	0.45 Tm	380	500	500 A/cm^2

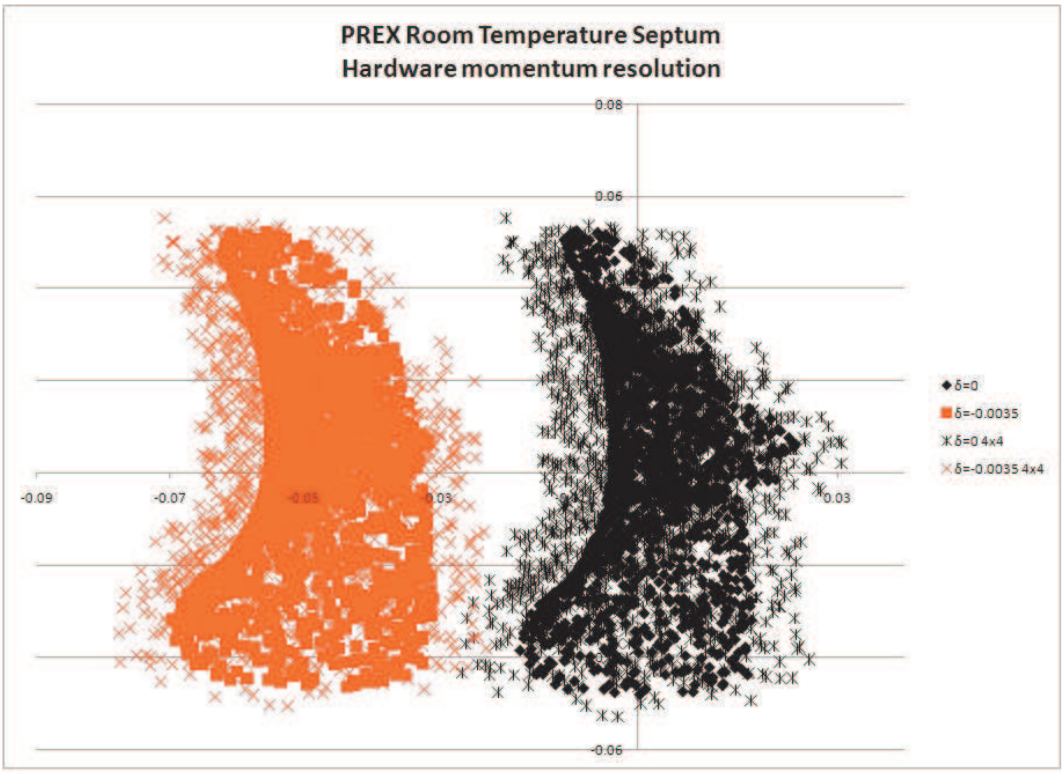

Figure 32: Monochromatic ray clusters traced using SNAKE at the HRS VDC. Black (red) solid symbols are for $\delta = 0$ ($\delta = -0.0035$). x's are the same but with a 4x4 mm raster. The horizontal and vertical axes are dispersive and transverse, respectively. Units are meters.

As of this writing, January 15, 2009, all major components have been designed and are ready to go or are already out for bids. The magnet and attendant systems are scheduled for installation in FY2010.

References

[1] TOSCA, 3-D Non-linear Magnetostatics Computer Program, Vector Fields, Oxford, England

[2] P. Vernin, RPAC (II) CEBAF, January 1987, p.615

4 Summaries of Experimental Activities

4.1 E94-107

High Resolution Hypernuclear 1p-shell Spectroscopy

F. Garibaldi, S. Frullani, J. J. LeRose, P. Markowitz, spokespersons
and
the Hall A collaboration

4.1.1 The experiment

Hypernuclei provide us with a variety of nuclear phenomena. Hypernuclei are unique laboratories for studying the ΛN interaction. Experiment E94-107 started a systematic study of high-resolution hypernuclear spectroscopy on p-shell targets, ^{12}C, ^{9}Be, ^{16}O, providing crucial information complementary to the studies performed with hadron probes and γ-ray spectroscopy. The first part of the experiment on ^{12}C and ^{9}Be targets was performed in January and April-May 2004 in Hall A. The second part of the experiment on ^{16}O was carried out in June 2005. The physics motivation, the experimental challenges and the improvements of the Hall A apparatus (septum magnets, optics, aerogel detectors, RICH detectors, waterfall target) were described in previous Hall A status reports. The update of the status of analysis is presented here.

4.1.2 Present status and outlook

High Resolution Spectroscopy of $^{16}_{\Lambda}$N by K^+ Electroproduction on ^{16}O

The results of $^{12}_{\Lambda}$B by K^+ electroproduction on ^{12}C are published on [6].

Experiment E94-107 used a waterfall target for hypernuclear production on Oxygen nuclei and simultaneously for the measurement of the elementary cross section in p(e, e'K$^+$)Λ.

Kinematics were set to electron detection at 6° for scattered electrons with momentum of 1.44 GeV/c, incident beam energy of 3.66 GeV, virtual photon energy of 2.2 GeV with Q^2 = 0.06 GeV^2. Scattered kaons were detected with momenta of 1.96 GeV/c at 6° .

Figure 33 shows the cross-section for the $^{16}_{\Lambda}$N hypernuclear spectrum produced on Oxygen nuclei at $\theta_{K^+,e} = 6°$. The dotted line is a result of the theoretical calculation using the SLA model for the elementary cross section and J. Millener calculations for the hypernuclear structure. The red line is the fit of the curve with same procedure used for Carbon spectrum. The overall picture shows good agreement between the data and the calculations in terms of positions and relative strength of the levels, as reported in the Table 7. The agreement also provides a upper limit on the charge-dependent effects in hyperon-nucleon interactions. The position of the fourth peak has a significant discrepancy between theory and experiment, providing an indication of very small spin-orbit splitting of the p_Λ orbits.

The waterfall thickness used during the experiment was 75 mg/cm^2. This value was determined using the known cross-section of the elastic reaction on hydrogen.

These results are significantly refined with respect to those published on the previous Hall A Report and presented at HYP 2006 Conference [7]. The differences in the measured cross-sections are mainly due to the precise calculation of the target thickness, significantly different than the previous, expected value which was based on a old calibration performed in a different laboratory. In order to understand and explain the new values of the cross-sections, the calculation of the K^+ optical potential was improved. In details, in the Distorted Wave Impulse Approximation (DWIA), kaon distortion in the final state is usually described by simple first order optical potential

Table 7: Levels and cross sections obtained by fitting the $^{16}\mathrm{O}(e,e'K^+)^{16}_{\Lambda}\mathrm{N}$ spectrum compared with theoretical predictions.

E_x/E_Λ [MeV]	Width [FWHM, MeV]	Cross section [nb/sr^2/GeV]	E_x [MeV]	Wave function	J^π	Cross section [nb/sr^2/GeV]
0.0/13.76 ± 0.16	1.71	1.45± 0.26	0.00	$p_{1/2}^{-1} \otimes s_{1/2\Lambda}$	0^-	0.002
			0.03	$p_{1/2}^{-1} \otimes s_{1/2\Lambda}$	1^-	1.45
6.83 ± 0.06	0.88	3.16 ± 0.35	6.71	$p_{3/2}^{-1} \otimes s_{1/2\Lambda}$	1^-	0.80
			6.93	$p_{3/2}^{-1} \otimes s_{1/2\Lambda}$	2^-	2.11
10.92 ± 0.07	0.99	2.11 ± 0.37	11.00	$p_{1/2}^{-1} \otimes p_{3/2\Lambda}$	2^+	1.82
			11.07	$p_{1/2}^{-1} \otimes p_{1/2\Lambda}$	1^+	0.62
17.10 ± 0.07	1.00	3.44 ± 0.52	17.56	$p_{3/2}^{-1} \otimes p_{3/2\Lambda}$	3^+	2.10
			17.57	$p_{3/2}^{-1} \otimes p_{1/2\Lambda}$	2^+	2.26

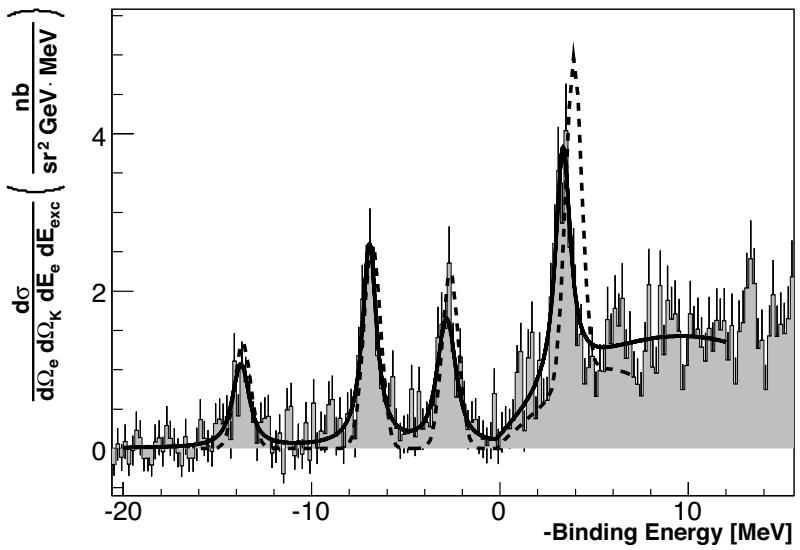

Figure 33: Experimental data for the $^{16}_{\Lambda}\mathrm{N}$ binding-energy spectrum compared with a new theoretical model (dashed curve). The solid curve represents the fit of the data with Voigt functions.

constructed from elementary t-matrices of kaon-baryon scattering. The optical potential used in previous calculation was based an a so-called Martin parametrization that was found to have limitations at the Kaon energy of the E94-107 experiment. Therefore a more realistic model, based on recent CERN and HERA data, with a stronger kaon absorption, is now used and compared with the experimental data, showing a good general agreement. This new optical potential changes the theoretical calculations published on [6], but there is still a good agreement with experimental data, as shown in Figure 34.

The measured Λ binding energy in $^{16}_{\Lambda}\mathrm{N}$, $B_\Lambda = 13.76 \pm 0.16$ MeV obtained from the first peak is

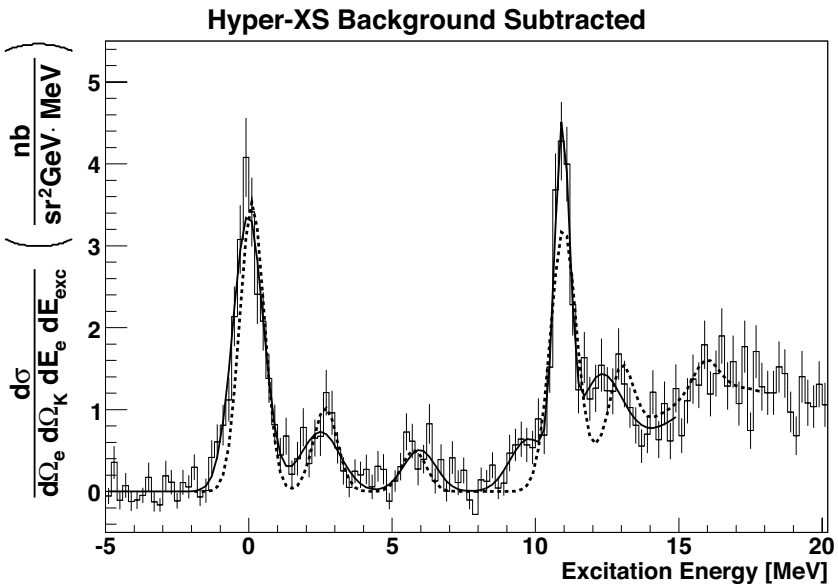

Figure 34: Experimental data for the ${}^{12}_{\Lambda}$B binding-energy spectrum compared with a new theoretical model (dashed curve). The solid curve represents the fit of the data with Voigt functions.

Table 8: Levels and relative strength obtained by fitting the ^{9}Be$(e,e'K^+){}^{9}_{\Lambda}$Li spectrum shown in Fig. 36.

Peak (a. u.)	Strength (a. u.)	Position [MeV]	FWHM [MeV]	Integral (a. u.)
0	19.15 ± 4.89	6.83 ± 0.08	0.52 ± 0.07	19.0
1	14.60 ± 4.39	7.30 ± 0.12	0.52 ± 0.07	14.5
2	14.63 ± 2.37	8.11 ± 0.05	0.50 ± 0.07	14.5
3	12.99 ± 2.40	8.64 ± 0.06	0.53 ± 0.07	12.9
4	11.81 ± 2.02	9.24 ± 0.05	0.45 ± 0.07	11.7

a previously not well known quantity. There are few emulsion events for the heavier p-shell hypernuclei and these events tend to have ambiguous interpretations [5]. Also, the reactions involving the production of a Λ from a neutron are more difficult to normalize. For these reasons, data on the mirror hypernucleus have a difficult interpretation. Therefore the present measurement may help in shedding light on this issue, providing the most precise data point and considering the charge-dependent effect for the other peaks.

The preliminary results on the simultaneous measurement of the elementary reaction on hydrogen also shows a similar agreement between the data (σ=30 nb/sr^2/GeV ± 20%) and the predicted cross section of 36 nb/sr^2/GeV according to the SLA model.

High Resolution Spectroscopy of ${}^{9}_{\Lambda}$Li by K^+ Electroproduction on ^{9}Be

Preliminary results of the ${}^{9}_{\Lambda}$Li are shown in Figure 35.

The first-step analysis shown in Fig. 35 is driven by a peak-search and χ^2 minimization procedures. A second step is the attempt of fitting the spectrum according to the expected structure of the energy levels, as shown in Fig. 36.

This spectrum would be able to provide information on the spin-spin part of the ΛN potential,

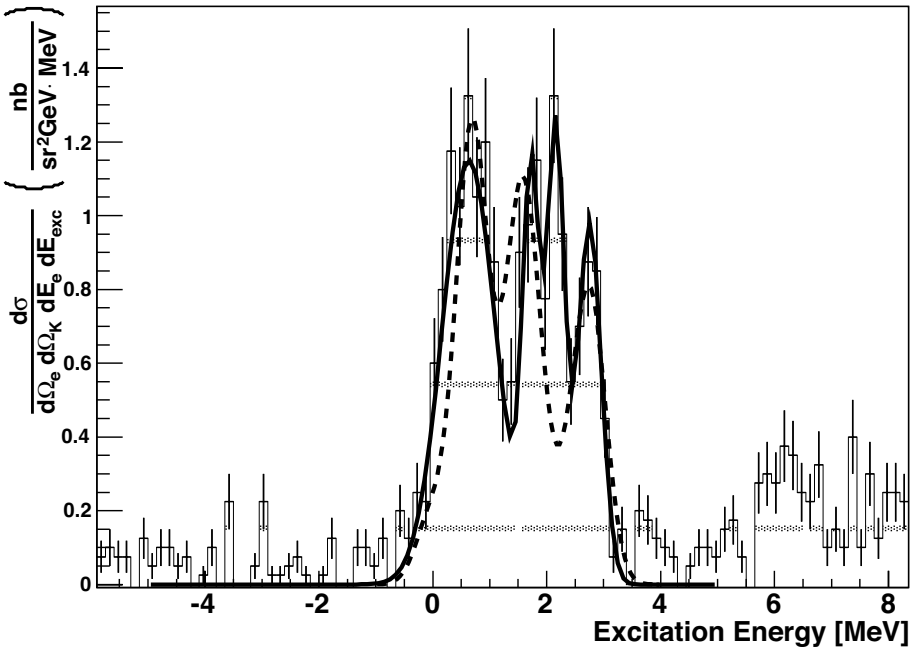

Figure 35: Preliminary data for $^{9}_{\Lambda}$Li. The dashed line represents a theoretical model, the solid curve is a fit performed with Voigt functions as for the previous data. The number of peaks to be fitted is determined by a peak-search algorithm.

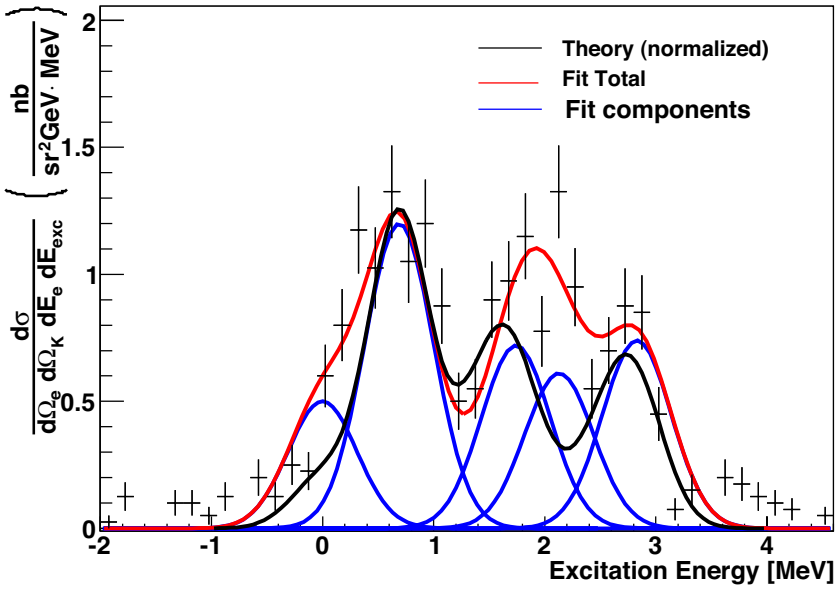

Figure 36: Preliminary data for $^{9}_{\Lambda}$Li. The number of peaks to be fitted is determined according to the theoretical models and to the χ^2 minimization.

the most interesting term. The choice of five peaks is guided by the χ^2 test and takes into account the theoretical predictions. Continuous improvements in the analysis is presently going and Fig. 36 has to be considered as a intermediate step, even if close to final results.

References

[1] M. Sotona and S. Frullani, Prog. Theor. Phys. Suppl. **117**, 151 (1994).

[2] J.C. David, C. Fayard, G.-H. Lamot, B. Saghai, Phys. Rev. C **53**, 2613 (1996); T. Mizutani, C. Fayard, G.-H. Lamot, B. Saghai, Phys. Rev. C **58**, 75 (1998).

[3] M. Ukai *et al.*, Phys. Rev. C **73**, 012501 (2006).

[4] O. Hashimoto and H. Tamura, Prog. Part. Nucl. Phys. **57**, 405 (2006).

[5] D. H. Davis, in *LAMPF Workshop on* (pi, K) *Physics*, edited by B. F. Gibson, W. R. Gibbs, and M. B. Johnson, AIP Conf. Proc. **224**, 38 (1991).

[6] M. Iodice *et al.*, *Phys Rev Lett* 99, 052501 (2007).

[7] J. J. LeRose *et al.*, *Nucl Phys A* 804, 116-124 (2008).

4.2 E97-110

The GDH Sum Rule, the Spin Structure of ^{3}He and the Neutron using Nearly Real Photons

J.-P. Chen, A. Deur, F. Garibaldi, spokespersons
and
the E97-110 Collaboration.

The goal of the experiment is to measure the generalized Gerasimov-Drell-Hearn integral (GDH) and moments of the neutron and ^{3}He spin structure at low Q^2 where Chiral Perturbation Theory can make rigorous predictions.

The experiment. The experiment ran in April-May and July-August 2003. The first part of the experiment (low Q^2, April-May 2003) acquired data with a mis-wired septum magnet. The septum was repaired in June and the experiment was completed in July-August.

Analysis Progress. V. Sulkosky (JLab) worked on improving the interpolation of the data from constant beam energy/angle to constant Q^2. This work is essentially completed and allowed us to obtain preliminary results. Figure 37 shows the spin structure functions g_1 and g_2 on ^{3}He at constant Q^2. Figs. 38 and 39 show their integrals Γ_1^n and Γ_2^n, extracted for the neutron.

J. Yuan (Rutgers University) finalized the VDC multitrack study.

R. Pandolfi (summer student, Randolf Macon College), under the supervision of V. Sulkosky, studied the various backgrounds seen in the E97-110 data (collimator punch-through, 2-step process,...). The conclusion of this work is that these backgrounds can be removed thanks to our analysis method (difference of polarized cross sections) together with the systematic empty reference cell measurements at the numerous E97-110 kinematic settings. The systematic uncertainties were studied as well. A. Deur and T. Holmstrom were also involved in this work.

R. Pandolfi worked also, under the supervision of T. Holmstrom, on the calculation of statistical error bars for data taken under large rates and large trigger prescale factors. A. Deur and V. Sulkosky were also involved. Work is in progress to finalize this analysis.

Jaideep Singh, after providing preliminary radiative corrections for E97-110, is resuming his work on it. An important part is to reach a good understanding of the quasi-elastic wings and tail, whose contributions are enhanced because of the $1/\nu$ weighting in the GDH integral. These effects are even more important for higher moments, such as generalized spin polarizabilities.

Hai-jiang Lu, who is conducting the first period analysis will come to JLab in early 2009 to continue this work.

Remaining tasks. Remaining tasks for the first paper are:

- Complete the radiative corrections (J. Singh)
- Complete the polarimetry analysis (J. Singh. This task is nearly completed)
- Verify the polarimetry analysis and radiative corrections by analyzing the asymmetries and cross sections for the elastic kinematics.
- Finalize the acceptance correction (V. Sulkosky).

Outlook. Our goal is to publish the first paper in 2009, including only the data from the second period. The paper will concentrate on the GDH sum and the first moments on neutron.

Work for subsequent papers includes the completion of the first period analysis, extraction of higher moments for the neutron and both first and higher moments for ^{3}He.

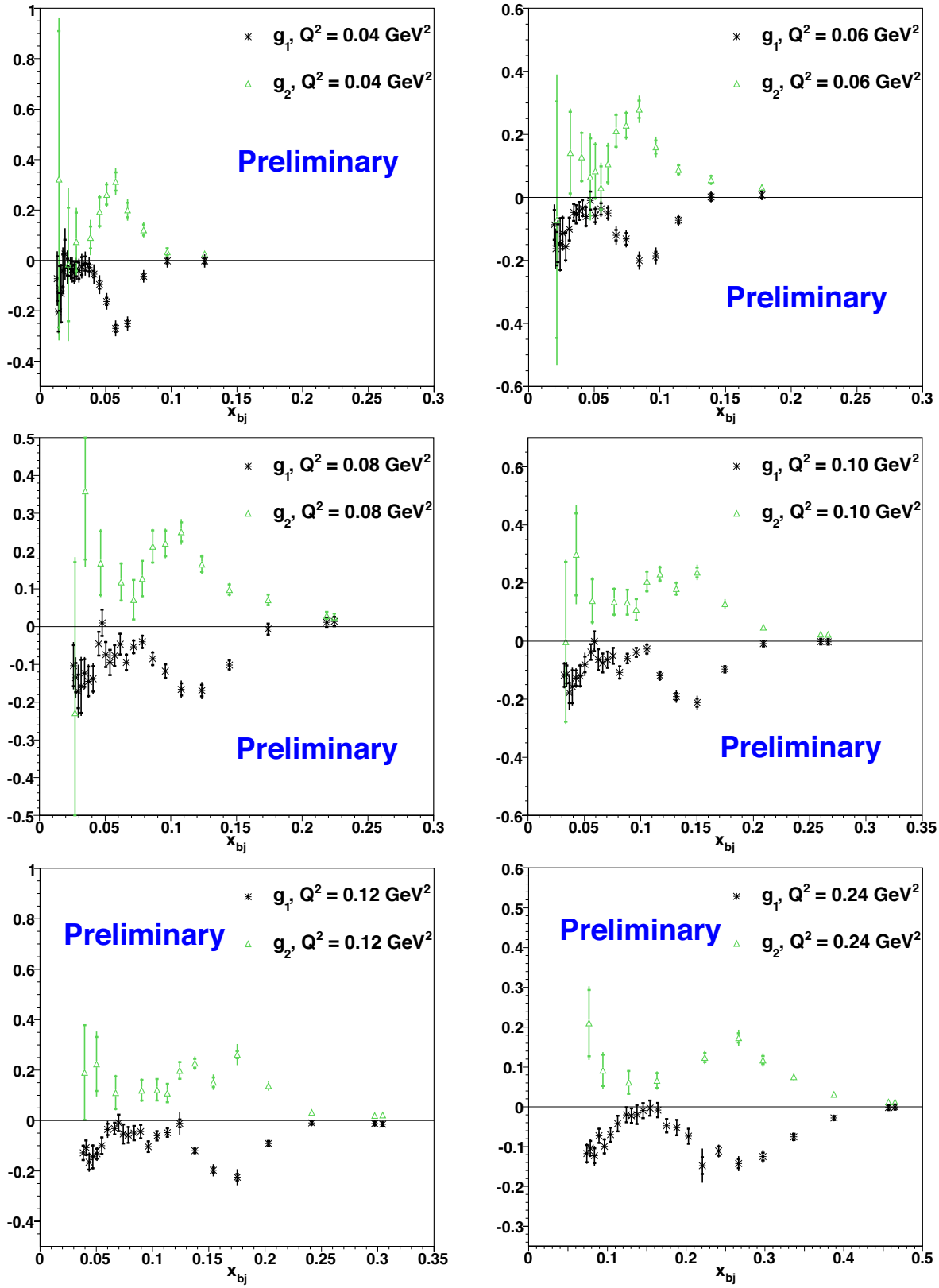

Figure 37: Preliminary E97-110 results on $g_1^{^3\mathrm{He}}$ and $g_2^{^3\mathrm{He}}$, interpolated to constant Q^2 values.

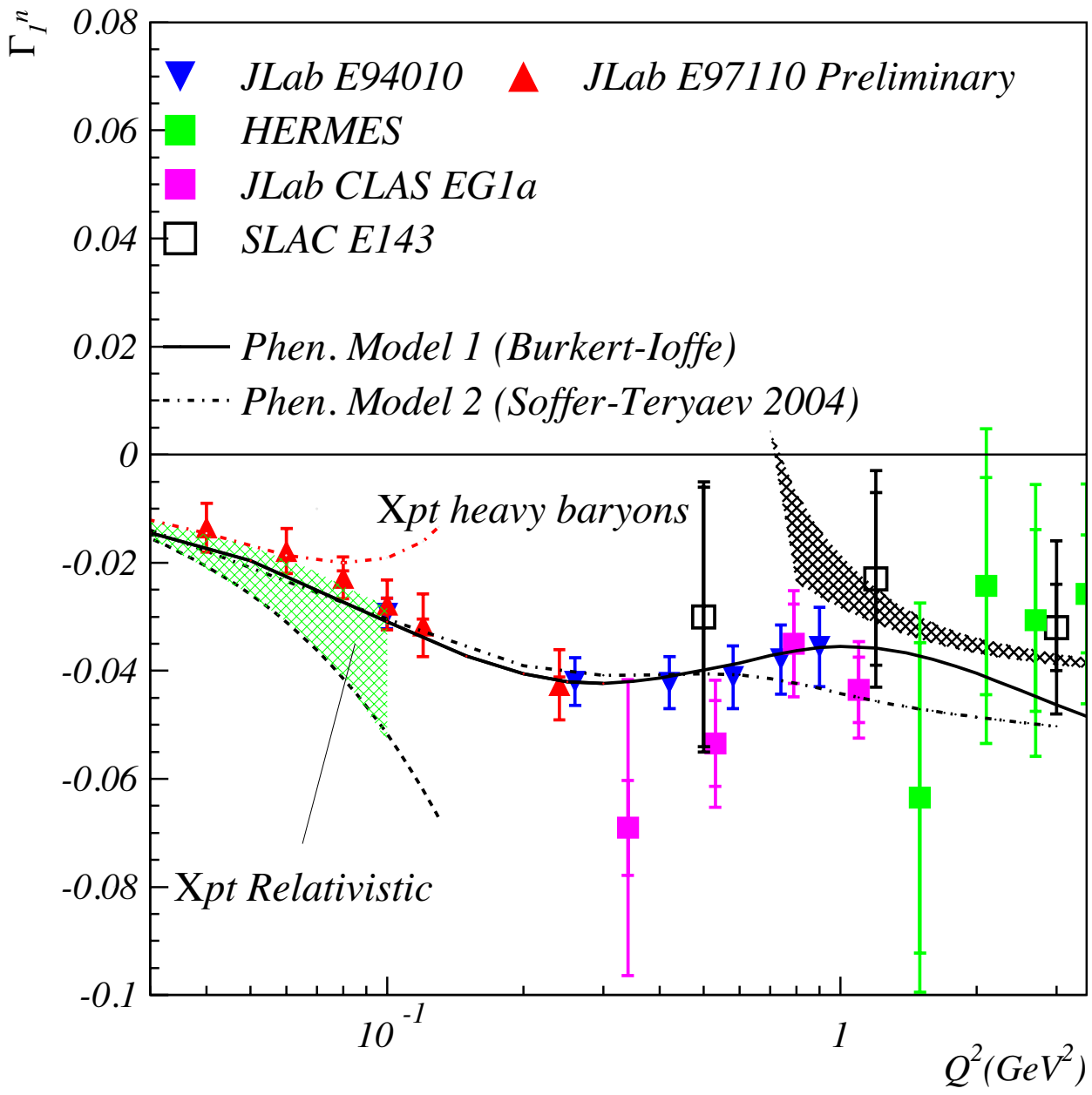

Figure 38: Preliminary E97-110 results on Γ_1^n, together with the published results from SLAC E143, HERMES, Hall A E94-010 and CLAS EG1a.

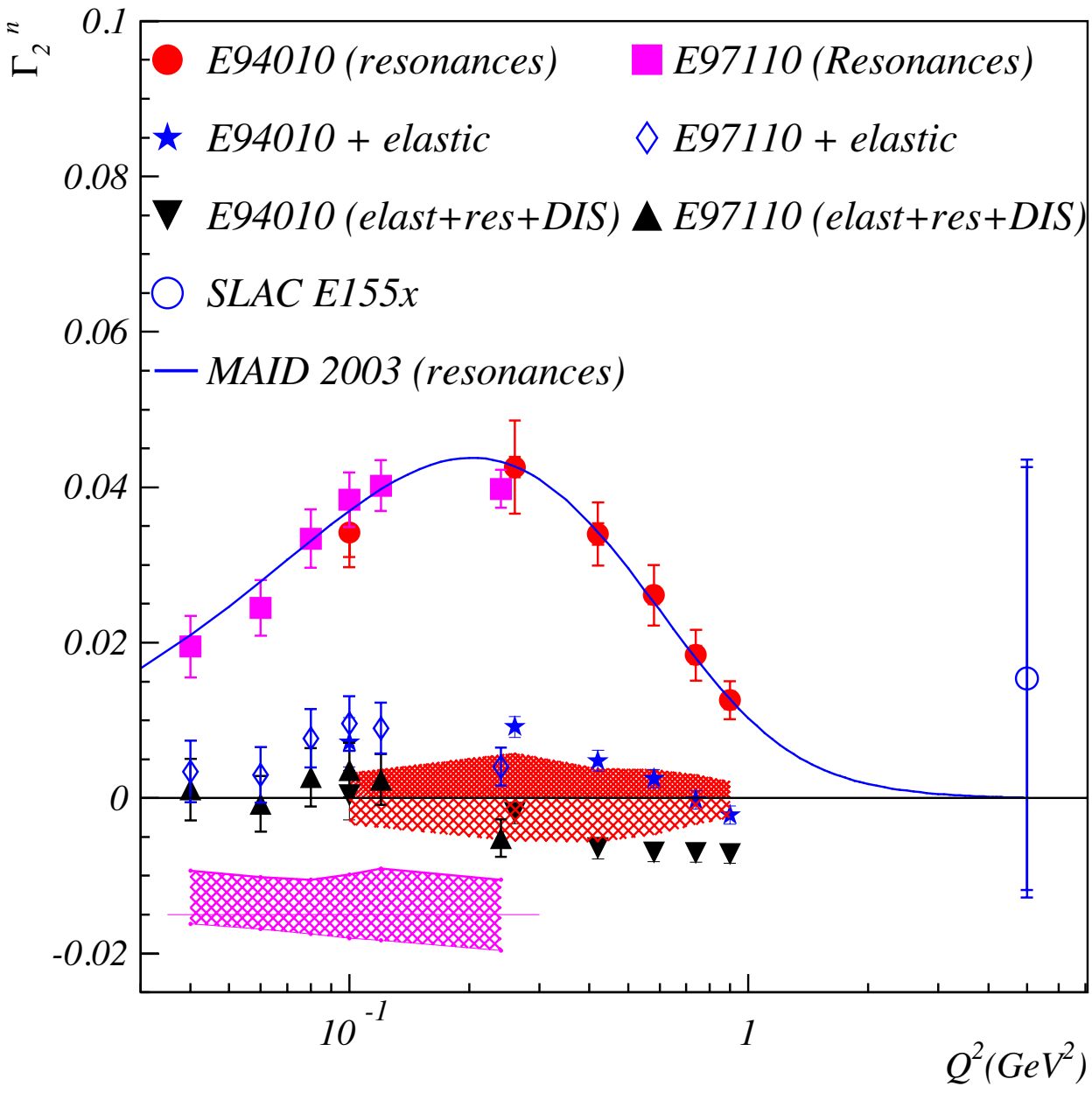

Figure 39: Preliminary E97-110 results on Γ_2^n, together with the published results from Hall A E94-010.

4.3 E00-102

Testing the Limits of the Single-Particle Model in $^{16}O(e,e'p)$

A. Saha, W. Bertozzi, L.B. Weinstein, and K. Fissum, spokespersons,
and
the Hall A Collaboration.
contributed by J. L. Herraiz.

Experiment E00-102 is a continuation of the Hall A experiment E89-003: A Measurement of the Cross Section, R_{LT}, and A_{LT} for the $^{16}O(e,e'p)$ Reaction. Experiment E89-003 made measurements at energy and momentum transfers of $\omega = 0.445$ GeV and $Q^2 = 0.8$ GeV^2 respectively, up to $p_m = 0.345$ GeV/c [1, 2, 3]. In E00-102, we expanded on the existing measurements up to $p_m = 0.755$ GeV/c at $\omega = 0.449$ GeV and $Q^2 = 0.902$ GeV^2.

4.3.1 Objectives

The goals of these measurements were to determine:

- the limits of validity of the single-particle model of valence-proton knockout,
- the effects of relativity and spinor distortion on valence-proton knockout using the diffractive character of the A_{LT} asymmetry, and
- the bound-state wave function and spectroscopic factors for valence-proton knockout.

The cross section will be determined from our measurements from $p_m = -0.515$ GeV/c to $p_m = 0.755$ GeV/c in order to determine where single-nucleon knockout calculations fail and if two-nucleon effects become important. R_{LT} and A_{LT} will be separated for p_m up to ± 0.515 GeV/c to further test relativistic DWIA calculations.

4.3.2 Experimental Setup

Data were taken at a fixed beam energy of 4.620 GeV, $q = 1.066$ GeV/c, and $\theta_q = 56.22°$. Throughout the entire experiment, the electron arm (HRS-L) was fixed at 12.5° with a central momentum of 4.121 GeV/c. This allowed it to be used as a luminosity monitor. The hadron arm (HRS-R) angle was varied from 28.3° to 96.1° to cover the necessary missing-momentum range. These kinematics are shown in Fig. 40. Both detector stacks were used in their standard configurations (see Fig. 41). Each stack contained an additional S0 scintillator for checking trigger efficiency, and the HRS-L contained a pion rejector which was used for e/π separation.

The target employed was the Hall A self-normalizing three-foil waterfall target [4, 5]. Each water foil was approximately 200 mg/cm^2 thick and was separated by 25.4 mm from the other foils. The foils were positioned at an angle of 57.4° with respect to the beam direction, as shown in Fig. 42. Electron scattering from the hydrogen in the water molecule enabled precise calibrations of the experimental apparatus to be made. Further, these measurements also made the normalization of the measured $^{16}O(e,e'p)$ cross section to known $^{1}H(e,e'p)$ and $^{1}H(e,e)$ cross sections possible.

Detector calibrations, beam-position determinations, and beam-energy calibrations have been performed. Optimized detector maps have been created, and the analysis of the spectrometer mispointing has been completed. The water-foil thicknesses have been determined by comparing $^{16}O(e,e'p)$ yields to those obtained from a solid BeO target of a well-known thickness [6].

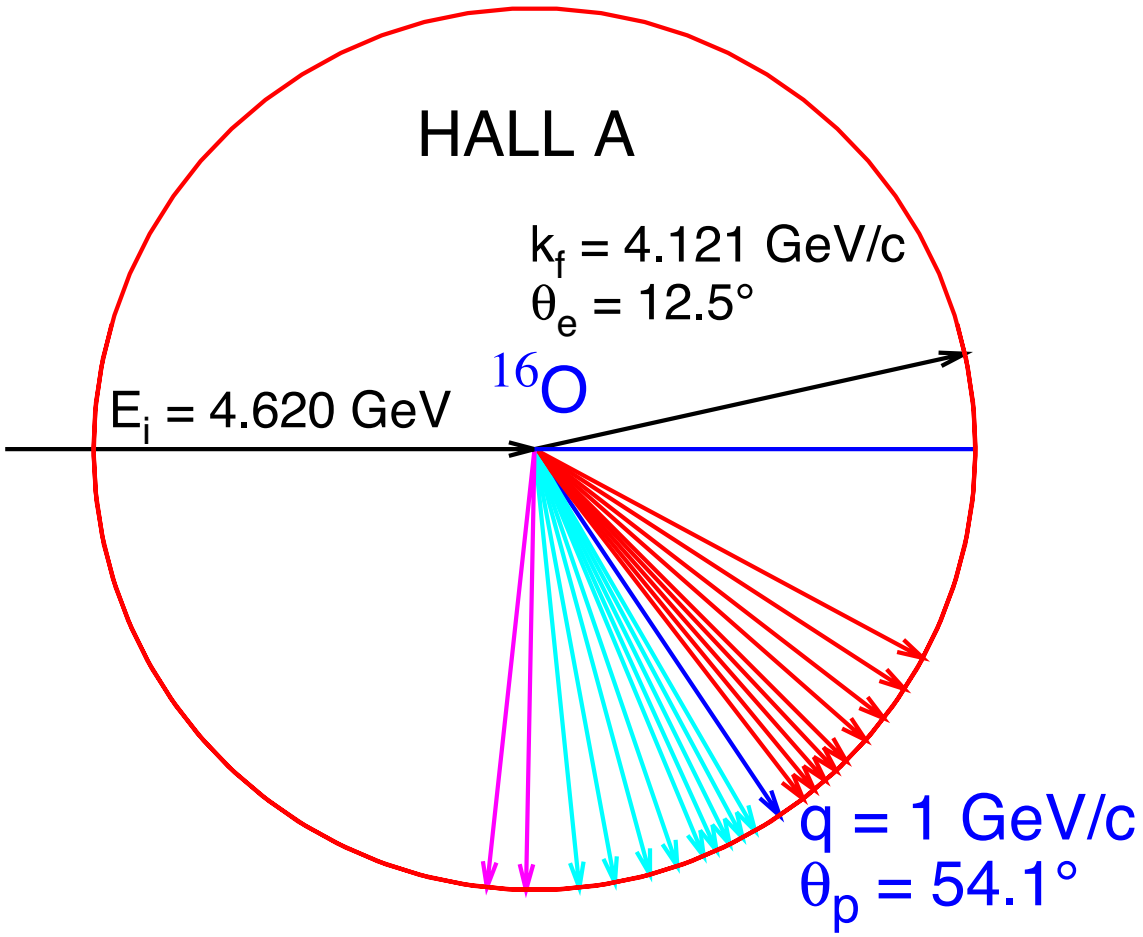

Figure 40: E00-102 kinematics. The beam energy was 4.620 GeV and the HRS-L was fixed at 12.5° with a central momentum of 4.121 GeV/c. The HRS-R was rotated around the direction of parallel kinematics to cover the necessary missing-momentum range.

4.3.3 Previously Developed Analysis Tools

Extensive progress has been made at ODU in adapting the E00-102 analysis [7] to the new ROOT/C++ Hall A Analyzer. This included transferring the optics calibration database used in ESPACE to the new format, creating a model of the waterfall target to calculate energy-loss corrections, and incorporating the LeRose R-functions to enable detector-acceptance cuts. The results from the new Hall A Analyzer have been sufficiently checked against both the ESPACE results and the data so that we are now confident in its accuracy. We are thus ready to analyze all the data acquired during the experiment.

In collaboration with LU, UCM has integrated a fully unfactorized RDWIA model [8] into the MCEEP simulation package. An interpolable hypercube containing nuclear response functions calculated by Udias was generated over a broad range of kinematics and used to weight MCEEP events [9]. This allowed the calculation to be averaged correctly over the finite acceptance of the spectrometers. MCEEP simulations may now be converted into ROOT files to ease the comparison with the data.

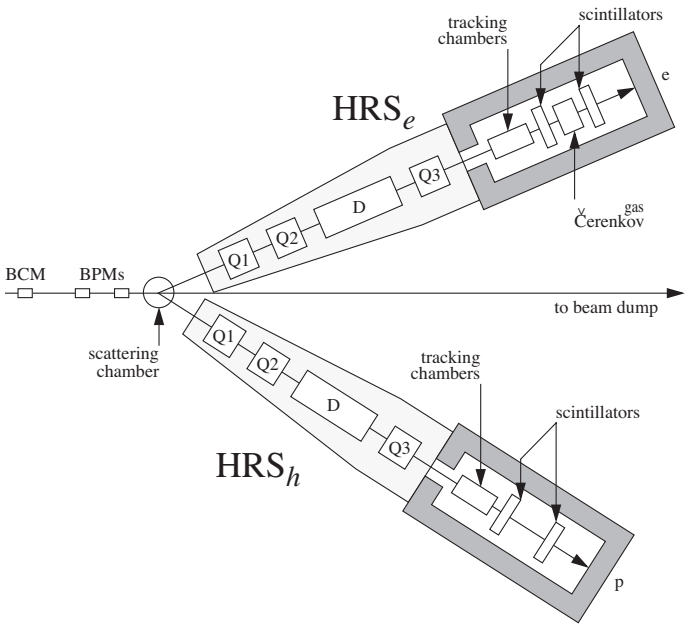

Figure 41: E00-102 HRS. Detector configurations for the High Resolution Spectrometers during the E00-012 experiment. The A1, A2, and the RICH detector were not of use in HRS-L while the Gas Cerenkov detector was not used in HRS-R.

4.3.4 Recently Developed Analysis Tools

A C++ macro has recently been jointly developed by ODU and UCM to obtain the cross section from the ROOT files containing the data events obtained with the Hall A Analyzer and the ROOT files containing the simulated events obtained with MCEEP. This macro performs the R-function cuts, the luminosity normalization, the efficiency correction, and the phase-space normalization of both the data files and the simulated files. The macro also applies a cut in missing energy which enables the $1p_{1/2}$, $1p_{3/2}$, or $1s_{1/2}$ shells to be selected. Further, the σ_{ep} factor necessary to determine reduced cross section is also evaluated based on the prescription of de Forest [10]. A step-by-step overview of the analysis to date is shown in Fig. 43.

The output of the C++ macro contains histograms of the 5-fold differential cross section and reduced cross section for both the data and the simulation for single-proton removal from ^{16}O. The cross section so obtained is a function of the physical variables q, ω, p_m, and the out-of-plane angle

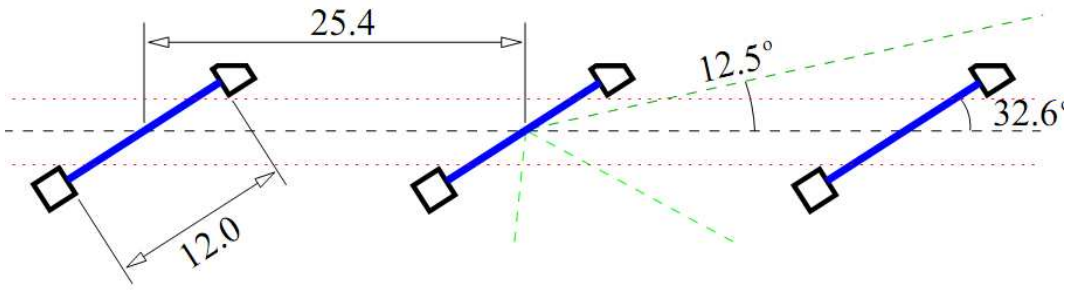

Figure 42: E00-012 waterfall target.

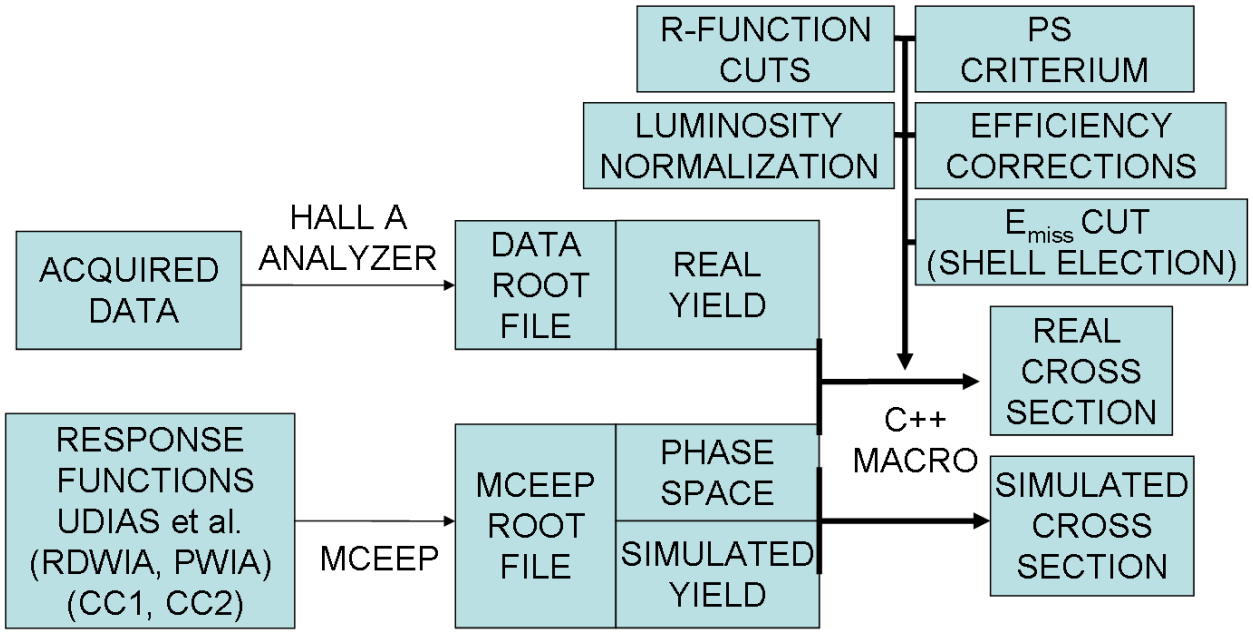

Figure 43: An illustration of the steps followed during the analysis of the E00-102 data.

between the reaction plane and the ejectile plane ϕ. The last step in the data analysis is to determine the differential cross section and the longitudinal-transverse asymmetry A_{LT} as a function of the missing momentum p_m from these multidimensional histograms as shown in Equation 2

$$\frac{d^5\sigma}{d\omega d\Omega_e d\Omega_p}(q,\omega,\phi,p_m) \rightarrow \begin{cases} \frac{d^5\sigma}{d\omega d\Omega_e d\Omega_p}(p_m) \\ A_{LT}(p_m) \end{cases} \tag{2}$$

At the moment, different approaches to obtaining the final result are being tested. These include

- using reduced acceptances in q, ω, and ϕ. This method results in the expected central-value results for these variables at the expense of wasting an unacceptable amount of data,
- using the reduced five-fold differential cross section to decrease (or even remove) the dependence of the five-fold differential cross section on q and ϕ, while retaining reduced acceptance cuts in ϕ, and
- using the reduced five-fold differential cross section together with the full range of ϕ to extract information about the response functions using a fitting procedure.

4.3.5 Latest Simulations

Some effort has recently been devoted to include radiation in MCEEP simulations in a manner that better reproduces the radiative tails of the data. Figure 44 shows a missing-energy spectrum with two peaks corresponding to the removal of $1p_{1/2}$ and $1p_{3/2}$ protons from ^{16}O. Good agreement between data and simulation is demonstrated.

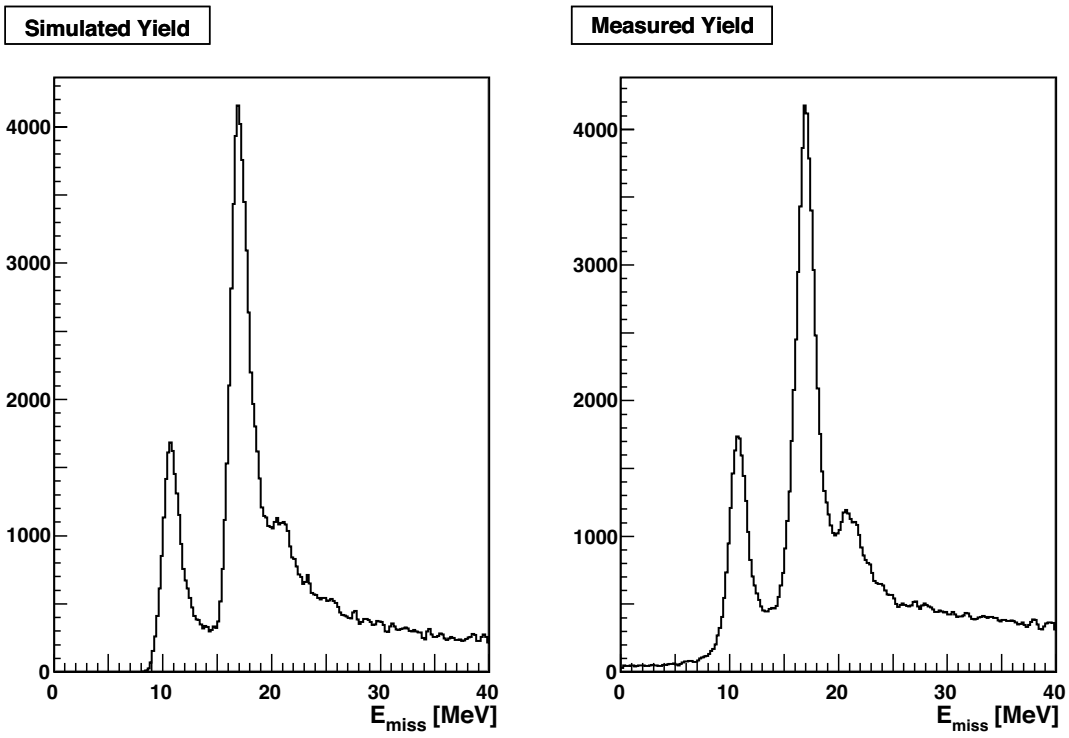

Figure 44: Missing-energy spectra showing two peaks corresponding to the removal of $1p_{1/2}$ and $1p_{3/2}$ protons from ^{16}O. (Left) Simulation (Right) E00-102 data. Good agreement between data and simulation is demonstrated.

The simulation for all kinematical settings for all foils and all shells has been performed. In Fig. 45, the cross section and the reduced cross section for the $1p_{1/2}$ shell as a function of p_m is displayed. It should be noted that all bins in (q, ω) are considered in this plot, so some disagreement between kinematics is expected because points with the same p_m from different kinematics correspond to different values of (q, ω). By instead using the reduced cross section, most of the dependence on (q, ω) may be removed, and the agreement between different kinematics improves markedly. This may be seen by comparing this figure with the preliminary results obtained at LU [11] shown in Fig. 46.

4.3.6 Latest Results

In order to check the MCEEP simulations and the C++ macro, data from our kinD measurement at $p_m = \pm 175$ MeV/c have been carefully studied. Figure 47 shows the reduced cross section obtained using the kinD data compared to the simulation. The plot shows 9 histograms of reduced cross section as a function of p_m corresponding to 9 different bins in (q, ω). Also shown is the dependence of $d^5\sigma$ with ϕ and p_m.

References

[1] W. Bertozzi, K.Fissum, A. Saha, and L. Weinstein, spokespersons, JLab Experiment E89-003 Study of the Quasi-Elastic (e,ep) Reaction in ^{16}O at High Recoil Momentum.

[2] J. Gao *et al.*, Phys. Rev. Lett. **84**, 3265 (2000).

[3] N. Liyanage *et al.*, Phys. Rev. Lett. **86**, 5670 (2001).

[4] F. Garibaldi *et al.*, Nucl. Instum. Methods. A **314**, 1 (1992).

[5] E. Cisbani *et al.*, A Waterfall Target System for Hall A at JLab, INFN/ISS 97/04 (1997).

[6] B. Reitz *et al.*, E00102 status report, (2005).

[7] J. Lachniet, private communication.

[8] J.M. Udias *et al.*, Phys. Rev. Lett. **83**, 5451 (1999).

[9] J.L. Herraiz, Jefferson Lab Technote JLAB-TN-07-068.

[10] T. de Forest, Jr., Nucl. Phys. A **392**, 232 (1983).

[11] M. Andersson, Lic. Thesis, University of Lund (2005).

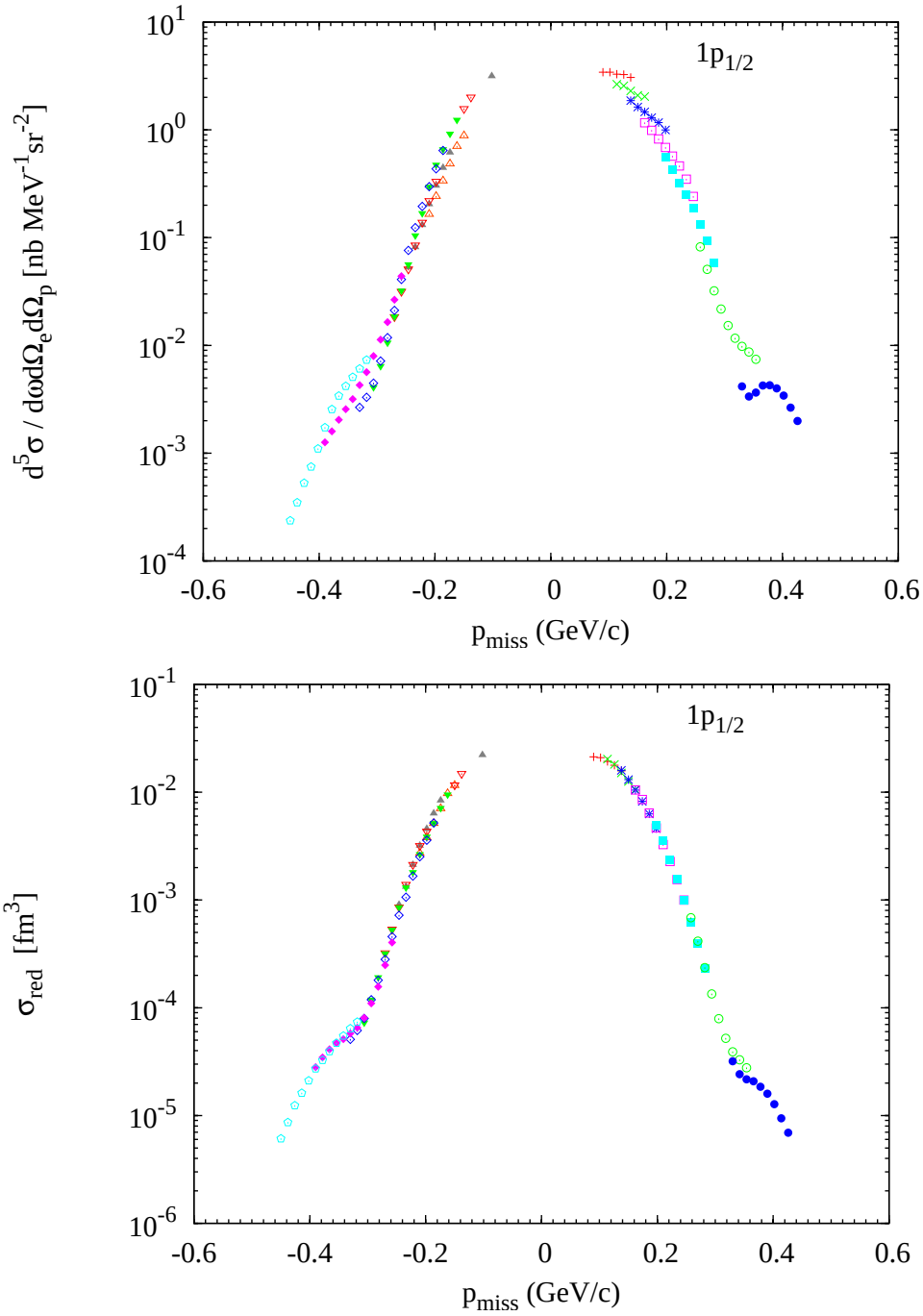

Figure 45: (Top) Simulated cross section (Bottom) Simulated reduced cross section. Results correspond to MCEEP simulations based on RDWIA CC2 response functions for the removal of a single proton from the $1p_{1/2}$ shell. Each kinematics has been assigned a different color.

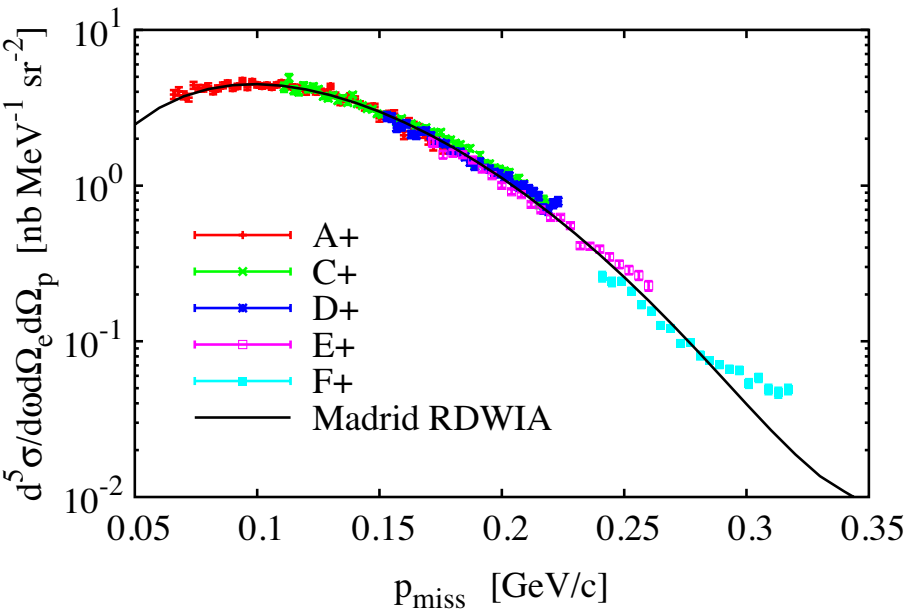

Figure 46: Preliminary cross section obtained at LU [11].

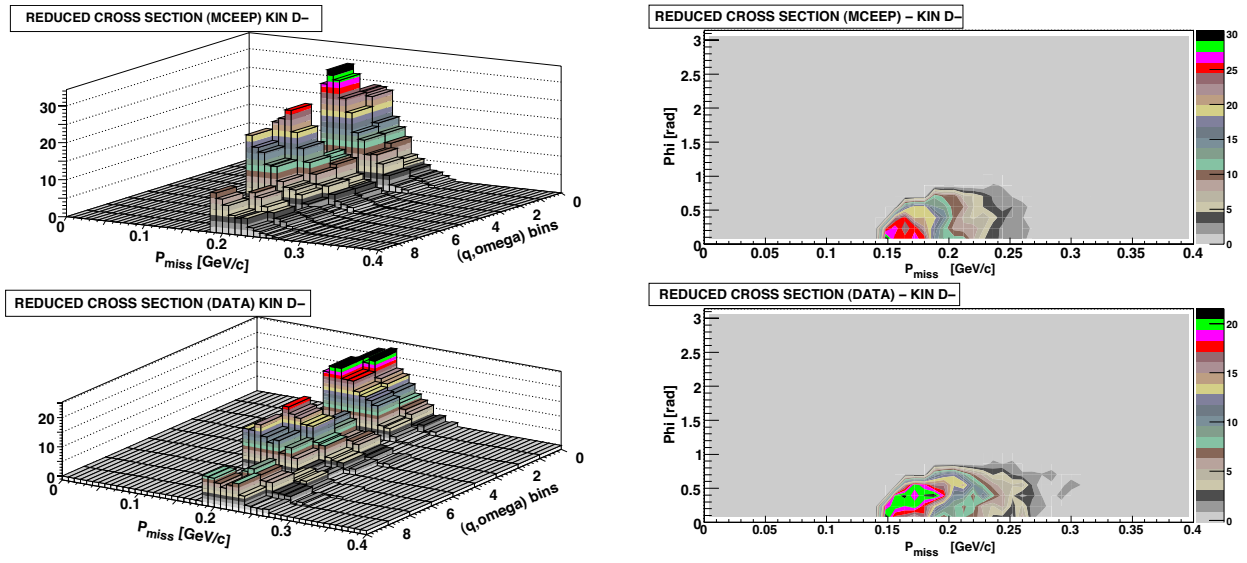

Figure 47: (Left) Reduced cross section for Kinematics D- as a function of missing momentum for 9 different bins in q and ω; (Right) Reduced cross section as a function of out-of-plane angle and the missing momentum.

4.4 E01-015

Short-Range Correlations

S. Gilad, D. Higinbotham, E. Piasetzky, J. Watson and S. Wood, spokespersons
P. Monaghan, R. Shneor and R. Subedi, Ph.D. students

The structure of nuclei is determined by the nature of the strong force: strong repulsion at short distances and strong attraction at moderate distances. This force, which binds the nucleons in the nucleus while also keeping them from collapsing, makes the nucleus a fairly dilute system. This allowed calculations that treated the nucleus as a collection of hard objects in a mean field to describe many of the properties of nuclear matter. Of course, this simple picture of the nucleus is inaccurate, as the nucleons should be thought of as waves that can strongly overlap for short periods of time.

The recent inclusive experiments have shown that about 20% of all nucleons in carbon are in such a state at any given time [1, 2]. These states of strongly overlapping wave functions are commonly referred to as nucleon-nucleon short-range correlations. It is predicted that these correlations lead to, for short periods of time, local densities in the nucleus that are several times higher than the average nuclear density of 0.17 GeV/fm^3. These densities are comparable to those predicted in the core of neutron stars; thus, isolating the signal of short-range correlated nucleons may lead to a deeper understanding of all cold dense nuclear systems, whether extremely small, such as helium nuclei, or extremely large, such as neutron stars.

The distinctive experimental features of two-nucleon short-range correlations are the large back-to-back relative momentum and small center of mass momentum of the correlated pair, where large and small are relative to the Fermi sea level of about 250 MeV/c. This is shown schematically in Fig. 48, where a virtual photon is absorbed by one nucleon in a correlated pair, causing both nucleons to be emitted from the nucleus. Due to the large strength of the nucleon-nucleon interaction at small distances, the relative motion in the pair is expected to be the same in all nuclei, though the absolute probability of a correlation grows with density, with the probability of a nucleon to be part of a pair reaching 25% for iron and heavier nuclei.

Isolating the signal of the short-range correlation initial state has been extremely difficult at low and medium energies, as other processes, such as final state interactions and meson exchange currents mimic the effect. Recent progress has been made using modern accelerators with high luminosity, high momentum transfer and kinematics where competing mechanisms are suppressed. For electron scattering, this corresponds to luminosities of 10^{-37} cm^{-2}s^{-1}, a four-momentum transfer, $Q^2 > 1$ GeV^2 and focusing on kinematics of Bjorken $x = Q^2/2m\omega > 1$, where ω is the beam energy minus the scattering electron energy.

In these kinematics, removing one fast nucleon from the nucleus, using a high-momentum probe, effectively breaks a pair and releases the second nucleon of the correlation. The experiment, which measured ^{12}C$(e, e'pp)$ and ^{12}C$(e, e'pn)$ reactions, showed that recoiling nucleons with a momentum above the Fermi sea level in the nucleus are part of a correlated pair, both observed the same strength of proton-neutron correlations [3]. The was also this confirms that the process is accessing a universal property of nuclei not related to the probe [4]. The E01-015 experiment was also able to observe the proton-proton pairs and, with matched acceptance detectors, determine the ratio of neutron-proton to proton-proton pairs to be nearly 20 as shown in Fig. 49. Calculations explain the magnitude of this neutron-proton to proton-proton ratio as being due to the short-range tensor part, or nucleon-nucleon spin dependent part, of the nucleon-nucleon force[5, 6, 7].

Future inclusive short-range correlation experiments will improve the statistics of the $x > 2$ data to definitely show whether or not there is a second scaling, as well as use targets such as

Calcium 40 and 48 to measure the dependence on the initial state proton-neutron ratio. The future exclusive experiments will focus on ^{4}He (a nucleus where both full and mean field calculations can come together) and push the limits of the recoil momentum to further extend our understanding of the repulsive part of the nucleon-nucleon potential.

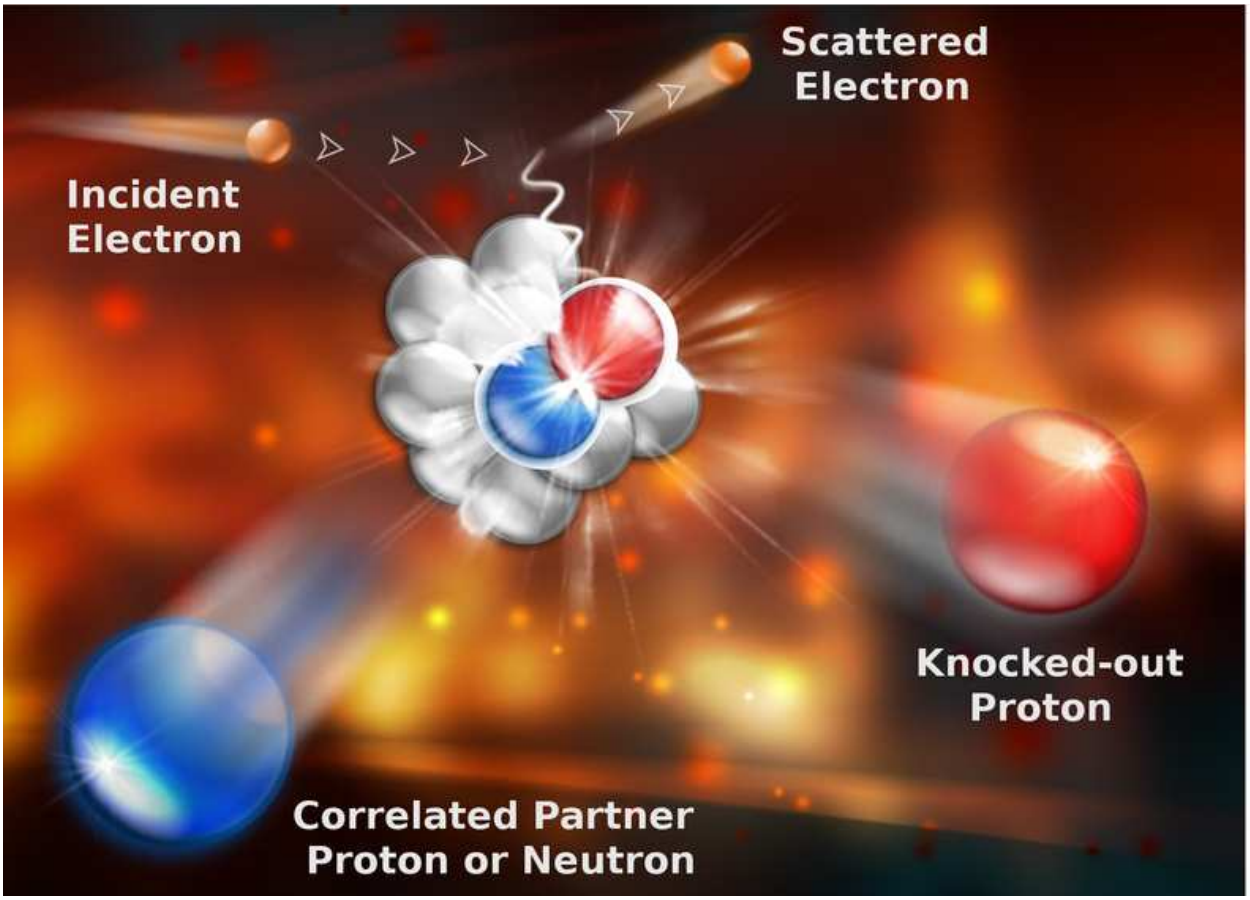

Figure 48: Shown is a diagram of a short-range correlation reaction. By selecting high Q^2, $x > 1$, and missing momentum well beyond the Fermi momentum of nucleons in the nucleus, as shown in the cartoon, knocking-out one proton causes a high momentum correlated partner nucleon to be emitted from the nucleus while leaving the rest of the system relatively unaffected.

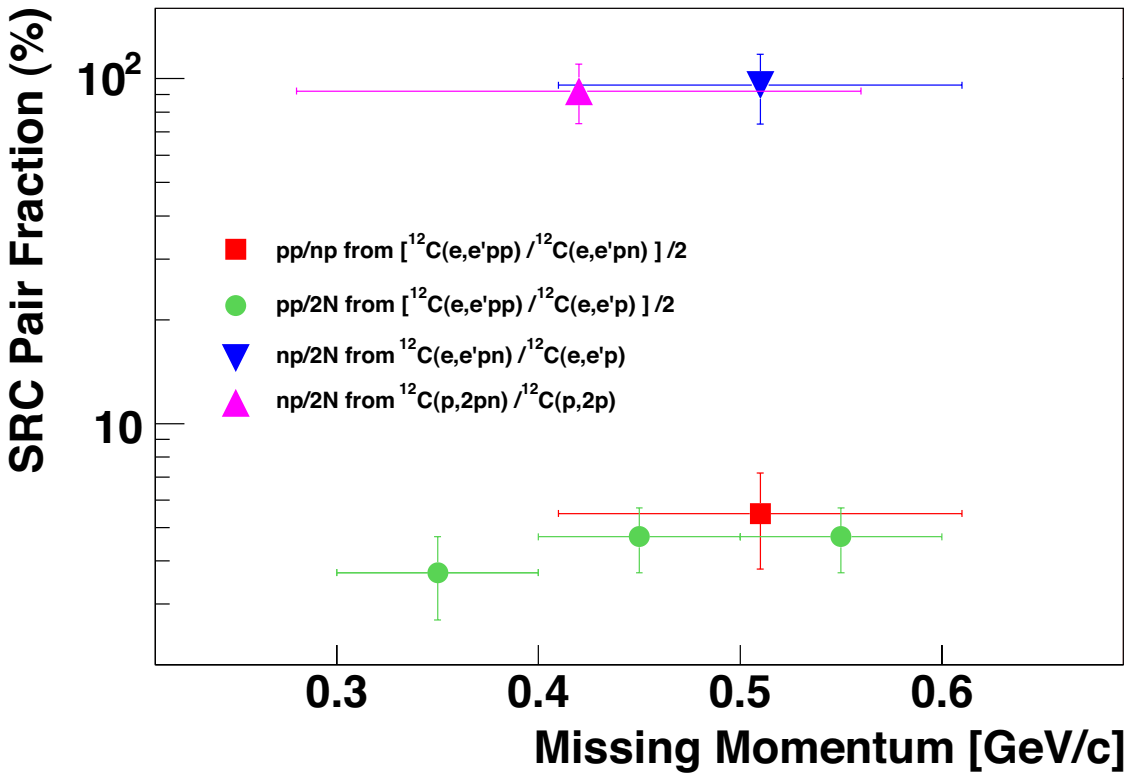

Figure 49: Shown are the fractions of short-range correlated pair combinations in ^{12}C as obtained from the Jefferson Lab $(e, e'pp)$ and $(e, e'pn)$ reactions, as well as from Brookhaven $(p, 2pn)$ data. The results agree with the interpretation of the inclusive data, while also showing the complete dominance of proton-neutron pairs over other pair types.

References

[1] K. S. Egiyan *et al.*, Phys. Rev. C **68**, 014313 (2003).

[2] K. S. Egiyan *et al.*, Phys. Rev. Lett. **96**, 082501 (2006).

[3] R. Subedi *et al.*, Science **320**, 1476 (2008).

[4] E. Piasetzky, M. Sargsian, L. Frankfurt, M. Strikman and J. W. Watson, Phys. Rev. Lett. **97**, 162504 (2006).

[5] M. M. Sargsian, T. V. Abrahamyan, M. I. Strikman and L. L. Frankfurt, Phys. Rev. C **71**, 044615 (2005).

[6] R. Schiavilla, R. B. Wiringa, S. C. Pieper and J. Carlson, Phys. Rev. Lett. **98**, 132501 (2007).

[7] M. Alvioli, C. Ciofi degli Atti and H. Morita, Phys. Rev. Lett. **100**, 162503 (2008).

4.5 E02-013

Measurement of the Neutron Electric Form Factor G_E^n at High Q^2

G. Cates, N. Liyanage, and B. Wojtsekhowski, spokespersons, and
the E02-013 and the Hall A Collaborations.
Contributed by S. Riordan

4.5.1 Introduction

Nucleon form factors contain crucial information on the structure of nucleons, providing insight into the underlying processes of QCD. They are a useful testing ground for fundamental hadron models and are currently a crucial source of information in the development of the parameterization of generalized parton distributions [1, 2].

Traditionally, the electric form factor of the neutron, G_E^n, has been the most difficult to measure of the four nucleon form factors. This is due to the relative smallness of G_E^n as the neutron is an overall neutral particle, and the fact that neutrons to be studied in medium energy electron scattering experiments must be bound in a nucleus, typically deuterium or ^{3}He. Prior to E02-013, precision data on G_E^n was limited to momentum transfers of Q^2 less than 1.5 GeV^2. This missing piece has hindered the reliable separation of the Dirac and Pauli form factors for the neutron, F_1^n and F_2^n, which contain unpolarized and polarized transverse structure of the neutron in the infinite momentum frame [3, 4], and of the u and d valence quark form factors.

The E02-013 experiment is a determination of G_E^n through the measurement of the helicity dependent cross section asymmetry from the reaction $^3\overrightarrow{\mathrm{He}}(\vec{e},e'n)pp$, i.e. quasi-elastic scattering from a transversely polarized ^{3}He target. The measurements were performed at four Q^2 points, 1.2, 1.7, 2.5, and 3.5 GeV^2.

This year the G_E^n collaboration continued the analysis of this experiment and released preliminary results for the three highest Q^2 points, presented at several conferences by a number of collaborators. Primary efforts in the analysis included the reliable extraction of quasi-elastic events, studying and improving the method of differentiating recoiling protons and neutrons, and the development of Monte Carlo simulations.

4.5.2 Experiment Overview

Experiment E02-013 measured the electric form factor of the neutron by studying spin asymmetries in quasi-elastic scattering in the reaction $^3\overrightarrow{\mathrm{He}}(\vec{e},e'n)pp$ at four values of Q^2 up to 3.5 GeV^2. The scattered electron was detected in coincidence using an open-geometry electron spectrometer, BigBite, (with a solid-angle acceptance of roughly 76 msr). The recoiling nucleon was detected in a large neutron detector which, with an active detection area of around 8 m^2 at a distance $9-12$ m, provides adequate acceptance for quasi-elastic neutrons. A diagram of the physics concept is shown in Fig. 50.

The asymmetry A_{phys} relates to G_E^n through the equation

$$A_{\mathrm{phys}} = -\frac{2\sqrt{\tau(\tau+1)}\tan(\theta/2)G_E^nG_M^n\sin\theta^\star\cos\phi^\star}{(G_E^n)^2+(G_M^n)^2(\tau+2\tau(1+\tau)\tan^2(\theta/2))} - \frac{2\tau\sqrt{1+\tau+(1+\tau)^2\tan^2(\theta/2)}\tan(\theta/2)(G_M^n)^2\cos\theta^\star}{(G_E^n)^2+(G_M^n)^2(\tau+2\tau(1+\tau)\tan^2(\theta/2))},$$

where $\tau = Q^2/4M^2$, and θ^* and ϕ^* are the polar and the azimuthal angles respectively between the polarization direction of the ^{3}He nucleus and the three-momentum transfer, $\vec{q}$. A missing momentum $p_{\rm miss}$, ($\vec{q} - \vec{p}_N$, where $\vec{p}_N$ is the momentum of the nucleon) is used for selection quasi-elastic process. The $p_{{\rm miss},\perp}$, the component of $\vec{q} - \vec{p}_N$ perpendicular to $\vec{q}$, provides suppression of final state interactions (FSI), allowing for the treatment of quasi-free neutron scattering.

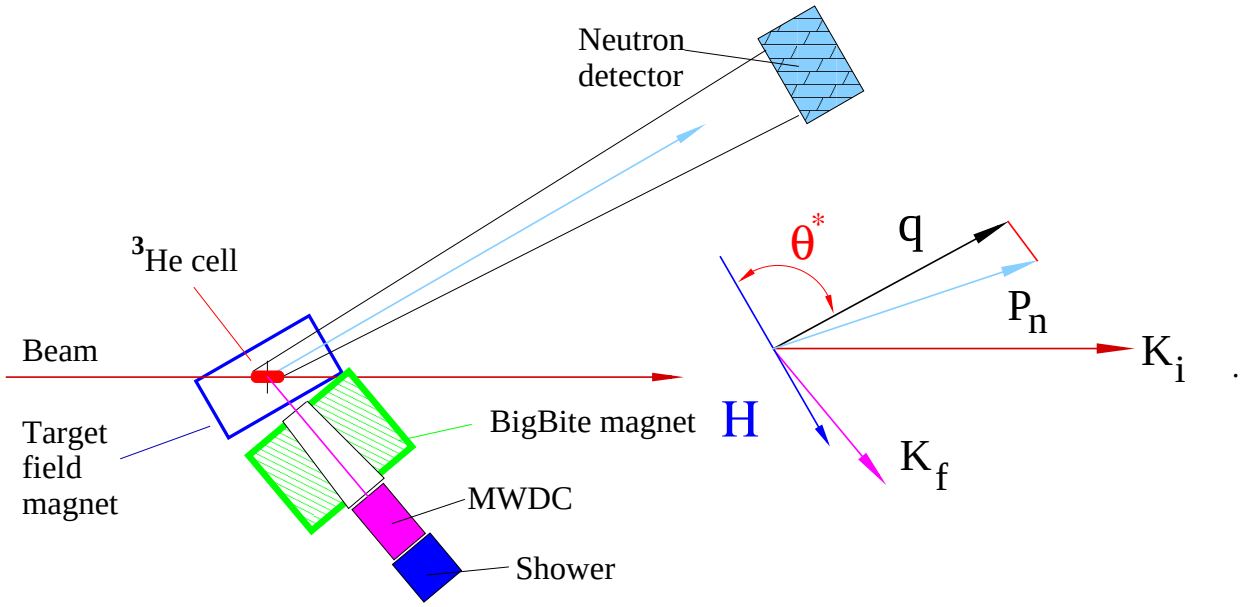

Figure 50: Conceptual layout of the E02-013 experiment. Here H shows the target holding magnetic field; K_i and K_f are the initial and a final electron momenta; $\vec{q} = \vec{K_i} - \vec{K_f}$ is the momentum transfer; P_n is the neutron momentum, θ^* is the angle between directions of the magnetic field and the momentum transfer.

Table 9 shows the kinematics for which data are taken and accumulated beam charge.

Q^2 [GeV^2]	$E_{\rm beam}$ [GeV]	Avg. θ_e [deg]	$Q_{\rm beam}$ [C]
1.2	1.519	56.26	1.2
1.7	2.079	51.59	2.2
2.5	2.640	51.59	5.5
3.5	3.291	51.59	11.4

Table 9: Four kinematics of G_E^n measurements in E02-013 and accumulated beam charge.

4.5.3 Progress of Analysis

Analysis of the G_E^n data continues from last year and we have released preliminary results for our three highest Q^2 points. Detector calibrations substantive to the analysis have been completed for these points. Most efforts in the analysis have gone to the extraction of quasi-elastic events from the data, understanding the identification of recoiling protons and neutrons, and in the development of Monte Carlo simulations.

Quasi-elastic Selection The selection of quasi-elastic events is performed by placing cuts on (pseudo-)invariant mass, components of missing momentum, and the missing mass of the reaction $e^3\text{He} \rightarrow e'nX$. This allows us to suppress final state interactions, inelastic processes such as pion electroproduction, and treat electron the interaction as with an effectively free neutron. Due to finite detector resolution there is some choice in where these cuts are placed, trading quantity of statistics for the purity of quasi-elastic sample. In practice, simulations can provide quantification background to provide corrections, but due to the present early development of these simulations, our analysis takes a conservative approach biasing towards results requiring minimal corrections. This becomes particularly important at the highest Q^2 points where pion electroproduction plays a more significant role and the momentum is not as clearly resolved in the neutron arm.

In Fig. 51 and 52 the quasi-elastic peaks can be clearly seen for two of our Q^2 points, with the selected cuts shown in red. In particular, the degraded momentum resolution at the higher Q^2 point is apparent, due to the higher nucleon momentum measured through time of flight. This degraded resolution complicates the separation of inelastic events. We have made compensations for this by placing the upper limit of the invariant mass cut at a lower value. This change in the invariant mass cut combined with the missing mass cut reduces our statistics by a factor of two without further support from simulations.

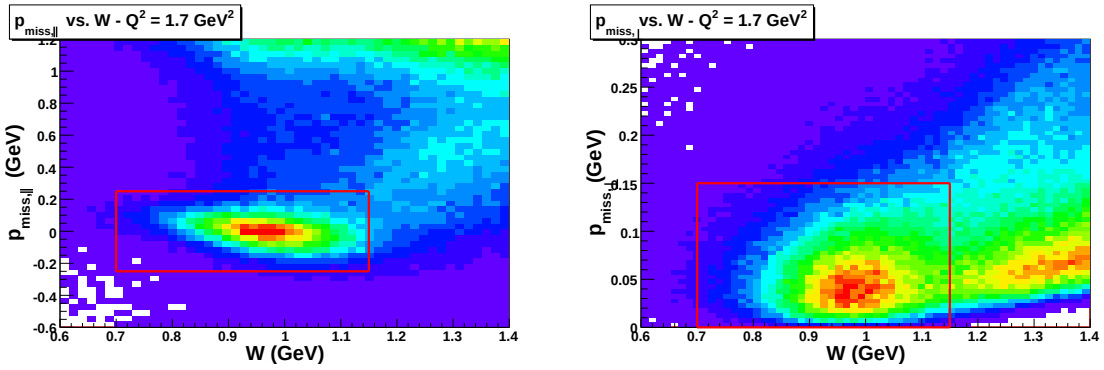

Figure 51: $p_{\text{miss},\parallel}$ and $p_{\text{miss},\perp}$ vs. invariant mass for $Q^2 = 1.7$ GeV^2. The quasi-elastic cut selection is outlined in red.

Nucleon Charge Identification For a given quasi-elastic scattering event, the detected nucleon in the neutron arm is assigned a charge based on signals in two front-most scintillator planes, known as the veto planes. Several effects may cause charge misidentification which need to be accounted for to properly calculate the neutral sample asymmetry. The dominant effects are natural detector inefficiencies in the veto planes, the interaction of the nucleon while in flight with materials such as the target cell wall and neutron arm shielding, accidental background producing a false signal in the veto planes, and charge exchange through final state interactions.

For all but the last effect, we have developed a technique that allows us to determine the relevant overall conversion probabilities directly from the data, providing knowledge of the purity of our sample. To perform this analysis, we utilize three targets with different nuclear ratios of protons and neutrons, H_2, ^{3}He, and N_2, and examine the response of the neutron arm. By looking at the ratio of the number of identified uncharged to charged nucleons for each of the three targets, it is then possible to sufficiently constrain these conversion rates using the uncharged to charged ratios without misidentification.

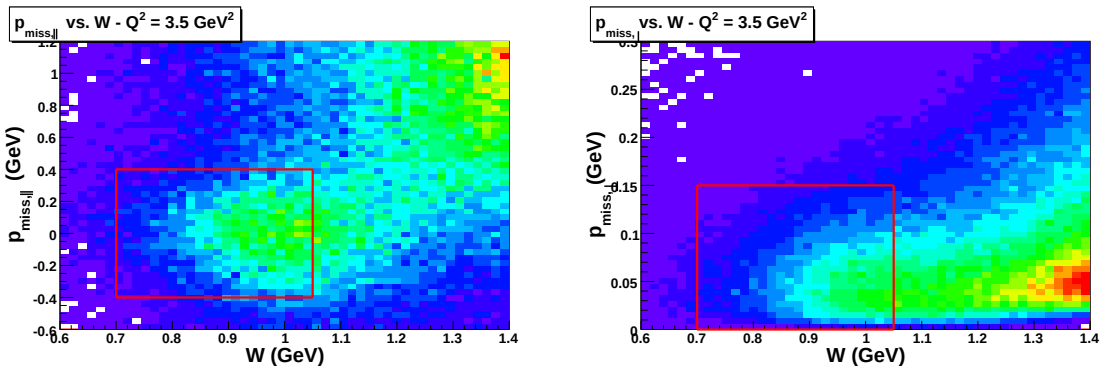

Figure 52: $p_{\mathrm{miss},\parallel}$ and $p_{\mathrm{miss},\perp}$ vs. invariant mass for $Q^2 = 3.5$ GeV^2. The quasi-elastic cut selection is outlined in red. The upper limit on the invariant mass cut has been reduced to help suppress inelastic background contributions.

Due to the differences in the initial momentum distributions of protons and neutron in ^{3}He, placing cuts on missing momentum will produce changes in the relative rates between protons and neutrons. To calculate this, we developed a simulation utilizing realistic nucleon momentum distributions bound in ^{3}He and simulate the final measured momentum distributions for quasi-elastic scattering. By placing cuts on these final momenta, the effective ratio of protons to neutrons can be determined. This analysis was determined to be unnecessary for N_2 due to isospin symmetry considerations and is irrelevant for H_2. For our analysis, the ratio of protons to neutrons for our cuts is generally near 2.15, higher than the naive expectation of 2, Fig. 53.

Monte Carlo Developments Presently work is underway to develop a Monte Carlo simulation of the experiment. From these simulations we are particularly interested in pion electroproduction process rates and asymmetries and the neutron arm response to protons and neutrons with varying momenta. From this it is our plan to increase our quasi-elastic statistics, possibly by a factor of 2, by widening our cuts and correcting using calculations of inelastic background contributions. We also hope to reduce the systematic uncertainty present in our charge identification analysis by augmenting it with results from the simulated response.

At this point we have developed a simulation which can reproduce the cross sections and asymmetries for elastic H_2 and quasi-elastic ^{3}He scattering, as well as for pion electroproduction from these targets using data from the MAID project. This simulation has provided somewhat accurate results up to invariant masses of about 1.4 GeV. Currently missing is an accurate representation of the neutron arm response, however, agreement between the data and simulation in the invariant mass spectrum and asymmetry vs. invariant mass is quite good, Fig. 54 and Fig. 55. From this we have evaluated that the inelastic contributions to the asymmetry for our present cuts are less that 1% for our highest three points.

Preliminary Results We have release preliminary results for our three highest Q^2 points ranging from $Q^2 = 1.7$ to 3.5 GeV^2, Fig. 56. These have been present at several conferences, most recently at SPIN 2008 in Charlottesville, the 2008 fall APS/DNP meeting in Oakland, and PANIC08 in Tel Aviv. For these results we have omitted the model-dependent FSI corrections, which based on preliminary calculations [5, 6], increase the G_E^n results by about 5%. The lowest Q^2 point is in agreement with the highest Q^2 point from the Madey results [7]. Our higher Q^2 points are in

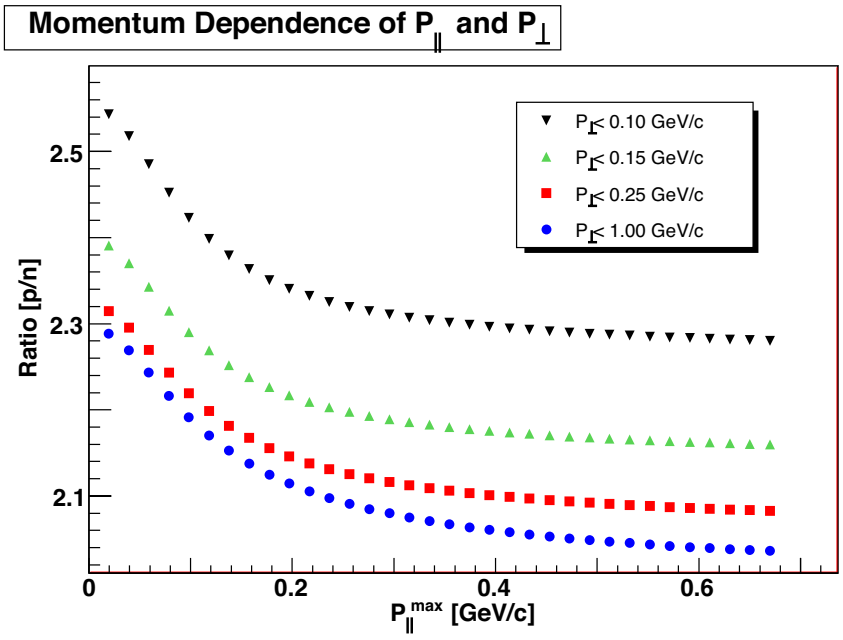

Figure 53: Effective proton to neutron ratios for a ^{3}He target with varying cuts on $p_{\mathrm{miss},\parallel}$ and $p_{\mathrm{miss},\perp}$.

disagreement with favored models, such as Miller's light front cloudy bag model [8]. Our curve is in better agreement with the Galster parameterization performed in 1971 with some of the earliest G_E^n data. Also interesting is to look at the expected perturbative QCD (pQCD) scaling behavior determined by Belitsky et al. [9], which in the case of the proton, appears to set in surprisingly early at about 2 GeV^2. Scaling a curve of the same form to our lowest Q^2 point, we do not see such behavior implying that we are not yet in the pQCD regime for this range of momentum transfer.

References

[1] M. Diehl *et al.*, *Eur. Phys. J* **C 39**:1-39, 2005.

[2] M. Guidal *et al.*, *Phys. Rev.* **D 72**:054013, 2005.

[3] G. Miller and J. Arrington, *Phys. Rev.* **C 78**:032201, 2008.

[4] C. Carlson and M. Vanderhaegen, *Phys. Rev. Lett.* **100**:032004, 2008.

[5] M. Sargsian, *Int. Jour. of Mod. Phys.* **E 10**:405, 2001.

[6] M. Sargsian, Private communication

[7] R. Madey *et al.*, *Phys. Rev. Lett.* **91**:37, 2003.

[8] G. Miller, *Phys. Rev.* **C 66**:032201, 2002.

[9] A. Belitsky, X. Ji and F. Yuan, *Phys. Rev. Lett.* **91**:092003, 2003.

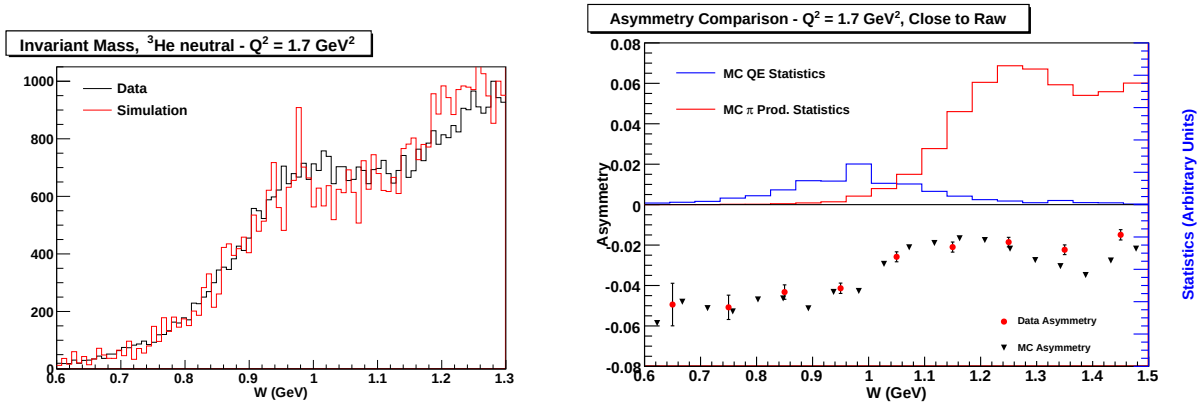

Figure 54: Agreement between data and simulation for the invariant mass spectrum and asymmetry vs. invariant mass with broad cuts for ^{3}He data at $Q^2 = 1.7$ GeV^2.

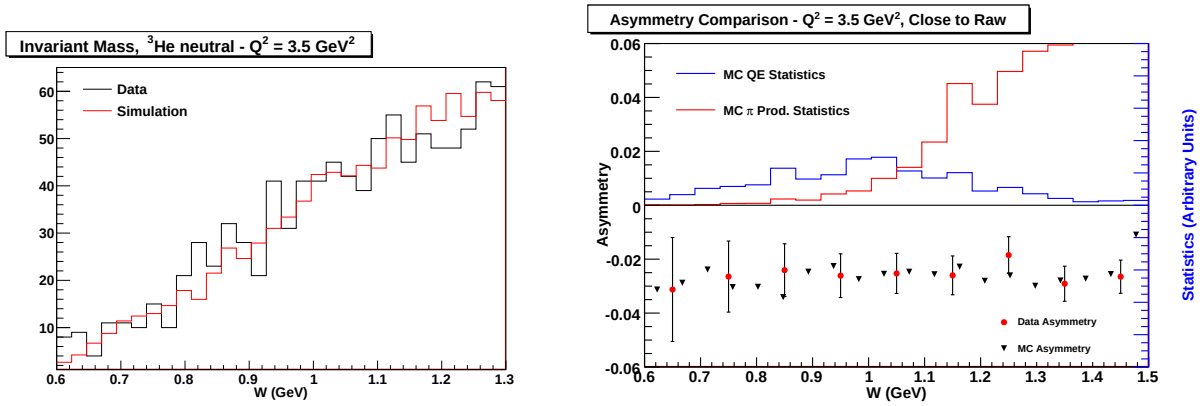

Figure 55: Agreement between data and simulation for the invariant mass spectrum and asymmetry vs. invariant-mass with broad cuts for ^{3}He data at $Q^2 = 3.5$ GeV^2.

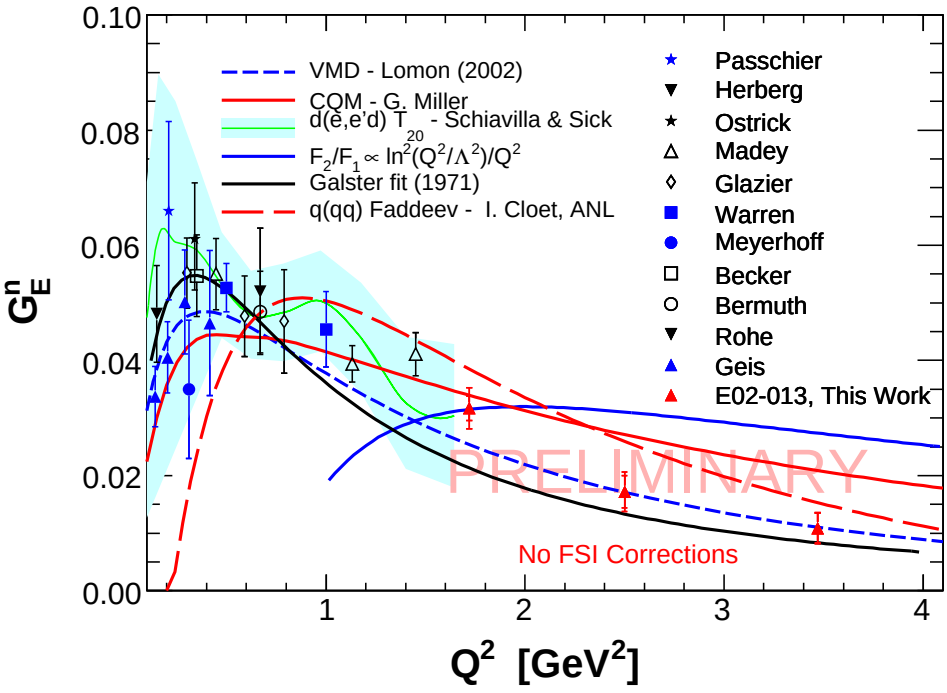

Figure 56: Preliminary results for the three highest Q^2 points for E02-013.

4.6 E03-101

The Hard Photo-disintegration of a Proton Pair in ^{3}He Nuclei

E. Piasetzky and R. Gilman, spokespersons,
and
the Hall A Collaboration.
contributed by I. Pomerantz.

Experiment E03-101, which ran during June 2007, has one Ph.D. student: I. Pomerantz from Tel Aviv University. The goal of E03-101[1] was to determine the cross section for hard two-proton disintegration of ^{3}He. The motivation rests in the extensive measurements of pn photodisintegration in the reaction $\gamma d \to pn$[2].

While modern hadronic theory provides, with some exceptions, a good explanation of measured deuteron photodisintegration at low energies [3], the underlying dynamics of photodisintegration above about 1 GeV have remained elusive. The cross-section data have led to the development of five quark-based [4, 5, 6, 7, 8] models of the reaction. Four models are based on the idea that an incoming high-energy photon is absorbed by a pair of quarks interchanged between the two nucleons; in two of these four models [6, 8] the photodisintegration cross section is directly related to measured nucleon-nucleon elastic scattering data. The fifth model, the quark-gluon string (QGS) model [5], uses Regge theory to evaluate the three-quark exchange diagram, and is based on the dominance of planar diagrams in quantum chromodynamics.

4.6.1 Simulation

In calculating the $\gamma^3\mathrm{He} \to p\,(\text{high } p_T) + p\,(\text{high } p_T) + n\,(\text{slow})$ cross section, using finite acceptance spectrometers, one encounters the following difficulty: For events in which the two photodisintegrated protons emerge at a large center of mass (CM) angle, leaving the neutron with small momentum (<100 MeV/c), the spread in phase space of the emerged protons is larger than the spectrometer acceptance. Figure 57 shows a simulated phase space density plot of the two protons for $\gamma^3\mathrm{He} \to p + p + n$ where the two spectrometers are centered around 90°CM. The left arm is simulated to have the true HRS acceptance, while the right arm is set to have infinite acceptance.
To overcome this difficulty one needs to determine the fraction of the events measured by the finite acceptance HRSs out of the total number of $\gamma^3\mathrm{He} \to p + p + n$ events. We call this ratio the "Coincidence efficiency" and denote it by f. Throughout the first year of the data analysis we constructed a MCEEP [9] based simulation to determine the value of f.

Figure 58 shows a comparison of various kinematic variables distributions from the data and simulation.

4.6.2 Preliminary results

Figure 59 shows the preliminary results of the cross-section for the 8 measured energy points at 0.8 - 4.7 GeV. The values are temporarily normalized to the available CLAS data. The analysis is approaching completion, and a draft article is expected to be submitted to the Hall A Collaboration within a few months.

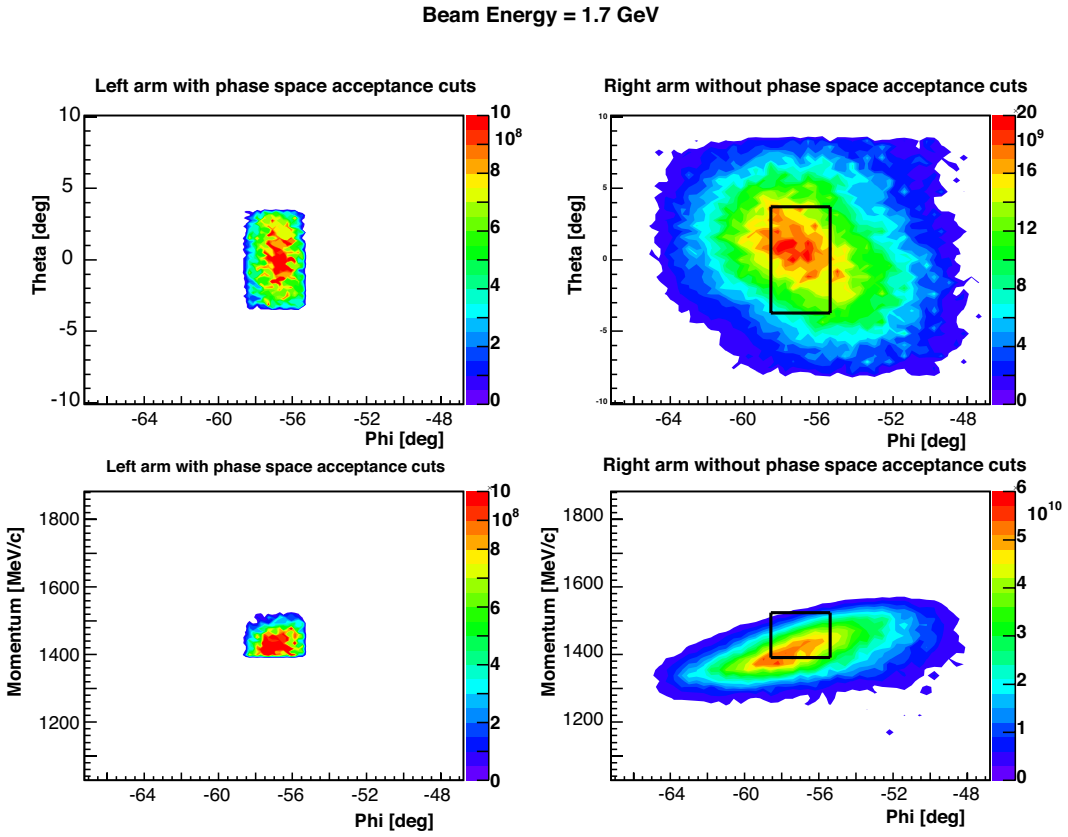

Figure 57: Phase space density plots generated with MCEEP to simulate γ^3He $\rightarrow p+p+n$ for beam energy of 1.7 GeV. The left arm is set to have the true phase space acceptance of the HRS. The right arm is set to infinite acceptance. The boxes on the right arm plots shows the true acceptance of the HRS.

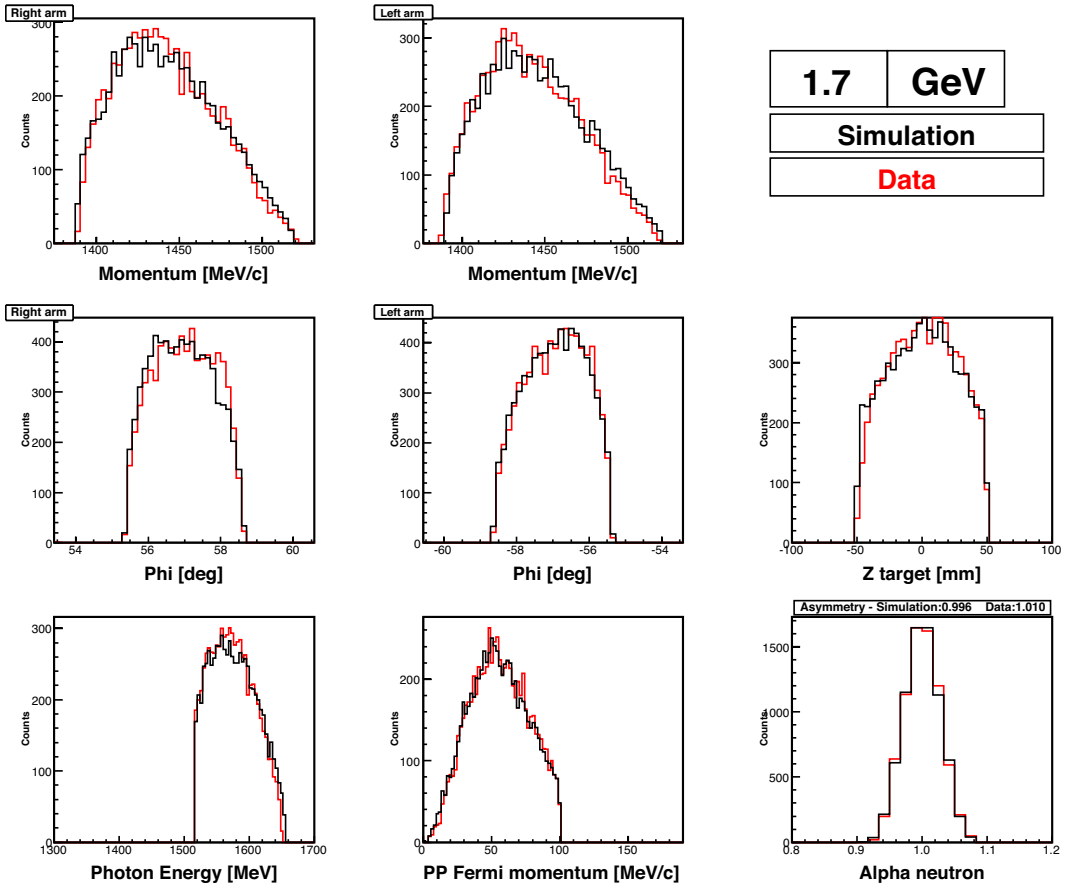

Figure 58: Comparison of various kinematic variables distributions from the data and simulation.

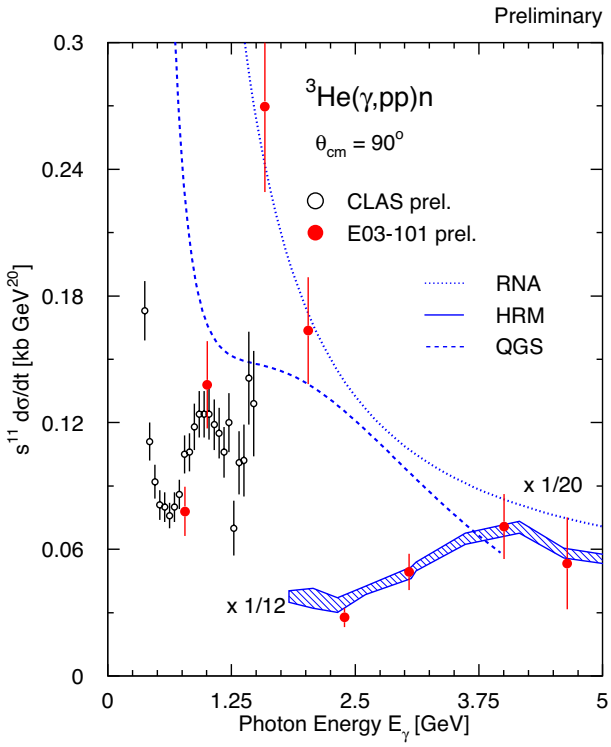

Figure 59: Preliminary results for E03-101 $\gamma^3\mathrm{He} \rightarrow p + p + n$ scaled cross section as a function of energy – the absolute normalization has been set to coincide with the preliminary CLAS data. Some of the theory curves have been renormalized by the factors indicated from the estimated normalization given in [10].

References

[1] R. Gilman, E. Piasetzky *et al.*, spokespersons, JLab experiment E03-101; and I. Pomerantz *et al.*, to be published.

[2] Recent work includes E.C. Schulte *et al.*, Phys. Rev. Lett. 87, 102302 (2001); E.C. Schulte *et al.*, Phys. Rev. C 66, 042201R (2002); M. Mirazita *et al.*, Phys. Rev. C 70, 014005 (2004); and X. Jiang *et al.*, Phys. Rev. Lett. 98, 182302 (2007).

[3] R. Gilman and F. Gross, *Electromagnetic Structure of the Deuteron*, J. Phys. G 28, R37 (2002).

[4] S.J. Brodsky and J.R. Hiller, Phys. Rev. C 28, 475 (1983).

[5] E. De Sanctis *et al.*, Few Body Syst. Suppl. 6, 229 (1992); L. A. Kondratyuk *et al.*, Phys. Rev.C 48, 2491 (1993); V.Yu Grishina *et al.*, Eur. Phys. J. A 10, 355 (2001); V.Yu Grishina *et al.*,Eur. Phys. J. A 18, 207 (2003); V.Yu Grishina *et al.*, Eur. Phys. J. A 19, 117 (2004).

[6] L.L. Frankfurt, G.A. Miller, M.M. Sargsian and M.I. Strikman, Phys. Rev. Lett. 84, 3045 (2000); L.L. Frankfurt, G.A. Miller, M.M. Sargsian and M.I. Strikman, Nucl. Phys. A 663, 349 (2000); M.M. Sargsian, Phys. Lett. B 587, 41 (2004).

[7] A. Radyushkin, private communication.

[8] B. Julia-Diaz and T.-S. H. Lee, Mod. Phys. Lett. A 18, 200 (2003).

[9] MCEEP, http://www.physics.odu.edu/ ulmer/mceep/mceep.html

[10] S.J. Brodsky *et al.*, Phys. Lett. B 578, 69 (2003).

4.7 E03-104

Probing the Limits of the Standard Model of Nuclear Physics with the ^{4}He$(\vec{e},e'\vec{p})^3$H Reaction

Contributed by Simona Malace, Mike Paolone and Steffen Strauch

Experiment E03-104, *Probing the Limits of the Standard Model of Nuclear Physics with the* $^4He(\vec{e},e'\vec{p})^3H$ *Reaction*, ran in Hall A from October 3 to November 9, 2006. Michael Paolone from the University of South Carolina, the Ph.D. student, analyzes the polarization transfer data and this analysis is now very close to completion. Simona Malace, a postdoctoral fellow with University of South Carolina, is working on the induced polarization extraction.

The goal of this experiment is to address the question whether the nucleon changes its fundamental properties while embedded in nuclear medium. This has been a long-standing question in nuclear physics, attracting experimental and theoretical attention. Nucleons are composite objects of quarks and gluons, the degrees of freedom of the Quantum Chromodynamics (QCD) Lagrangian. Yet, because of the highly non-perturbative nature of the phenomena in the confinement region, there are no available calculations for nuclei within the QCD framework. Conventionally, nuclei are effectively and well described as clusters of nucleons held together by a strong, long-range force mediated by meson exchange [1]. In the effective nuclear field theory, the interaction of an electromagnetic probe with a nucleon inside the nucleus is described by taking into account the presence of the nuclear medium. Conventional nuclear medium effects like nucleon offshellness, meson-exchange currents (MEC), isobar configurations (IC), and final-state interactions (FSI) need to be incorporated as corrections to the impulse approximation picture. In this context, the question arises whether the nucleon form factors present in the nuclear current operator could be modified as well by the presence of the nuclear medium. Over the years, a sustained theoretical activity was carried out to predict the possible change of the nucleon properties in the nuclear medium. A calculation by Lu *et al.* [2], using a quark-meson coupling (QMC) model, suggests a measurable deviation from the free-space electromagnetic form factor over the four-momentum-transfer squared Q^2 range $0.0 < Q^2 < 2.5$ GeV^2. Similar measurable effects have recently been calculated in a light-front-constituent quark model by Frank *et al.* [3], a modified Skyrme model by Yakshiev *et al.* [4], a chiral quark-soliton model by Smith and Miller [5], and the Nambu-Jona-Lasinio model of Horikawa and Bentz [6]. The connection between the modifications induced by the nuclear medium of the nucleon form factors and of the deep inelastic structure functions is discussed by Liuti [7] using the concept of generalized parton distributions (GPDs). Guzey *et al.* [8] study incoherent deeply virtual Compton scattering (DVCS) on ^{4}He in the ^{4}He$(e,e'\gamma p)X$ reaction, which probes medium-modifications of the bound nucleon GPDs and elastic form factors. However, the answer to the question whether the nucleon changes its properties while embedded in nuclear medium is only possible within a model and requires a very good handle on the more conventional reaction mechanisms mentioned above together with very precise experimental constraints.

Polarization transfer experiments of the type $(\vec{e},e'\vec{p})$ have measured polarization-transfer ratios $P_x^{'}/P_z^{'}$, which for a proton target are directly proportional to the ratio of the electric and magnetic form factors of the proton. When such measurements are performed on a nuclear target, the polarization-transfer observables are sensitive to the form-factor ratio of the proton embedded in the nuclear medium. Our recent experiment E03-104 improved the Q^2 coverage of previous measurements from Mainz microtron (MAMI) [9] and Jefferson Lab experiment E93-049 [10] of the polarization transfer and the induced polarization in ^{4}He$(\vec{e},e'\vec{p})^3$H. Our experiment added two high precision measurements at $Q^2 = 0.8$ and 1.3 GeV^2. In view of decreasing the contribution from other reaction mechanisms effects like MEC and FSI, the data were taken in quasi-elastic kinematics at low missing momentum with symmetry about the three-momentum-transfer direction. The two

Hall A high-resolution spectrometers were used to detect the scattered electron and the recoil proton in coincidence. In addition, the missing-mass technique is used to identify ^{3}H in the final state. We measure the azimuthal angular distribution of recoil protons that scatter via the spin-orbit nuclear interaction on the graphite analyzer in the focal-plane polarimeter (FPP). The recoil proton polarization observables are then extracted from the azimuthal angular distributions taking into account the spin precession of the protons in magnetic fields [11].

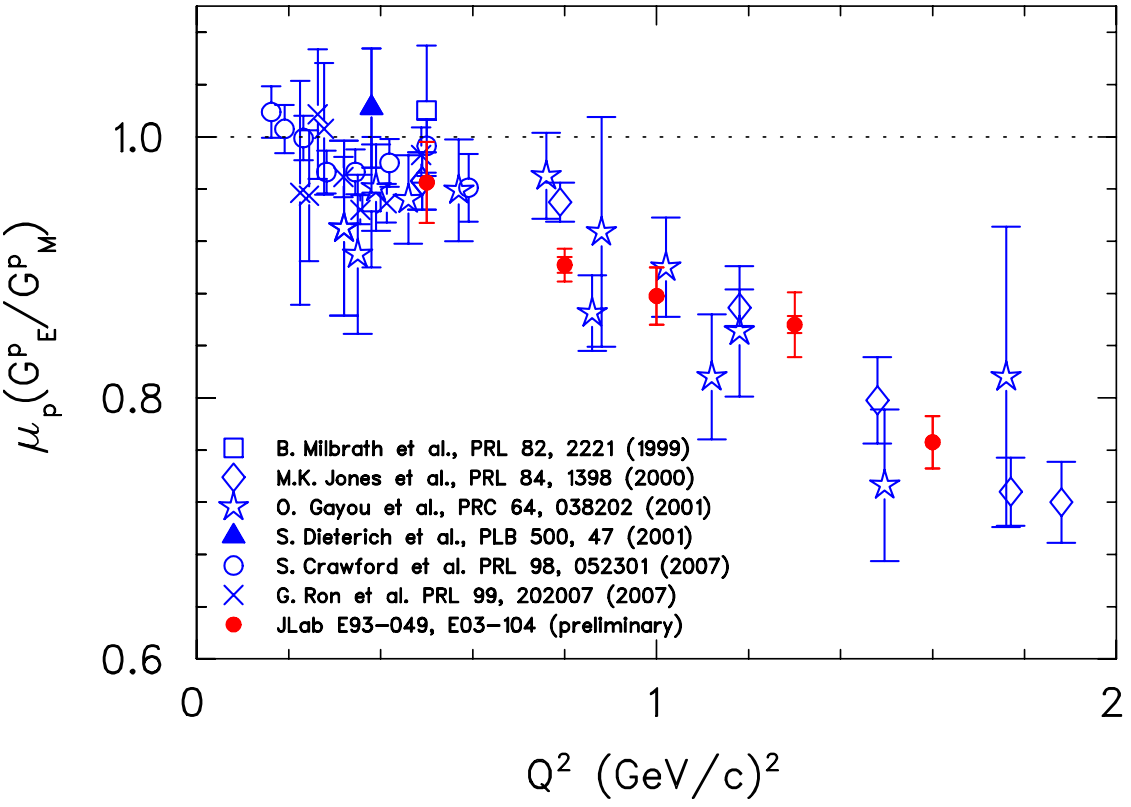

Figure 60: World data on the free proton form-factor ratio G_E/G_M from recoil-polarization experiments as a function of Q^2. The Mainz (triangle) and Jefferson Lab experiment E93-049 points along with preliminary results from experiment E03-104 are in good agreement with previous polarization-transfer data. For the preliminary data of E03-104 at $Q^2 = 0.8$ and 1.3 GeV^2, the inner error bars are statistical while the outer error bars represent the total preliminary uncertainties.

The ^{4}He target was chosen because, in spite of its relative simplicity which allows for realistic microscopic theoretical calculations, it is rather dense, increasing possible medium modifications. In addition to the ^{4}He target, a ^{1}H target was used in order to provide a base line for the comparison of in-medium to free proton polarizations. Therefore, our results on the proton polarization transfer are expressed in terms of the polarization-transfer double ratio, where the helium polarization ratio

is normalized to the hydrogen polarization ratio, measured in an identical setting:

$$R = \frac{(P'_x/P'_z)_{^4\mathrm{He}}}{(P'_x/P'_z)_{^1\mathrm{H}}}. \quad (3)$$

As a by-product of the hydrogen measurements, the free proton form-factor ratio was extracted. Figure 60 shows our preliminary data at $Q^2 = 0.8$ and 1.3 GeV^2 to be in good agreement with previous polarization-transfer measurements [11, 12].

In the polarization-transfer double ratio R nearly all systematic uncertainties cancel: the polarization-transfer observables are not sensitive to the instrumental asymmetries in the FPP, and their ratio is independent of the electron beam polarization and the graphite analyzing power. The small systematic uncertainties are due mainly to the uncertainties in the spin transport through the proton spectrometer. However, extensive studies were carried out in order to ensure not only a precise extraction of R but also of the individual polarization-transfer observables P'_x and P'_z. These studies concerned mainly the spin transport of the proton through the spectrometer and the extraction of the analyzing power of the graphite from our ^{1}H data [13]. This detailed analysis enabled us to take full advantage of the high statistics accumulated and map the missing momentum dependence of the individual polarization-transfer observables and of R with an accuracy that was not achieved before.

Figure 61 displays the comparison between our measured observables P'_x, P'_z, R and theoretical calculations at $Q^2 = 0.8$ GeV^2, left panel and $Q^2 = 1.3$ GeV^2, right panel. The Madrid fully relativistic distorted wave impulse approximation (RDWIA) [14] represented by the blue curves is a state of the art calculation which gives a fully relativistic treatment to the initial bound and final outgoing proton wave functions and to the current operator. The FSI are incorporated using relativistic optical potentials that distort the final nucleon wave function. MEC are not explicitly included in the Madrid calculation. Predictions by Meucci *et al.* [15] show that the two-body current (the seagull diagram) effects are generally small (less than 3 % close to zero missing momenta) and visible only at high missing momenta. The Madrid calculation does not describe our data. However, if instead of free form factors, density-dependent medium modified form factors as provided by the QMC model [2] are used in the RDWIA calculation (red curves), the calculation is in agreement with the data.

The same trend is observed when plotting the ratio R as a function of Q^2 as shown in Fig. 62, right panel. The Madrid RDWIA calculation (blue band) overpredicts the data by about 6%. After including the density-dependent medium-modified form factors as predicted by the QMC model [2] in the RDWIA calculation (red band), good agreement with the data is obtained.

This agreement has been interpreted as possible evidence of proton medium modifications [10]. The interpretation is based on the description of the data in a particular model in terms of medium modifications of nucleon form factors and requires excellent control of the conventional nuclear medium effects like MEC, IC, and FSI. In fact, there is an alternative interpretation of the observed suppression of R within a more traditional calculation by Schiavilla *et al.* [16] (grey band). Schiavilla's non-relativistic calculation uses free nucleon form factors and explicitly includes MEC effects which are suppressing R by almost 4%. The FSIs are treated within the optical potential framework and include both spin-dependent and spin-independent charge-exchange terms which play a crucial role in his calculation of P_y. The spin-independent charge-exchange term is constrained by $p + {}^3\mathrm{H} \rightarrow n + {}^3\mathrm{He}$ charge-exchange cross section data at lab kinetic energies of 57 MeV and 156 MeV. The spin-dependent charge-exchange term is taken to be real, with a depth parameter depending logarithmically on the lab kinetic energy, and with radius and diffuseness values of 1.2 fm and 0.15 fm, respectively. In Schiavilla's model, the final-state interaction effects suppress R by an additional 6% bringing this calculation also in good agreement with the data.

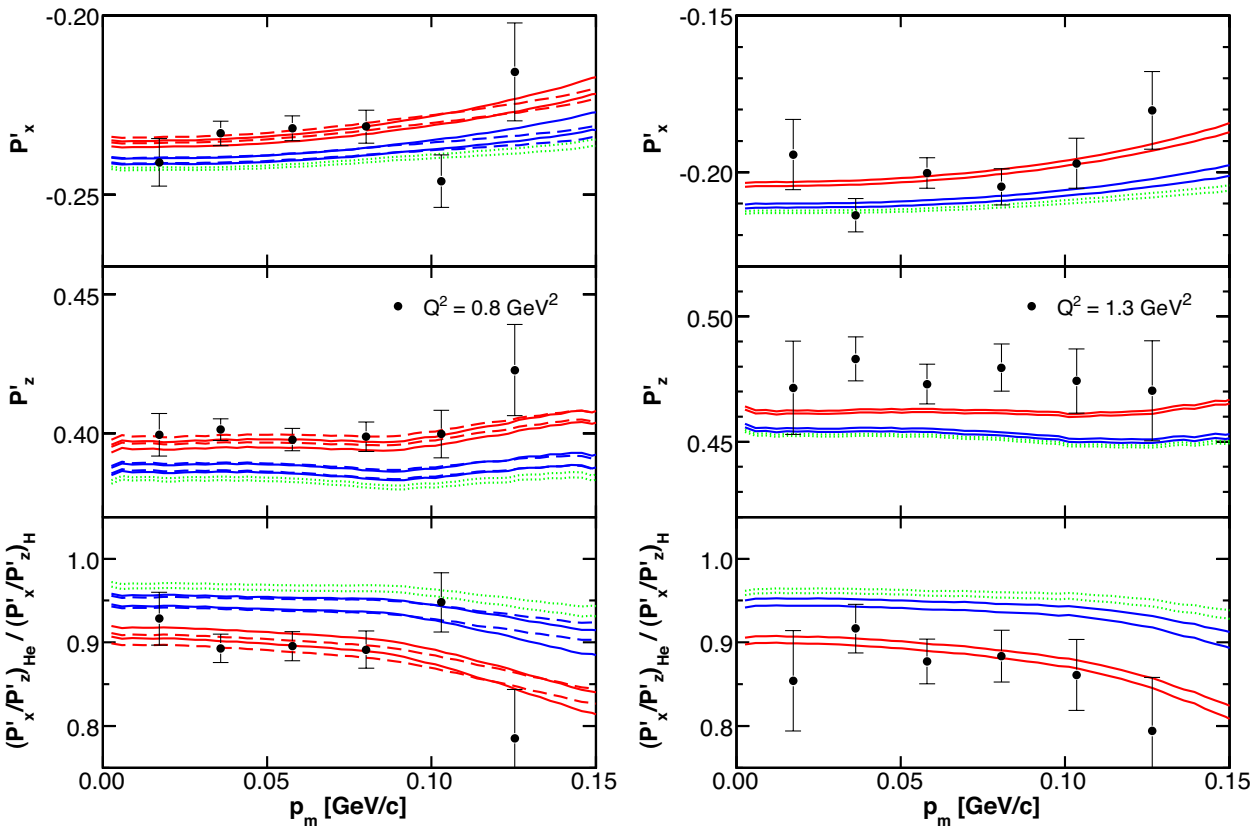

Figure 61: The polarization transfer $P_z^{'}$, $P_x^{'}$ and R extracted from our data at $Q^2 = 0.8$ GeV^2, left panel, and $Q^2 = 1.3$ GeV^2, right panel, compared to calculations from the Madrid group [14]. The blue curves represent the Madrid RDWIA calculation using free, density-independent form factors. Different blue curves correspond to different prescriptions for the optical potential and the current conservation operator. The green curves show the plane wave impulse approximation (PWIA) prediction. The red curves display the Madrid RDWIA calculation with density-dependent nuclear medium-modified form factors as predicted by the QMC model [2].

It should be stated that charge-exchange terms are not taken into account in the Madrid RDWIA calculation.

The difference in the modeling of final-state interactions is the origin of the major part of the difference between the results of the calculations by Madrid *et al.* [14] and Schiavilla *et al.* [16] for the polarization-transfer observables. Effects from final-state interactions can be studied experimentally with the induced polarization, P_y. Figure 62, right panel, shows the data for P_y. The E03-104 data, represented by the filled black circles, are still preliminary. The P_y measurements are compared with the results of the calculations from the Madrid group and Schiavilla *et al.* at missing momenta of about zero. The data have been corrected for the spectrometer acceptance to facilitate this comparison. The measurements suggest that the induced polarization (and thus the final-state interaction) is overestimated in the model of Schiavilla *et al.* Note that the charge-exchange terms, particularly, the spin-dependent one, gives the largest contribution to Schiavilla's calculation of P_y. The induced polarization proves to be sensitive to the choice of optical potential allowing this

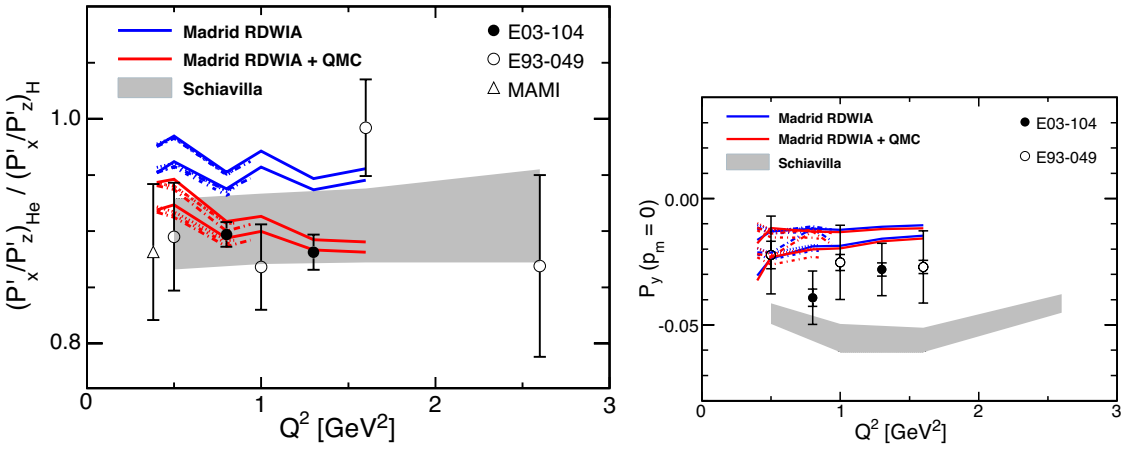

Figure 62: Recoil-polarization data as a function of Q^2 from Mainz [9] and Jefferson Lab experiment E93-049 (open symbols) [10] along with preliminary results from experiment E03-104 (filled circles), compared to calculations from the Madrid group [14] and Schiavilla *et al.* [16]. Left panel: The ratio R of transverse to longitudinal polarization of the recoiling proton in ^{4}He$(\vec{e}, e'\vec{p})^3$H compared to the same ratio for ^{1}H$(\vec{e}, e'\vec{p})$. Right panel: Induced polarization P_y for missing momentum $p_m \approx 0$; note that the experimental data have been corrected for the spectrometer acceptance.

observable to be used to constrain theoretical models of FSI. In consequence, it is of paramount importance to reduce the systematic uncertainties on the induced polarization extraction.

Typically, the P_y extraction is complicated by the presence of instrumental asymmetries. E03-104 took dedicated high-precision data to deal with this issue and our detailed analysis will make possible the precise extraction of the induced polarization. Our studies show that instrumental asymmetries could be caused by inefficient regions in the FPP chambers, possible misalignments of the front and rear FPP chambers and also by the differential absorption of the protons in the graphite analyzer. We found that for certain regions in the FPP rear chambers the tracking algorithm failed systematically to reconstruct tracks. This proved to be due to the fact that some of the chambers planes had dead wires and in those particular regions the strict requirements of the tracking algorithm regarding the number of hits needed to reconstruct a track could not be met. We relaxed the tracking algorithm by requiring less hits for a track to be reconstructed and this lead to a significant improvement of the tracking efficiency in those particular regions of the FPP chambers. This is illustrated in Fig. 63, left panel: the Fourier coefficient that we extract from our azimuthal angular distribution displayed the typical pattern of instrumental asymmetries due to highly inefficient regions in the rear chambers when the standard (old) tracking algorithm was used (black circles). If, we, however, extract the Fourier coefficient by using our relaxed tracking algorithm, the instrumental asymmetries are greatly reduced (red circles).

Figure 63, right panel, shows the Fourier coefficients extracted from the azimuthal angular distributions of E03-104 ^{1}H data. In the one photon-exchange approximation, the induced polarization and, in consequence, the corresponding Fourier coefficient is zero. Our extracted Fourier coefficients still indicate the presence of false asymmetries which are displayed in very distinct patterns: an overall offset with respect to zero, most clearly seen in the Fourier coefficient ε_y and a slope in ε_x when displayed as a function of the x coordinate. Our investigations showed that the differential absorption of the proton in the graphite analyzer could play a role but not a significant

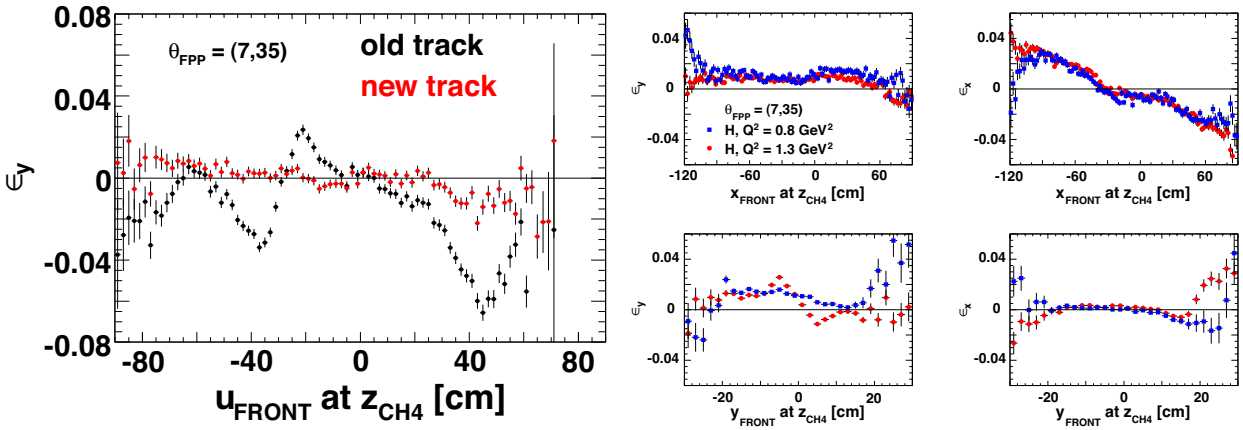

Figure 63: The Fourier coefficients extracted from our measured angular distributions. Left panel: The ε_y Fourier coefficient extracted from ^{4}He data at a Q^2 of 1.3 GeV^2 as a function of the u coordinate as reconstructed by the front FPP chambers projected to the z position of the fourth FPP chamber. The black circles display the Fourier coefficient when the standard (old) tracking algorithm was used while the red circle show the extraction when our relaxed tracking algorithm was utilized to reconstruct tracks. Right panel: The ε_x and ε_y Fourier coefficients extracted from our ^{1}H data at $Q^2 = 0.8$ GeV^2 (blue circles) and 1.3 GeV^2 (red circles) as a function of x and y coordinates as reconstructed by the front FPP chambers.

one. We are currently working to improve our alignment procedure. This detailed analysis will allow us to extract the induced polarization with high precision and constrain the interpretation of our polarization-transfer data.

References

[1] S.A. Moszkowski and B.L. Scott, Ann. Phys. (Paris) **11**, 65 (1960).

[2] D.H. Lu *et al.*, Phys. Lett. **B417**, 217 (1998) and Phys. Rev. C **60**, 068201 (1999).

[3] M.R. Frank, B.K. Jennings, and G.A. Miller, Phys. Rev. C **54**, 920 (1996).

[4] U.T. Yakhshiev, U-G. Meissner, and A. Wirzba, Eur. Phys. J. A **16**, 569 (2003).

[5] J.R. Smith and G.A. Miller, Phys. Rev. C **70**, 065205 (2004).

[6] T. Horikawa and W. Bentz, Nucl. Phys. A **762**, 102 (2005).

[7] S. Liuti, arXiv:hep-ph/0601125v2.

[8] V. Guzey, A.W. Thomas, K. Tsushima, arXiv:0806.3288 [nucl-ex, nucl-th, hep-ph].

[9] S. Dieterich *et al.*, Phys. Lett. **B500**, 47 (2001).

[10] S. Strauch *et al.*, Phys. Rev. Lett. **91**, 052301 (2003).

[11] V. Punjabi *et al.*, Phys. Rev. C **71**, 055202 (2005).

[12] M.K. Jones *et al.*, Phys. Rev. Lett. **84**, 1389 (2000); O. Gayou *et al.*, Phys. Rev. C **64**, 038202 (2001); O. Gayou *et al.*, Phys. Rev. Lett. **88**, 092301 (2002); G. Ron *et al.*, Phys. Rev. Lett **99**, 202002 (2007).

[13] Michael Paolone, Ph.D. Thesis, University of South Carolina (2008).

[14] J.M. Udias *et al.*, Phys. Rev. Lett. **83**, 5451 (1991); J.A. Caballero, T.W. Donnelly, E. Moya de Guerra and J.M. Udias, Nucl. Phys. **A632**, 323 (1998); J.M. Udias and J.R. Vignote, Phys. Rev. C **62**, 034302 (2000).

[15] A. Meucci, C. Giusti, and F.D. Pacati, Phys. Rev. C **66**, 034610 (2002).

[16] R. Schiavilla *et al.*, Phys. Rev. Lett. **94**, 072303 (2005).

4.8 E04-007

Precision Measurements of Electroproduction of π^0 near Threshold: A Test of Chiral QCD Dynamics

R. Lindgren, J. Annand, D. Higinbotham, B. Moffit, V. Nelyubin, B.E. Norum, spokespersons
and
the Hall A Collaboration.
contributed by M. Mihovilovič and others

4.8.1 Introduction

The goal of the experiment E04-007 is to make high precision cross-section measurements of the $p(e, e'p)\pi^0$ reaction near threshold.

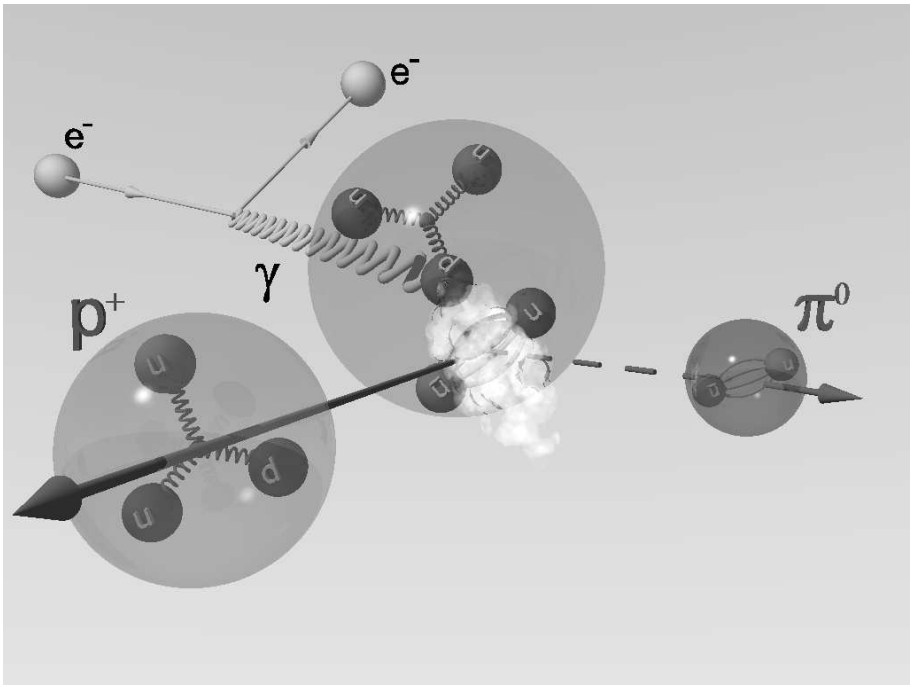

Figure 64: Cartoon of pion production.

4.8.2 Motivation

The scientific motivation for the experiment is to extend and re-examine existing measurements of electroproduction near threshold, in particular those from Mainz [1, 2], which have shown strong disagreement with the predictions of Chiral Perturbation Theory (ChPT). Since this theory is firmly grounded on the symmetries of Quantum Chromodynamics (QCD), these possible violations are very fundamental and require substantiation by more than on experiment. Measured cross-sections also disagree with phenomenological models (SAID [3], MAID [4]).

4.8.3 New BigBite Spectrometer

4.8.4 Eve - The Event Display

EVe is highly configurable event display for the BigBite spectrometer. It displays hits in scitillation planes and wire-chambers and shows all possible particle trajectories through the detector package.

4.8.5 Data Analysis

The data analysis is currently focused on the calibration of the BigBite spectrometer, which was used in this configuration for the first time in this experiment. We are presently trying to understand the optical properties of the spectrometer before analyzing real data. We expect to have first preliminary results of the measured cross-sections analysis by the end of 2008.

References

[1] Merkel, H. *et al.*, Phys. Rev. Lett. **88**, 012301 (2002).

[2] Distler, M. O. *et al.*, Phys. Rev. Lett. **80**, 2294 (1998).

[3] Arndt, Richard A. and Strakovsky, Igor I. and Workman, Ron L., Phys. Rev. C **53** 430 (1996).

[4] Drechsel, D. and Hanstein, O. and Kamalov, S. S. and Tiator, L., Nucl. Phys. **A645** 145 (1999).

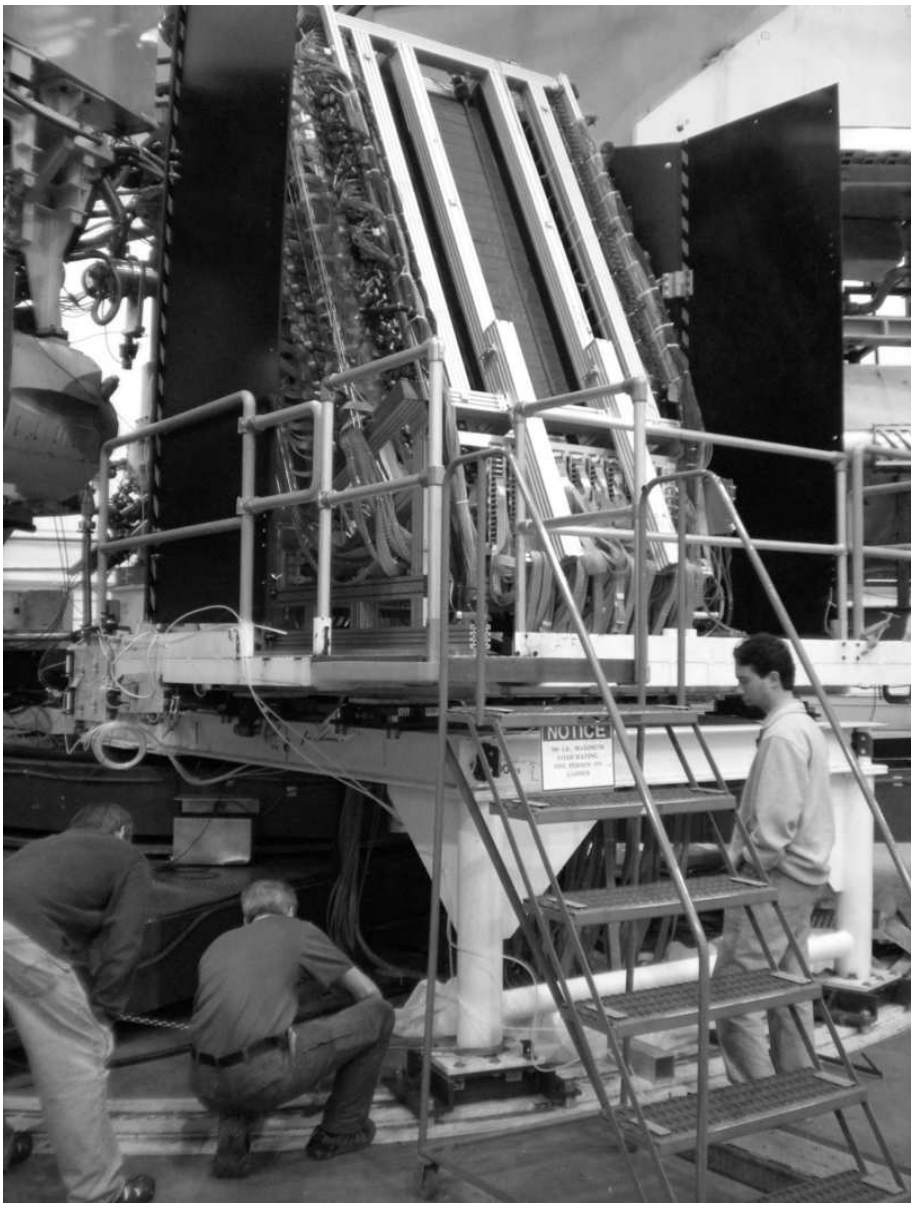

Figure 65: Photo of the BigBite spectrometer as used during E04-007.

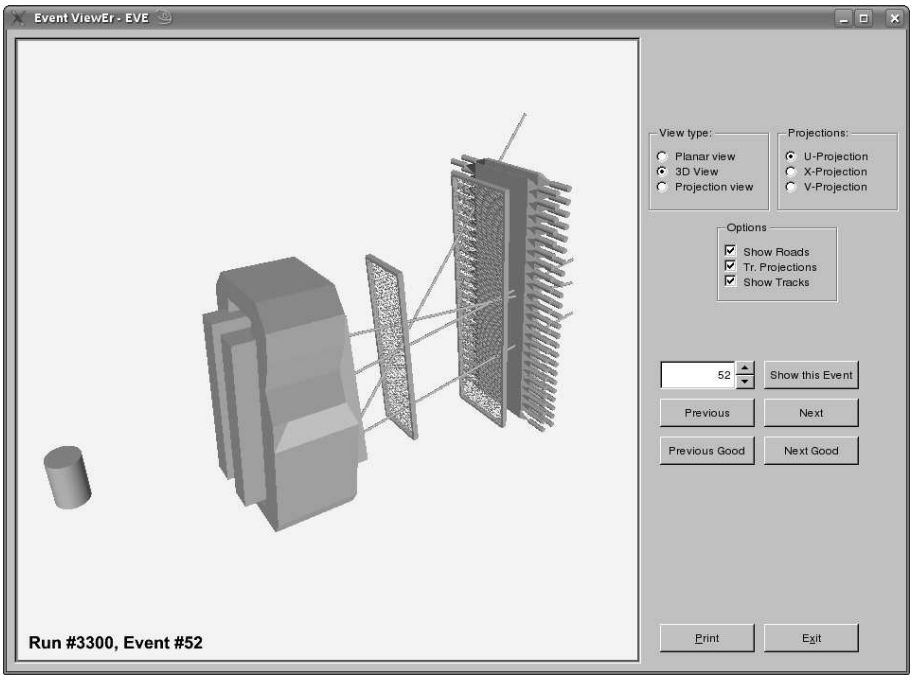

Figure 66: The Event Display (EVe).

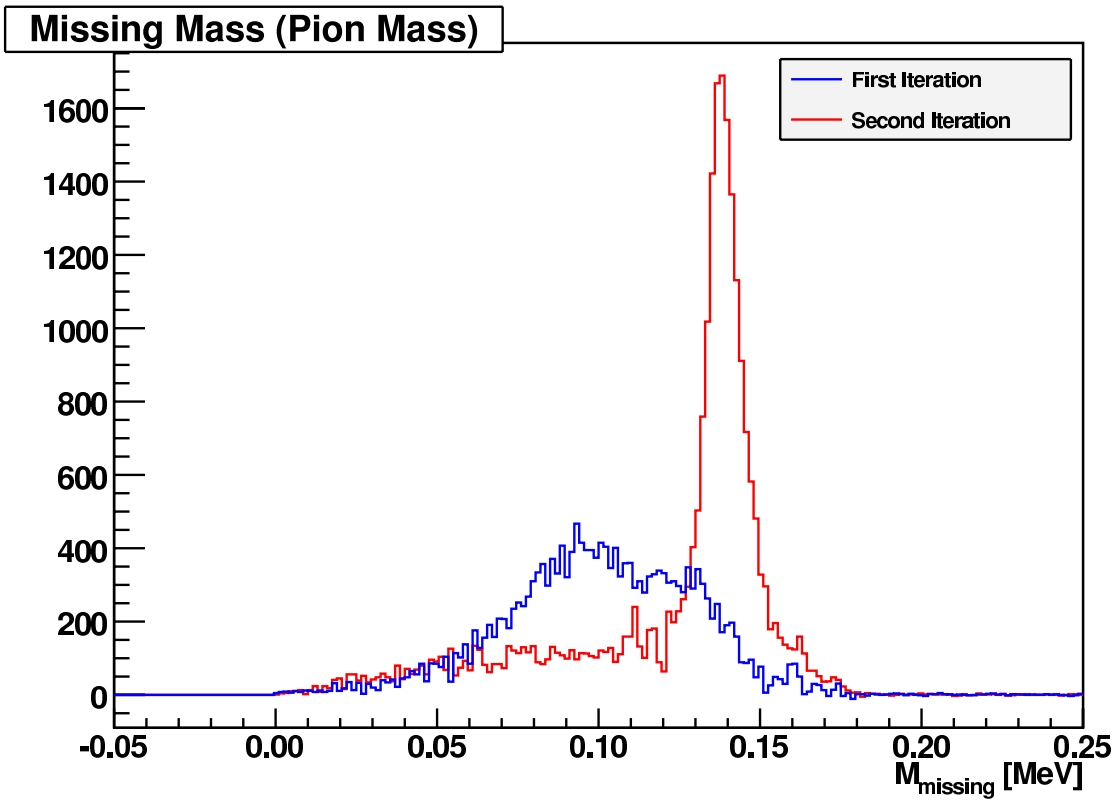

Figure 67: Missing Mass Spectrometer

4.9 E05-004

$A(Q)$ at Low Q in ed Elastic Scattering

R. Gilman, D. Higinbotham, and X. Jiang spokespersons
B.W. Lee Ph.D. student

The low energy deuteron elastic measurement ran in Hall A during July – September, 2006 with a short extension to measure elastic Li and B which ran in February 2008. The data is being analyzed by B.W. Lee of Seoul National University, Korea. The goal of the experiment [1] was to resolve a discrepancy of about 10% between two high-precision data sets, from Mainz [2] and Saclay [3], in the region $Q = \sqrt{Q^2} = 0.2$ – 0.4 GeV.

The discrepancy is interesting as the best conventional non-relativistic calculations tend to lie between the two data sets, with relativistic calculations tending to increase the prediction slightly towards the Mainz data. The best chiral perturbation theory calculations agree well with the Saclay data. It has been found that extractions of the deuteron form factors from the recent Bates tensor polarization [4] data vary by a few σ depending on whether $A(Q)$ is assumed to follow the Saclay or the Mainz data. Thus, it is important to resolve the discrepancy to determine the sign of the leading relativistic corrections at low Q, the level of convergence of chiral perturbation theory calculations, and the deuteron form factors with improved confidence.

The experimental measured elastically scattering electrons from tantalum, aluminum, carbon, hydrogen, and deuterium targets. The tantalum is used primarily for kinematics fits to determine the beam energy. The aluminum is used to subtract backgrounds in the hydrogen and deuterium data. The carbon provides a check of our ability to measure cross sections from a solid target; the carbon cross section was previously measured at NIKHEF to ∼1% [5]. Hydrogen provides a similar check of our ability to measure the cross section, with the advantage of having the same extended target geometry as the deuterium, along with a greater sensitivity to target heating. One spectrometer was used as a luminosity monitor while the other spectrometer measured the angular distribution.

To better understand the solid angle, new ∼1 and 2 msr collimators were fabricated and mounted on the front of the spectrometers. To better understand the integrated beam charge for the low currents needed for these experiments, the Hall A BCM electronics were upgraded, and a new beam calorimeter was installed in the beam line. Initial comparisons among the various BCM read-outs indicate the point-to-point variations in beam current are about 0.3%. Initial studies of the absolute current calibration using the beam calorimeter as a calorimeter, versus as a Faraday cup, indicate that the absolute current calibration is better than 1%, down to a few tenths of 1 μA.

The analysis of the data is underway. Spectra from the 687 MeV run in late September look clean, as can be seen in Figure 68, but some spectra on solid targets at 362 MeV indicate that the beam might have been striking the aluminum target frames. The final goal is to achieve 2–3% absolute cross sections and better than 1% point-to-point cross sections. A preliminary reduced hydrogen cross section is shown in Fig. 69 and shows we are still systematically low though not all corrections have yet been checked.

References

[1] R. Gilman, D. Higinbotham and X. Jiang *et al.*, JLab Experiment E05-004.

[2] G.G. Simon *et al.*, Nucl. Phys. **A 364**, 285 (1981).

[3] S. Platchkov *et al.*, Nucl. Phys. **A 510**, 740 (1990).

[4] J. Calarco, private communication.

[5] E. A. J. Offermann *et al.,* Phys. Rev. C **44** (1991) 1096.

[6] J. Arrington and I. Sick, Phys. Rev. C **76** (2007) 035205.

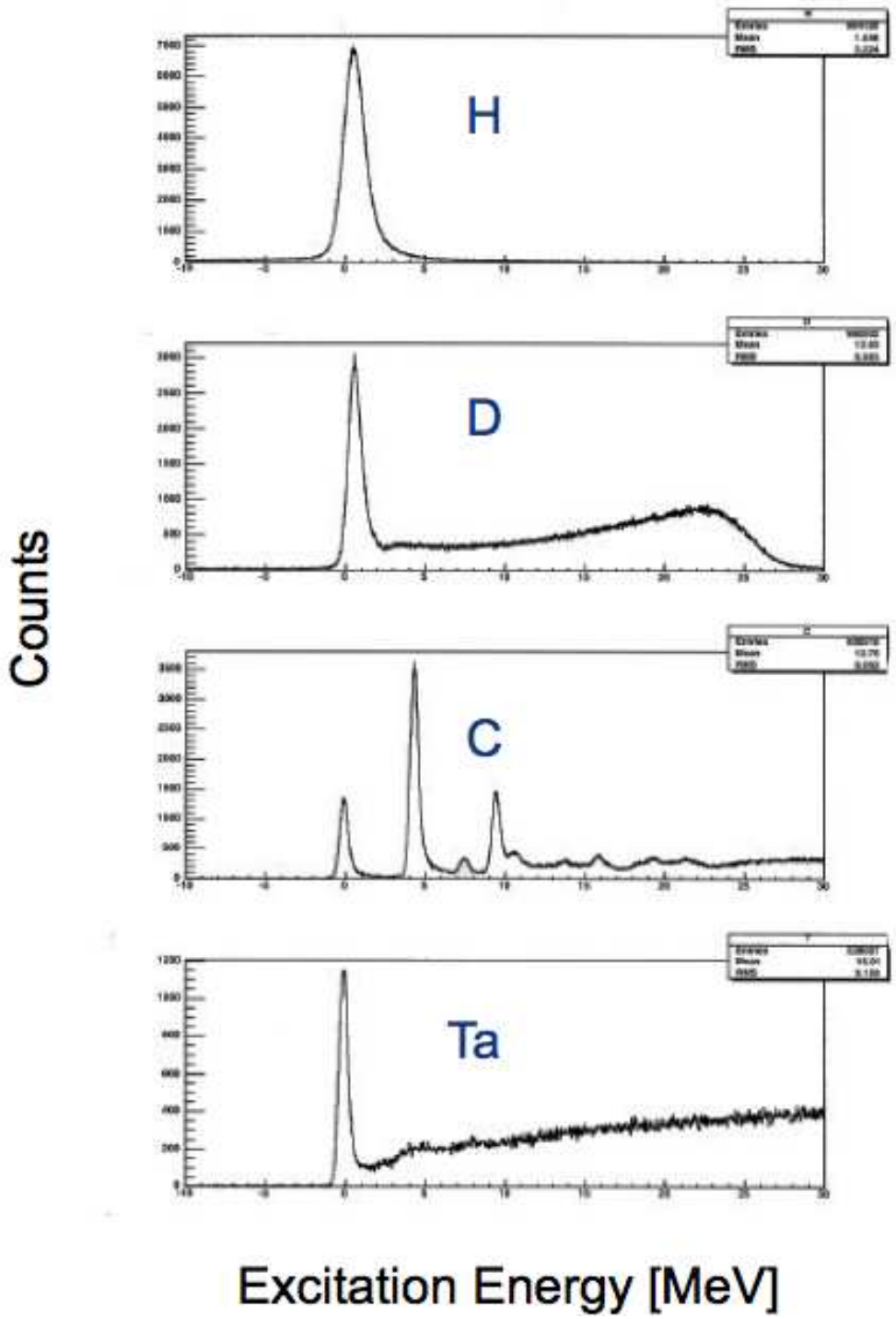

Figure 68: Shown are the excitation spectra for hydrogen, deuterium, carbon and tantalum as taken during the low energy $A(Q)$ measurement.

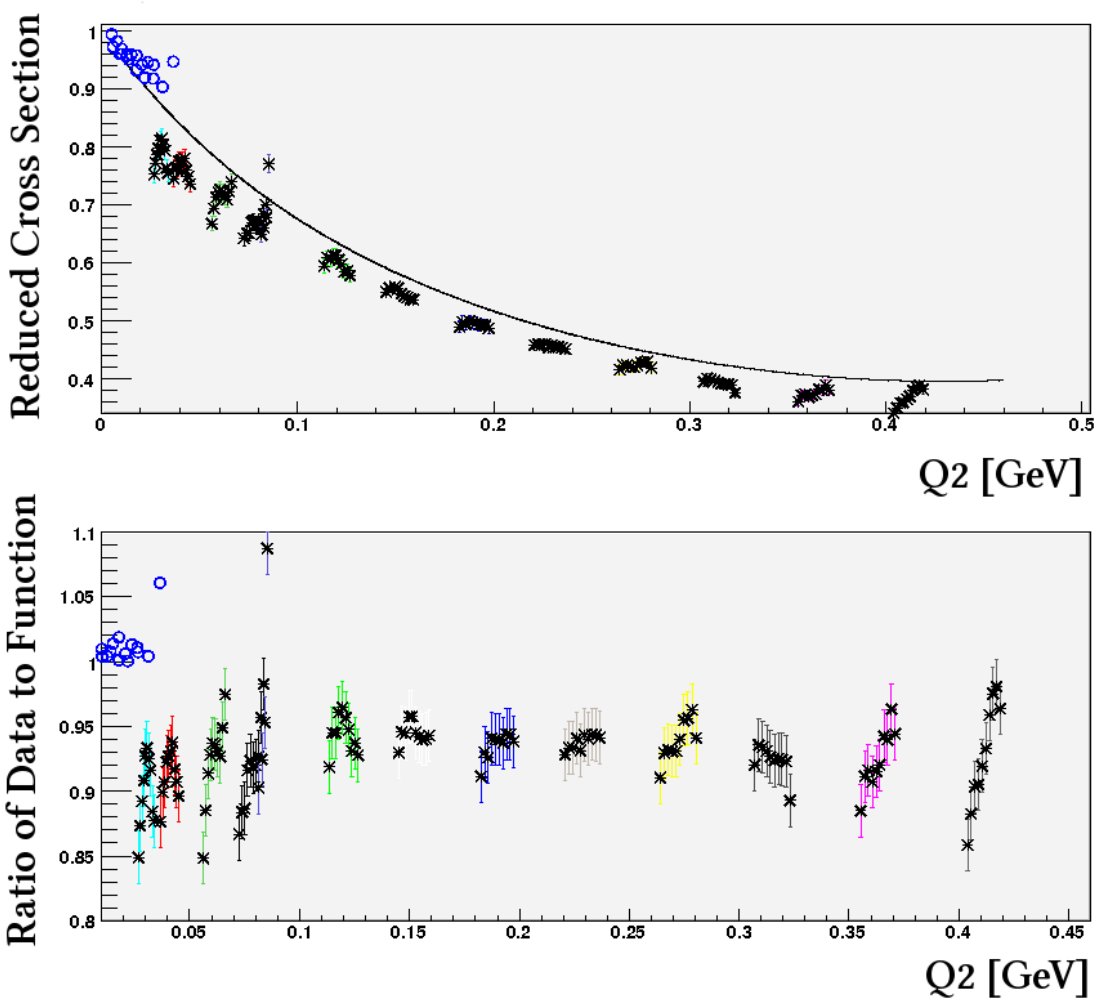

Figure 69: Shown is the reduced hydrogen cross section that is presently being obtained as compared to a world data fit from Arrington and Sick [6]. The blue circles are from Mainz data. The ratio plot clearly shows that our current preliminary data is systematically low. The analysis is being reviewed (deadtime corrections, eff., etc.) to understand what is causing the reduction.

4.10 E05-103

Low Energy Deuteron Photodisintegration

R. Gilman, A. Sarty, and S. Strauch, spokespersons,
contributed by J. Glister

Experiment E05-103, Low Energy Deuteron Photodisintegration is one of two LEDEX experiments which ran from July to September 2006. The experiment has two Ph.D. students: J. Glister (St. Mary's and Dalhousie Universities, Canada) and G. Ron (Tel Aviv University, Israel).

The goal of E05-103 [1] was to obtain recoil proton polarization observables in deuteron photodisintegration over a range of angles and energies near 300 MeV. Current hadronic interaction models are in excellent agreement with deuteron photodisintegration data up to a few hundred MeV. The models are based on meson, nucleon and Δ degrees of freedom and include meson-exchange currents, final state interactions and relativistic corrections [2]. The modern calculations include a series of technical advances over older ones, such as modeling the pion with finite velocity, non-perturbative treatment of the Δ resonance, and mutual interaction in the πNN system [3]. A striking disagreement emerges at roughly 300 MeV; where the calculations predict that the induced recoil proton polarization near $\theta_{cm} = 90^\circ$ will approach 0, yet the data grows in magnitude up to nearly -1 at 500 MeV. This large peak in the induced polarization has been known, but not explained, for 30 years.

The existing data set consisted of measurements taken at different labs, with varying bins in energy and angle. Also, no polarization transfer data had been taken below ≈500 MeV. We proposed to obtain a systematic set of recoil polarization observables, both transferred and induced, at lower energies, in order to identify precursors of what causes the disagreement at 500 MeV. The experiment covered an angular range of $\theta_{cm} = 20^\circ$ – 120°, generally in 10° steps, although some intermediate angles were skipped due to time constraints. A photon energy range of 270 – 360 MeV was covered at each angle using two spectrometer momentum settings, except at the two largest angles and one of the intermediate ones. All measurements were taken above pion production threshold, but in kinematical regimes where the proton had sufficient momentum to exclude existence of a pion in the final state.

Due to the relatively low energy, the older McNaughton analyzing power parameterization [4] was not sufficient and *ep* elastic scattering measurements [5] were taken to obtain a new parameterization [6] which provided an extension to lower energies and higher FPP scattering angles. The extension to higher scattering angles led to an improvement of up to 1.6 times in the FPP figure of merit at low energies, as shown in Figure 70.

The angular dependence of the new transferred ($P_x^{c'}$ and $P_z^{c'}$) and induced (P_y) polarization data are shown in black in Fig. 71 and 72 for photon energies of 277 MeV and 357 MeV, respectively. Previous induced polarization measurements [8]-[18] are shown in blue. The new analyzing power parameterization, spectrometer mispointing corrections, target energy loss corrections and background subtraction of electron and target wall contamination were all considered. The COSY [7] spin precession method was used to precess the protons through the magnetic field of the spectrometer. False asymmetries due to inhomogeneities in FPP efficiency and misalignments were parameterized across the focal plane and subtracted away. The error bars are statistical only. Systematic uncertainties due to spin transport, beam energy, beam polarization, reconstruction of FPP scattering angles, momentum, normalization factors and uncertainties in analyzing power and false asymmetry parameterizations are shown as black error bands. The calculations are from [2] (solid line) along with recent, unpublished improvements from [3] (dashed line). The energy dependence of the new induced polarization data is also shown in black in Figure 73 for a center of mass angle

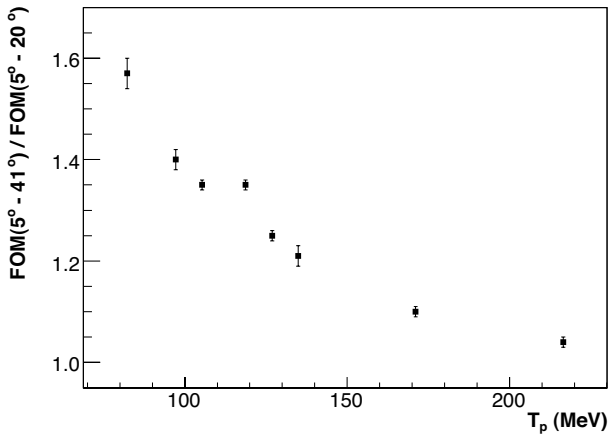

Figure 70: Figure of merit ratio for two θ_{fpp} ranges ($FOM(5^\circ - 41^\circ)/FOM(5^\circ - 20^\circ)$) as a function of proton energy at carbon center (T_p). Uncertainties are statistical only.

of 90°, along with previous measurements [8, 10, 19] and theoretical calculations from Schwamb and Arenhövel and Kang *et al.* [20].

The transferred polarizations, or $P_x^{c'}$ and $P_z^{c'}$, are in rough agreement with the calculation of Schwamb & Arenhövel, with exception to $P_x^{c'}$, having a good agreement with the older calculation (solid line) at the highest energy. The induced polarization results are in good agreement with the calculation within uncertainties at the lowest energy, while at the highest energy the new data, while statistically consistent with the older data, show a slightly greater deviation from theory than the current world data. Since P_x^c and P_y arise from the real and imaginary parts of the same combination of amplitudes, it is interesting that the imaginary part appears to be better predicted at the lower beam energy, below the Δ resonance, while the real part appears to be better predicted at the higher energy. The differences between P_z^c calculations and data are similar at all energies; P_z^c arises from a combination of the squared magnitudes of the contributing amplitudes. In the hadronic framework, the increasingly poor agreement as the energy is raised might result from tails of higher-lying resonances, relativistic corrections, or inadequate modeling of the increasingly inelastic NN interaction. More exotic explanations, such as a need for quark and gluon degrees of freedom, cannot be ruled out.

This work has already resulted in one publication on the proton form factors [5]. A paper on the polarimeter calibration [6] is expected to be submitted in late 2008. A paper on the photodisintegration results [21] discussed here is expected to be submitted in early 2009.

References

[1] Jefferson Lab Hall A Collaboration proposal E05-103; spokespeople: R. Gilman, A. Sarty, S. Strauch (2005); J. Glister *et al.*, in preparation.

[2] M. Schwamb and H. Arenhvövel, Mod. Phys. Lett. **A 18**, 190 (2003); M. Schwamb and H. Arenhvövel, Nucl. Phys. **A 696**, 556 (2001); and M. Schwamb and H. Arenhvövel, Nucl. Phys. **A 690**, 682 (2001).

[3] M. Schwamb, Habilitation thesis, Johannes Gutenberg-Universität Mainz, 2006.

[4] M. McNaughton *et al.*, Nucl. Inst. Meth. in Phys. Res. **A 241**, 435 (1985).

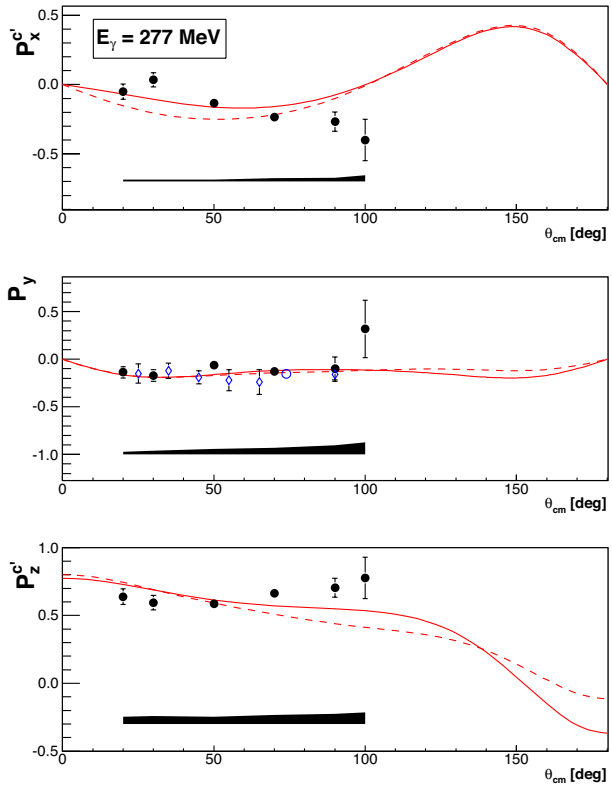

Figure 71: Angular distributions for recoil proton polarizations in deuteron photodisintegration, for $E_\gamma = 280 \pm 10$ MeV. See text for details.

[5] G. Ron, J. Glister, B. Lee *et al.*, Phys. Rev. Lett. 99 (2007) 202002.

[6] J. Glister, G. Ron, B. Lee *et al.*, to be submitted to Nucl. Instr. and Meth. A.

[7] M. Berz, H.C. Hoffmann, H. Wollnik, Nucl. Instr. and Meth. **A 258**, 402 (1987).

[8] F. F. Liu *et al.*, Phys. Rev. **165**, 1478 (1968).

[9] R. Kose *et al.*, Z. Phys. **220**, 305 (1969).

[10] T. Kamae *et al.*, Phys. Rev. Lett. **38**, 468 (1977).

[11] A.S. Bratashevskii, Yad. Fiz. **31**, 860 (1980); and A.S. Bratashevskii, Sov. J. Nucl. Phys. **31**, 444 (1980).

[12] A.S. Bratashevskii, Yad. Fiz. **32**, 418 (1980); A.S. Bratashevskii, Sov. J. Nucl. Phys. **32**, 216 (1980); A.S. Bratashevskii *et al.*, Pis'ma Zh. Eksp. Teor. Fiz. **31**, 295 (1980); and A.S. Bratashevskii *et al.*, JETP Lett. **31**, 270 (1980).

[13] A.S. Bratashevskii *et al.*, Yad. Fiz. **43**, 785 (1986); and A.S. Bratashevskii *et al.*, Sov. J. Nucl. Phys. **43**, 499 (1986).

[14] A.S. Bratashevskii *et al.*, Yad. Fiz. **44**, 960 (1986); and A.S. Bratashevskii *et al.*, Sov. J. Nucl. Phys. **44** (1986).

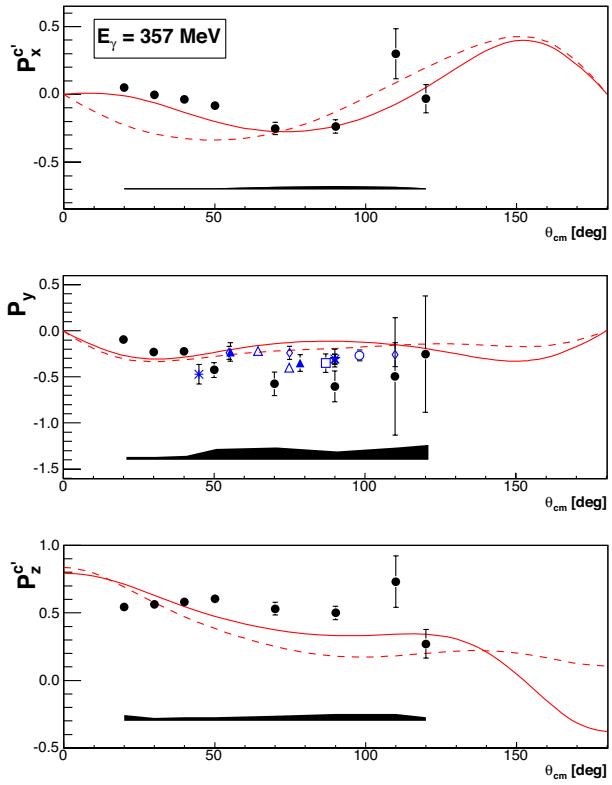

Figure 72: Angular distributions for recoil proton polarizations in deuteron photodisintegration, for $E_\gamma = 360 \pm 10$ MeV. See text for details.

[15] V.P. Barannik *et al.*, NPA451, 751 (1986).

[16] R.O. Avakyan *et al.*, Journal YF **52**, 312 (1990); Journal SJNP **52**, 198 (1990).

[17] A. A. Zybalov *et al.*, Nucl. Phys. **A 533**, 642 (1991).

[18] V.B. Ganenko *et al.*, Z. Phys. **A 341**, 205 (1992).

[19] K. Wijesooriya K *et al.*, Phys. Rev. Lett. **86**, 2975 (2001).

[20] Y. Kang, P. Erbs, W. Pfeil, and H. Rollnik, *Abstracts of the Particle and Nuclear Intersections Conference*, (MIT, Cambridge, MA) (1990); and Y. Kang, Ph.D. thesis, Bonn (1993).

[21] J. Glister, G. Ron, B. Lee *et al.*, to be submitted to Phys. Rev. Lett..

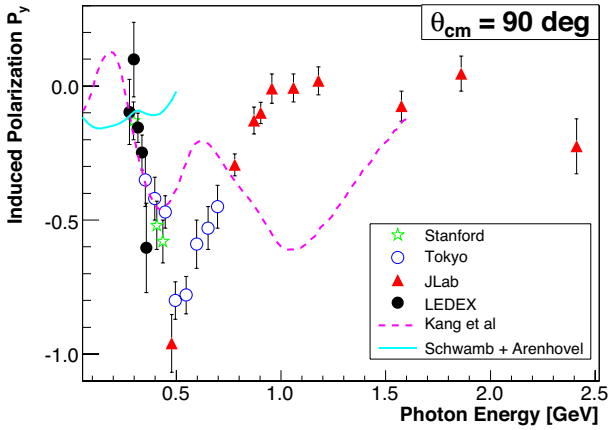

Figure 73: Energy distribution for induced recoil proton polarization in deuteron photodisintegration, for $\theta_{cm} = 90°$. See text for details.

4.11 E05-110

Coulomb Sum Rule experiment and data analysis progress

S. Choi,J.-P.Chen, and Z.-E. Meziani, spokespersons,
and
the Hall A Collaboration.
contributed by H. Yao.

4.11.1 The Coulomb Sum Rule experiment summary

In this experiment the longitudinal and transverse response functions will be extracted from a precision measurement of inclusive electron scattering cross sections in the quasi-elastic region for ^{4}He, ^{12}C, ^{56}Fe and ^{208}Pb with four different angles (15°, 60°, 90°, 120°). This experiment was completed at the beginning of 2008 with data taking over a period of two and a half months. We used incident electron beam energies from 0.4 GeV to 4 GeV, spectrometers momenta from 0.1 GeV/c to 4 GeV/c. Besides using the standard HRS detector packages, the NaI(Tl) detector was added to the HRS-L, to reduce the systematic error generated by low-energy electron background. In order to obtain the final cross sections, careful offline analysis is required. So far, we have completed the following analysis items:

- NaI detector calibration (X.Yan)
- Density fluctuation of liquid and gas targets (Y.Oh)
- Carbon form factor extracted using elastic cross sections (Y.Oh)
- Data check for production runs (Y.Oh)
- Beam energy calibration (J.Song)
- Spectrometer optics for all energies (H.Yao)
- BPM calibration (V.Sulkosky, H.Yao)

4.11.2 NaI Calibration

The NaI newly refurbished detector was configured in three individual boxes, each holding 90 crystals in order to fit in the left spectrometer detector package, The resolution obtained is essential for an extensive study of the low-energy background of the Coulomb Sum Rule experiment.

By minimizing the difference between an event's momentum and its energy deposited in a cluster of NaI blocks we determined the coefficients for each NaI crystal. However, for some areas, some crystal blocks did not operate properly, so we devised a method for recover the missing energies of bad blocks from the neighboring good blocks. After calibration, the NaI detector reached a resolution four times better than the pion rejector.

The figure on the left side in fig. 74 shows the amplitude of the middle box of NaI detector of run 4082 before calibration of the carbon target at 23° with 739 MeV incident electron beam energy. After calibration, the ratio of deposited energy in in the middle box to scattering electron energy is shown on the right side. Same for fig. 75, but with lead target at 120° .

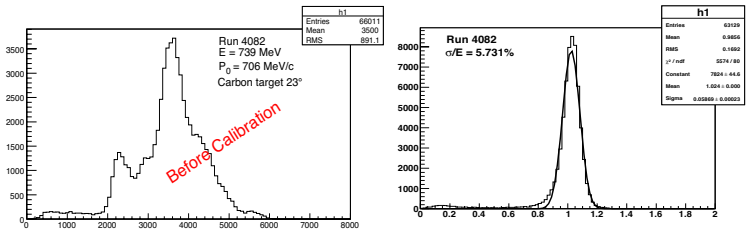

Figure 74: NaI calibration for Run 4082.

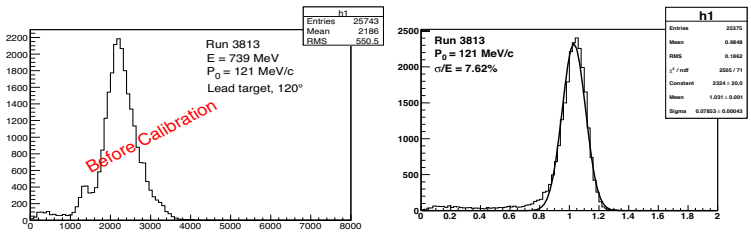

Figure 75: NaI calibration for Run 3813.

4.11.3 Density fluctuation

In the case of liquid and gas targets, the beam current heats the targets and vaporizes it along its path, which result in a reduction of the target density. This relation can be approximated as a linear relation between the beam current and the density of the target.

$$\rho(I) = \rho_0(1 - BI)$$

Here, I is the magnitude of beam current, B is the coefficient of density fluctuation. In order to measure B, runs were taken with the same kinematics but various beam current intensity. B is the slope in Figs. 76, 77.

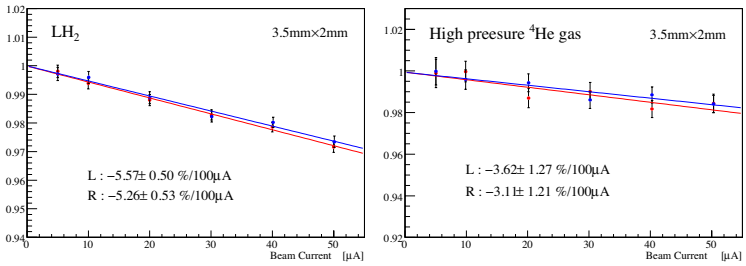

Figure 76: LH_2 and ^{4}He density fluctuation with 3.5x2 raster beam.

It is clear that the density fluctuation for the two arms has a raster size dependence. For a large raster size, the effect of the density fluctuation is smaller than the one for a smaller raster size. For left and right arms, the difference of the coefficients is negligible for 3.5x2 raster size in Fig. 76. However, it is quite large for large beam current for 2x2 raster size in Fig. 77. In principle, it is impossible since the same target is used for both arms. We are still trying to understand the

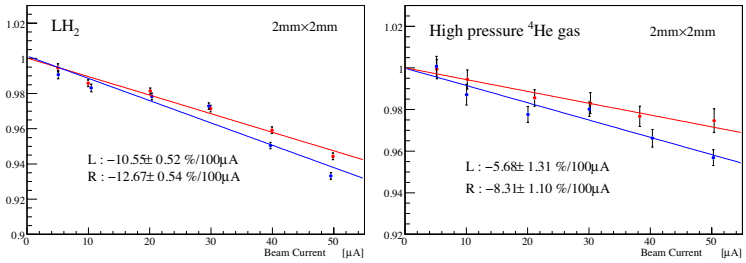

Figure 77: LH_2 and ^4He density fluctuation with 2x2 raster beam.

discrepancy at the smaller raster size but fortunately, our operating conditions are with the large raster size, so this effect is small for the cross section calculation.

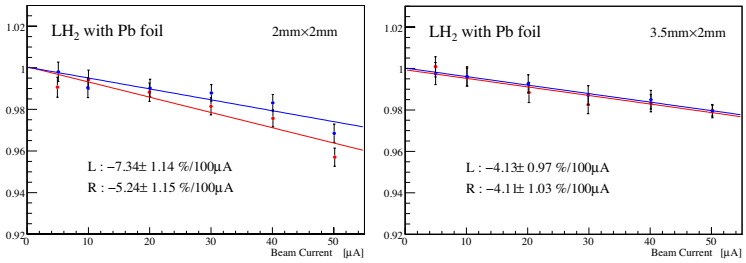

Figure 78: LH_2 boiling effect in Pb target.

The Pb target consists of a lead foil in the center of a 15 cm cell with liquid hydrogen flowing around it to keep the beam from overheating the foil and damaging it. The existence of the lead foil makes the flow of liquid hydrogen different from the one of pure liquid hydrogen, so the density fluctuation for the liquid hydrogen in Pb target can be different. It is shown in Fig. 78.

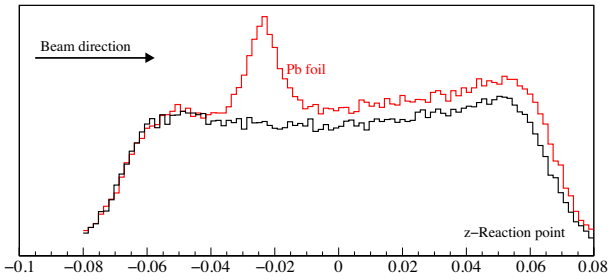

Figure 79: Comparison of reaction point-Z of liquid hydrogen with(red) and without(black) Pb foil.

Because of the Pb target setup, subtraction of the hydrogen contribution is required. However, mere correction by the density fluctuation factor isn't enough. Electron beam passing through the lead foil loses its energy due to radiative effects and consequently the cross section of hydrogen after the lead foil is different from the one of hydrogen before the foil, which can be seen in Fig. 79.

4.11.4 Carbon form factor for elastic cross section

To quickly check the data quality, we used a simulation as a tool to calculate the Carbon form factor extracted from the world data and compared it with our own data. The data points are measured from the events with appropriate angular acceptance, Cherenkov cut and the elastic peak cut with the appropriate electromagnetic radiative corrections. From Fig. 80 which is in log scale, the data agrees with the simulation reasonably well. However, more corrections like energy calibration, angular calibration, tracking efficiency, etc..., are needed to be consider to obtain more precise result.

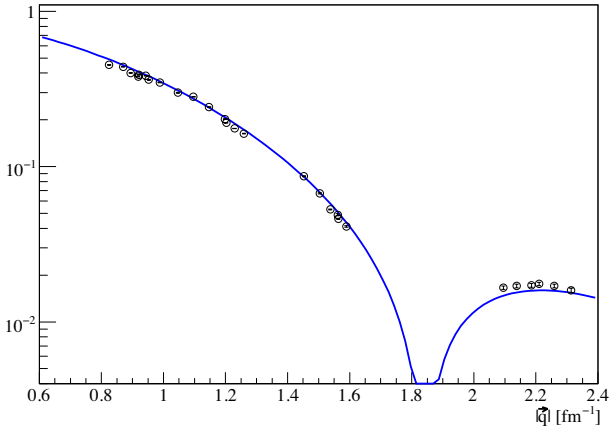

Figure 80: ^{12}C Form factor vs $|\vec{q}|$.

4.11.5 Data check for production runs

Figure 81 shows the differential cross section from some production runs. Up to now, the results for left HRS (red points) have only the Cherenkov and one track cuts, while the ones for the right HRS (black points) have the Cherenkov, one track and shower-preshower cuts.

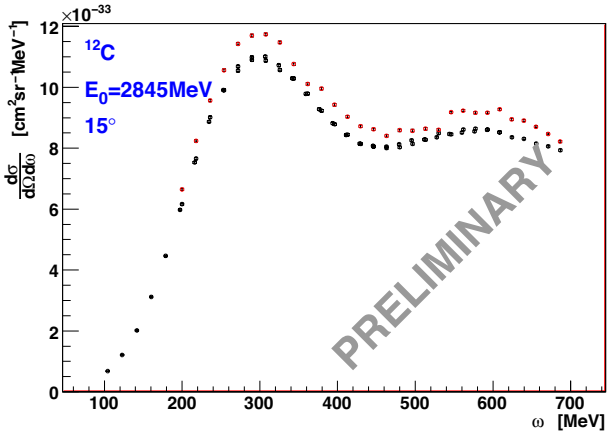

Figure 81: Data Check for carbon.

4.11.6 Beam energy Calibration at 400 MeV

At low energy, the NMR probe in the HRS dipole is outside its operation reach, so it is replaced by a Hall probe. However, as we know, the value reading from Hall probe is not calibrated well. After comparing the scattered electron energy calculated from beam energy (E_f) with the one detected from VDCs (p_f) tracking, we obtained a new calibration constant for hall probe at low energy.

$$E_f = \frac{(E_{beam} - eloss1)}{1 + \frac{(E_{beam} - eloss1)\cdot(1 - cos\Theta_{scat})}{M}} - eloss2 \tag{4}$$

here E_{beam} is Tiefenbach energy reading from epics, Θ_{scat} is the scattering angle, M is the mass of target, $eloss1$ and $eloss2$ are energy loss before and after scattering, respectively.

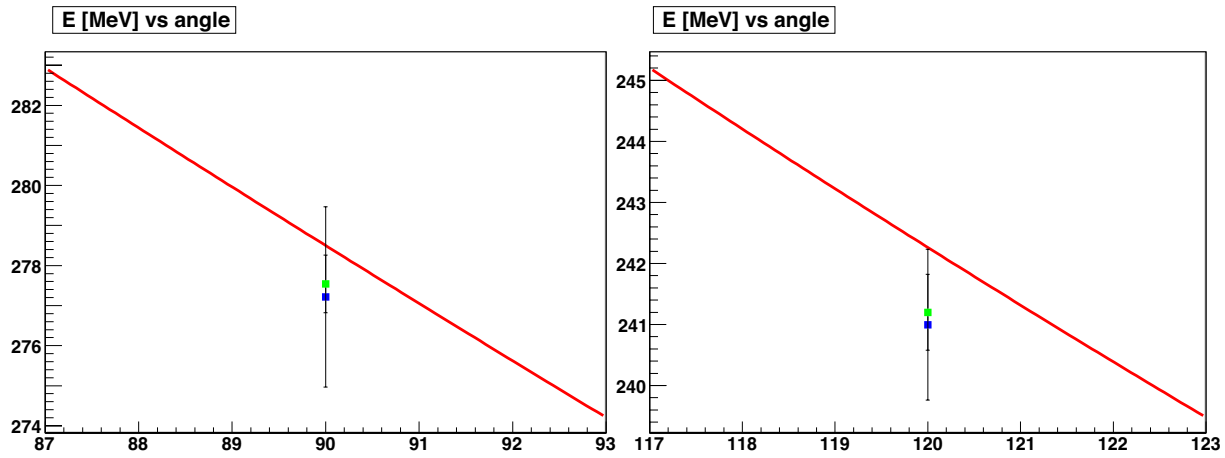

Figure 82: ^{1}H elastic scattering at 400 MeV, E_f is represented by red line while points are p_f.

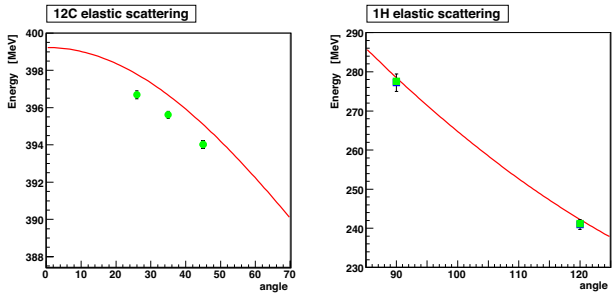

Figure 83: ^{12}C elastic scattering at 400 MeV, E_f is represented by red line while points are p_f.

From the fig. 82, we find there is about 1 MeV offset between E_f and p_f, and the ratio of E_f to p_f is,

$$\frac{E_f}{p_f} = 1.003931 \tag{5}$$

So for 400 MeV, we may multiply detected electron energy with this ratio to get correct scattered electron energy. As for fig. 83, the ratio is 1.002734.

4.11.7 Optics

The purpose of the optics studies is to reconstruct target variables from focal plane variables detected by the VDCs. By minimizing the difference between expected value of target variables like θ_{tg}, ϕ_{tg}, y_{tg} and dp with the data detected from the tracking using the VDCs, we get an optimized set of optics coefficients. While expected values are calculated from survey information, the data is reconstructed from focal plane variables at VDCs by a starting set of optics coefficients. Next three figures show the optimization result for 739 MeV. For low energy smaller than 400 MeV, we find mid-plane symmetry breaking for ϕ_{tg} and y_{tg}, which causes a misalignment of these reconstructed variables for different holes in the sieve slit, so it is necessary to add more terms and thus coefficients to compensate the effect.
For figs. 84, 85, and 86, the reconstructed variables before optimization are at on the left side in each figure, the ones after optimization are at the right side. The red lines represent the expected values.

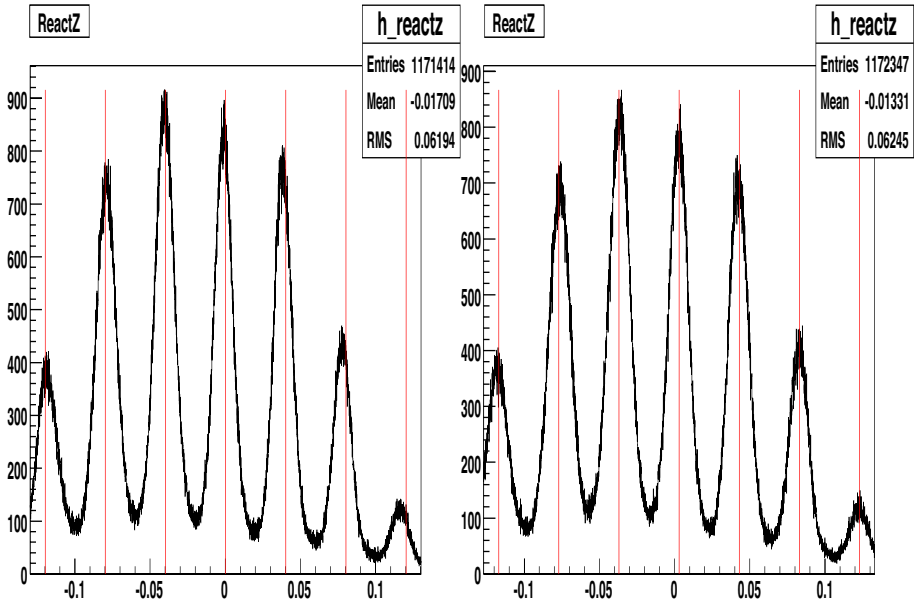

Figure 84: React_Z before and after optimization. The unit of the x-axis is a meter.

React_Z is the position of the scattering measured along the z-axis in the hall coordinate system. Since there are 7 foils for the "optics" target, separated by 4cm for each foil, we can see there are 7 peaks in Fig. 84. Before optimization, it is obvious that there exists an offset between expected values and the data for each foil, furthermore the offset is different. These offsets are calibrated back after optimization.

θ_{tg} and ϕ_{tg} are out-of-plane and in-plane angles respectively in the target coordinate system. Since there is a sieve slit in front of the entrance of the spectrometer, which includes 7x7 holes corresponding to 7x7 θ_{tg} vs ϕ_{tg} pattern it is clearly seen on the reconstructed data. Furthermore, a special feature built into the sieve are two large holes one in the center and the other in the corner that can been clearly seen in Fig. 85.

$$dp = (P - P_0)/P_0 \tag{6}$$

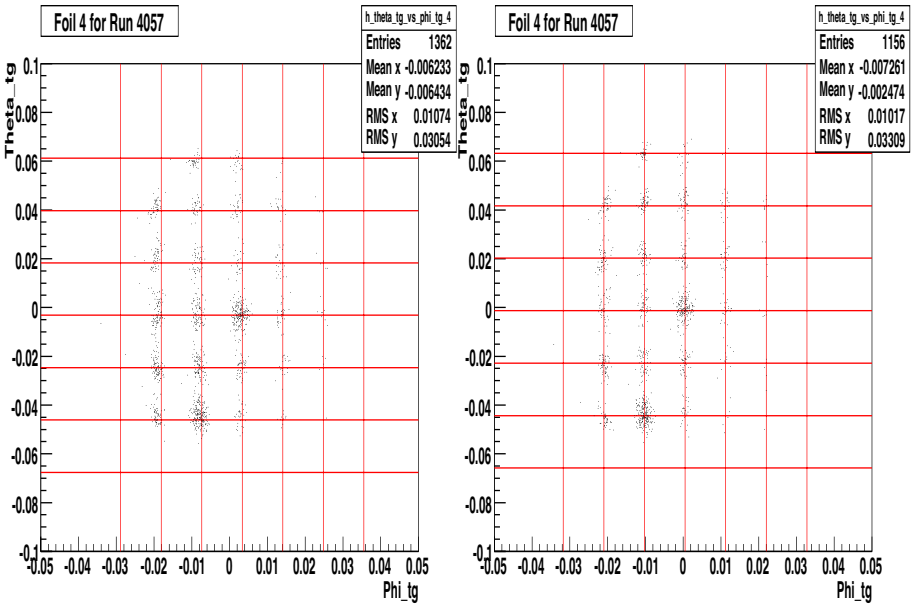

Figure 85: θ_{tg} vs ϕ_{tg} before and after optimization.

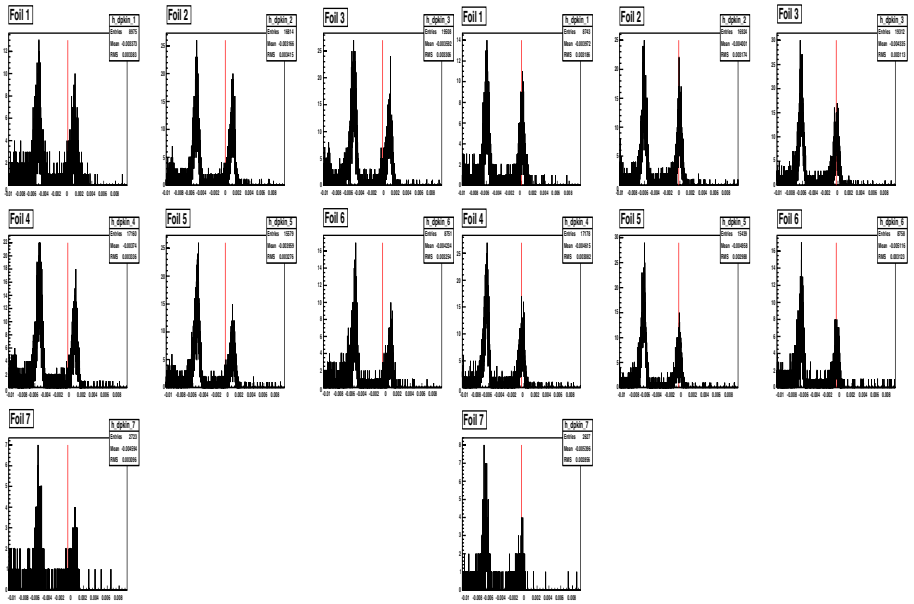

Figure 86: *dpkin* before and after optimization.

where P_0 is the spectrometer setting momentum. In theory,

$$P = \frac{E_{beam}}{1 + \frac{E_{beam} \cdot (1 - cos\Theta_{scat})}{M}} \tag{7}$$

M is the mass of the target. Θ_{scat} is the scattering angle. To remove the dependence on Θ_{scat}, we

introduce the *dpkin* variable, which is defined as

$$dpkin = dp - \frac{P(\Theta_{scat}) - P(\Theta_0)}{P_0} \tag{8}$$

here Θ_0 is the spectrometer angle.

Figure 86 shows *dpkin* for 7 foils. For each foil the peak on the right side is the elastic peak while the one on the left side is the first excited-state of carbon.

4.12 E06-002

PREX Developments in 2008

Contributed by R. Michaels

The Lead Radius Experiment (PREX), experiment E06-002, uses the parity violating weak neutral interaction to probe the neutron distribution in ^{208}Pb, thus measuring the RMS neutron radius to 1% accuracy, which has an important impact on nuclear theory, with widespread applications including neutron star structure. The experiment is being performed by the HAPPEX collaboration and is tentatively planned to run in January 2010.

In January 2008 we had a few days of beam time to test several issues as follows:

- **The lead/diamond target** was tested up to 100 μA. This is twice the beam current requested in the proposal. The target ran at 60μA for 5 days, 80μA for 1 shift, and 100 μA for 2 hours with no damage. The main improvement in the target was to ensure good contact between the lead and diamond. This is done by using a thin layer of vacuum grease between the foils, and by using a silver paste between the diamond and the copper frame. The silver paste does not see the beam, and the vacuum grease is a pure hydrocarbon and only $\sim 50\mu$m thick, so it's an acceptable background considering we already have carbon (diamond) foils. Also important is the use of Belleville washers on the clamp that squeezes the stack of foils together. These are spring-like washers which maintain the pressure as the target changes temperature.

- **A new detector concept**, designed at the University of Massachusetts and Smith College, was successfully tested. Two types of detectors will be deployed, a "thick" calorimeter with quartz/tungsten layers and a "thin" quartz detector. Both intercept the elastically scattered electrons, and the thin one is in front of the thick one in the path of electrons. The detectors and PMTs had good noise characteristics and were linear. Their energy resolution was $\frac{\sigma_E}{E} \sim 21\%$. This latter is important because the statistical noise gets blown up by a factor $\sqrt{(1+(\frac{\sigma_E}{E})^2)}$.

- **The microwave cavity position and current monitors** were tested down to 50 nA, a current necessary to do low-current measurements of Q^2 and backgrounds in counting mode. The resolution was roughly 150μm above 1 μA and 450 μm at 50 nA (these are upper bounds but are also adequate). The measurements should be repeated at some point because we mistakenly changed the gains during the test run. However, the signals looked strong enough to reach 10 nA with the present electronics. A new generation of electronics is being prepared by John Musson's group which will reach 0.1 nA and will have several improvements in noise reduction, cross-talk reduction, and ease of control and setup. New and more sensitive electronics for the striplines is also being prepared by Musson's group. These should be available by summer of 2009.

- **The luminosity monitor established a 50 ppm noise baseline.** This is an important milestone for the experiment. Due to the high rates in our detectors ($\sim$ 1 GHz), the noise from counting statistics will be very small (130 ppm for a 30 Hz helicity flip rate). Therefore all other sources of noise in a helicity period must be negligible compared to 130 ppm in order for counting statistics to dominate our error. The lumi provides a real-world test bench to check this; it integrates scattered electrons in quartz detectors at 0.5° to the beam, thus seeing an extremely high rate and providing a stringent test of the full electronics and DAQ

chain. A correlation analysis is required to remove natural noise due to beam movement. The result was noise of 50 ppm, thus establishing the adequacy of our electronics.

- **Tests of the Compton integrating method** had mixed results. This method is important for removing two sources of systematic error in our quest to reach 1% polarimetry. The two sources of error are the threshold cut normally used for counting mode and the deadtime. During the test we saw a clear photon signal and acceptable background, but there was a source of unacceptably high electronics noise which was not understood at the time. In the meantime, the group from Carnegie Mellon have solve this noise problem and we are ready to try again if we get development beam time.

Other activity on PREX from this year are as follows

- **Tests of the new 18-bit integrating ADCs**, designed at JLab by Fernando Barbosa and Ed Jastrzembski have shown an acceptable noise floor (8 ppm) and compare well to the Qweak ADC. A batch of the ADCs have been ordered. These ADCs replace our obsolete 16-bit ADCs from the HAPPEX-I era and provide improvements in pedestal sampling and bit resolution.

- **The new room-temperature septum magnet** has been designed by Paul Brindza and Al Gavalya. Detailed design work in preparation for fabrication is underway. The new scattering angle is 5° and the new optimal energy is 1.05 GeV with a tolerance of 50 MeV. This slightly improves our figure-of-merit and makes the Compton polarimetry easier compared to our original energy of 850 MeV. The magnet will be built in early 2009.

- **The Monte Carlo is being improved** and will be reported on in the Winter 2008 software workshop. This Monte Carlo is similar to others that have existed in Hall A. It is based on ROOT, written in C++, and uses John LeRose's model for HRS transport and acceptance. LeRose's model is written in Fortran, which is linked to the C++ framework.

- **Polarimetry:** The HAPPEX collaboration is contributing manpower to the Compton polarimeter upgrade. The Møller polarimeter is also being upgraded to have a higher magnetic field which saturates the target foils, and with several target orientations to study systematics. These upgrades are vital to the experiment and are reported on in other sections of the annual report.

4.13 E06-007

Impulse Approximation limitations to the $(e, e'p)$ reaction on ^{208}Pb, identifying correlations and relativistic effects in the nuclear medium

K. Aniol, A. Saha, J. Udias and G. Urciuoli, spokespersons,
and
the Hall A Collaboration.
contributed by K. Aniol.

E06-007, March 3 → March 26, 2007, and Jan. 21, 2008→Jan. 25, 2008, ^{208}Pb$(e, e'p)^{207}$Tl, ^{209}Bi$(e, e'p)^{208}$Pb
x_B=1, $q = 1$ GeV/c, $\omega = 0.433$ GeV, $Q^2 = 0.81$ to 1.97 GeV^2

4.13.1 Physics motivation

The question we wish to address in this measurement is " How well do we understand nuclear structure? ". The nucleus is a dense system of fermions whose motion to first order can be treated as independent particles moving in a mean field. The ^{208}Pb nucleus is the textbook example of a nucleus amenable to such an approach. This nucleus has been studied in the past at NIKHEF-K and Saclay by the $(e, e'p)$ reaction [1]. Spectroscopic factors were obtained from missing momenta less than 300 MeV/c and analyzed in the Impulse Approximation both with a nonrelativistic and relativistic treatment [2]. Deviations from independent particle motion for orbits near the Fermi energy are clearly present and are attributed to various correlations. Measurements on this nucleus at high missing momentum, $p_{miss} > 300$ MeV/c, [3] attribute the excess strength in the cross section as determined by a nonrelativistic analysis to long range correlations. However, a relativistic analysis of the bound and free nucleon states shows no need to invoke long range correlations [4]. In the relativistic treatment of the $(e, e'p)$ reaction the spinor distortions of the lower component of the nucleon wave function account for the cross section at high missing momentum in the case of the measurement of [3]. In that experiment the measurement was done far from quasi-elastic conditions due to limitations of beam energy. At Jefferson Lab we can measure $(e, e'p)$ on ^{208}Pb at $x_B = 1$, for which both nonrelativistic and relativistic treatments predict the same high missing momentum cross sections when the spectroscopic factors are properly normalized. Excess strength at high p_{miss} can then be attributed to long range correlations.

The asymmetry A_{TL}, accessible in $(e, e'p)$ reactions, is a relatively new and as yet little exploited observable for low lying excited states. It was not possible to measure this quantity at previous laboratories. Our measurement is the first one to measure the cross section at negative p_{miss} (angles forward of the three momentum transfer). For missing momenta below 300 MeV/c the mean field potential is primarily responsible for the nucleon's state and other mechanisms are negligible. A_{TL} is sensitive to the theoretical approach (nonrelativistic vs relativistic) employed and is of prime interest in this measurement.

It has been claimed [5, 6], from the comparison of $(e, e'p)$ data in ^{12}C at different momentum transfers, that the spectroscopic factors as measured in $(e, e'p)$ reactions at exclusive conditions display a dependence on the momentum transfer. This dependence would saturate at Q^2 of around 1 GeV^2 [6]. Subsequent studies on ^{16}O including data from 0.2 to 0.8 GeV^2 did not find evidence for such Q^2 dependence (see for instance ref. [7]). This experiment at Hall A can settle this issue since we can efficiently measure the cross sections for low p_{miss} at Q^2 between 0.81 to 1.97 GeV^2.

4.13.2 Objectives

1. Long Range Correlations search

   (a) Measure spectroscopic factors for states near the Fermi level. Spectroscopic factors depend on short range correlations (SRC) and long range correlations (LRC).

   (b) Measure cross sections for these low lying states to 500 MeV/c in p_{miss}. Excess strength here is theoretically identified as due to LRC.

   (c) Search for Q^2 dependence of spectroscopic factors.

2. Identify dynamical relativistic effects in nuclear structure.
   Measure cross section asymmetry A_{TL} around the three momentum transfer. Relativistic mean field theory predicts an A_{TL} dependence on $p_{miss} < 300$ MeV/c due to dynamical enhancement of the lower component of the nucleon wave function. Calculations which do not include the enhancement of the lower component predict a substantially different A_{TL} behavior.

4.13.3 Activities in 2008

Most of the effort this year was focused on continuing the analysis of the 2007 data. We also had a 5 day run in January 2008 to accumulate more data at the large missing momentum region, $p_{miss} > 300$ MeV/c. This second run was in collaboration with the PREX tests. A new target ladder holder was designed and built for this run. The electron beam energy was slightly higher in January 2008, 2.775 GeV, but the same values of (ω, q) were investigated as in the 2007 runs.

4.13.4 Data analysis from 2007 run

Raster/Optics Studies

Considerable effort went into improving the resolution. This required extensive optics optimization and detailed examination of the raster corrections on a run by run basis. The resolution we achieved is in agreement with the simulation which is 1 MeV FWHM for the diamond/lead/diamond sandwich targets. An example of the separation of the states is more clearly seen in a two dimensional plot of p_{miss} vs e_{miss}, Fig. 87 for ^{208}Pb$(e,e'p)^{207}$Tl at the $p_{miss} = 0$ setting. The large momentum acceptance of the Hall A spectrometers reveals the missing momentum dependence of the excited states in ^{207}Tl. A projection onto the e_{miss} axis is seen in Fig. 88. An example of the best resolution with a fit for the ^{12}C target is shown in Fig. 89. Our experience is that the data analysis will be a lengthy procedure since we want to apply this process to all the low p_{miss} spectra.

Cross Sections

Cross section determinations for the lead target face two main experimental challenges. The first is the acceptance correction since the low count rate requires the use of the entire solid angles of the spectrometers. Our first investigation of the acceptance correction used the cross section

for the reaction $^{12}C(e,e'p)^{11}B_{gs}$ at $p_{miss} = 100$ MeV/c. This is a large cross section and we could investigate the effect on the average cross section as a function of spectrometer solid angle and momentum bite cuts. An example of a spectrum with restricted solid angles is shown in Fig. 90. For the wide open solid angle measurement we see an increase in the FWHM of the peaks, Fig. 91. The average cross section is expected to change as a function of solid angle because of instrumental effects(acceptance efficiencies) and for physics reasons. This effect is seen in Fig. 92 for the cross sections extracted from the excited states. Since we have a theoretical model for the cross section we can gauge how much of the change in the average cross section is due to the physics of the reaction. We compared the ratio of data/theory for the ground state transition, Fig. 93, and found for this case that the ratio tends to about 0.65 as the solid angle shrinks. We will use the same technique for other kinematic points to see if this is a reliable method of determining the acceptance efficiency for the low count rate lead data. The same sort of analysis of the cross sections as a function of momentum bite showed that the average cross sections were independent of the momentum bite.

The second challenge for obtaining the cross sections is the large raster pattern we had to use. In this first analysis of the raster effect we had not yet obtained the complete raster correction to the resolution as described in the previous section. The effect was to broaden the resolution beyond the raster off case. Nevertheless, the spectrum fitting procedure allowed us to extract the same cross section for the $^{11}B_{gs}$ transition with raster on or raster off, as seen in Fig. 94.

The large raster pattern also was a problem for some runs in which the beam scraped the target holder frame. In these cases we excluded those events from the analysis. The cross section determinations require the knowledge of the total relevant charge collected. The raster pattern is very uniform in Hall A [8] and we checked this also by studying the count rate in the spectrometers as a function of the cut in the raster pattern. Cutting out a piece of the raster pattern introduces an uncertainty in the amount of charge, nevertheless, which at present in our analysis introduces an uncertainty of 5 to 10% in the cross section. The uniformity of the raster pattern allows the effective charge to be determine from a simple geometric ratio of the size of the raster pattern cut to the total area of the raster pattern. This normalization of the charge was particularly important for the bismuth target which slipped in the target holder and was only partially exposed to the beam.

Our preliminary cross sections are in Table 10. There are more cross sections available in our data than included in this table. We have other kinematic settings for bismuth and the carbon cross sections were measured for each of the lead settings. We will continue further with our study of the raster and acceptance efficiency effects on the cross sections. At present we assign a 20% systematic uncertainty to the cross sections.

Q^2 dependence of spectroscopic factors

Cross sections were measured for $Q^2 = 0.81, 1.40, 1.97$ GeV^2 at $p_{miss} = 0$ with the goal of determining whether or not the spectroscopic factors obtained from the $(e,e'p)$ reaction are independent of Q^2. We did not have enough time to measure the cross sections at several values of low missing momenta but decided to concentrate on the lowest kinematic setting. However, the nominal setting at $p_{miss} = 0$ actually covers a very wide range in missing momenta, see Fig. 87, and, in fact, captures protons on both sides of the three momentum transfer. The cross sections for these values of Q^2 are in Table 11. The agreement between theory and data is not good. Before drawing any firm conclusions about this comparison we will elaborate the theory simulation over

the experimental acceptance. The theory simulation in Table 11 treats the theory cross section as factorizable in the integration over the acceptances, properly taking into account the p_{miss} variation over the solid angle. A fully unfactorized simulation of the theory is called for before we can draw a firm conclusion. We expect the theory simulation to be especially sensitive to its method of execution for the low p_{miss} conditions under which the data were measured.

Left - Right asymmetry, A_{TL}

The left-right asymmetry, A_{TL} was measured out to $p_{miss} = 400$ MeV/c. The data for the integrated cross section up to 6 MeV in ^{207}Tl are displayed in Fig. 95. Given our present level of systematic uncertainty there is no striking difference between the two theoretical approaches, relativistic or non relativistic for the $(e, e'p)$ reaction. Qualitatively the relativistic treatment predicts a larger negative asymmetry, which is more consistent with our data. The largest difference appears to be at about 290 MeV/c where the two predictions differ dramatically.

Long Range Correlations

If long range correlations were important to explain the cross sections for $p_{miss} > 300$ MeV/c then the measured cross sections should be factors of 2 to 3 bigger than predicted by the mean field values. This prediction is robust between relativistic and non relativistic theories, both approaches giving comparable cross sections at large missing momenta. An investigation of the measured cross sections and the simulated theory values from Table 10 for $p_{miss} = 300, 400$ MeV/c shows that the mean field predictions are very close to the measured values. There seems to be little room for invoking long range correlations to predict the cross sections at large missing momenta.

4.13.5 Run time experience in 2008

Target Development
Based on our experience in the March 2007 run a new target holder design was developed, however, the diamond/lead/diamond sandwich was still used. The January 2008 run was in collaboration with the PREX collaboration which also needs a lead target capable of handling large currents. A thick copper target holder with special compression washers and silver paste to improve the thermal contact of the diamond foils to the frame was built. It was not necessary to cool the target with flowing cryogenic helium with this design. The thermal contact of the target ladder with the cold cryogenic Hall A target provided sufficient heat conduction to maintain the integrity of the targets. Most of our data were collected at 60 μA but there were 8 hours runs also at 80 μA. The PREX collaboration subsequently tested the 0.5mm natural lead target with a 100 μA beam for three hours and saw no deterioration in the target. The improved target ladder design also allowed for the large rastered beam to pass through the target without striking the frame. A view of the target ladder from the beam exit side is seen in Fig. 96. The beam entrance view showing the flared entrance window design to accomodate the large raster pattern is seen in Fig. 97.

Data at large p_{miss} were the focus of the January 2008 run, Fig. 98. Most of the effort so far has been to improve the coincidence time resolution, 4 ns at present. This is particularly important at these large p_{miss} settings where the cross sections of interest are small and the random rates are large.

4.13.6 Figures, Tables, Equations, and References

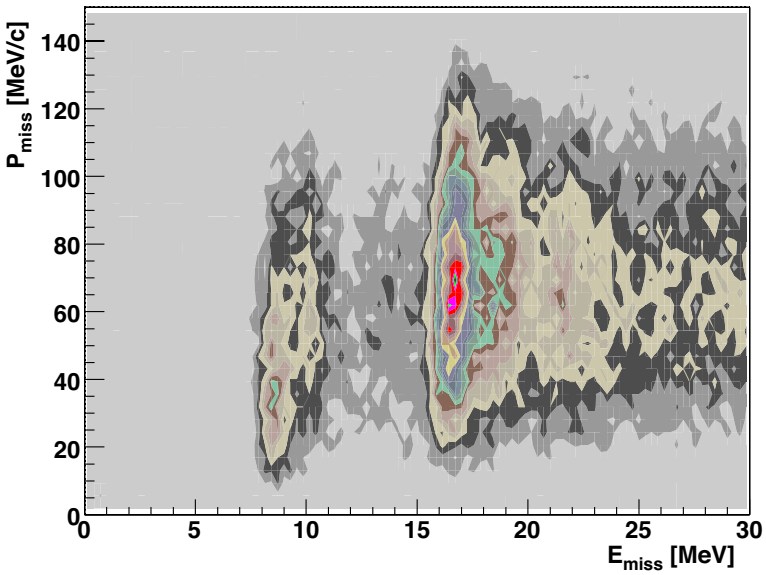

Figure 87: ^{208}Pb$(e,e'p)^{207}$Tl, p_{miss} vs e_{miss} for the $p_{miss} = 0$ setting.

References

[1] E. Quint, *Limitations of the mean-field description for nuclei in the Pb-region, observed with the (e,e'p) reaction.* PhD thesis, Universiteit van Amsterdam, March 15, 1988, unpublished, NIKHEF-K Nr. 1313.

[2] J. M. Udias *et al.* Phys. Rev. C **48**, 2731 (1993).

[3] I. Bobeldijk *et al.*, Phys. Rev. Lett. **73**, 2684 (1994).

[4] J. M. Udias *et al.* Phys. Rev. C **51** 3246 (1996).

[5] L. Lapikas *et al.* Phys. Rev. C **61** 064325 (2001).

[6] L. Frank *et al.* Phys. Lett. B **503** 73 (2001).

[7] J. M. Udias *et al.* Phys. Rev. C **64** 024614 (2001).

[8] J. Yan *et al.* NIM **539A** 1 (2005).

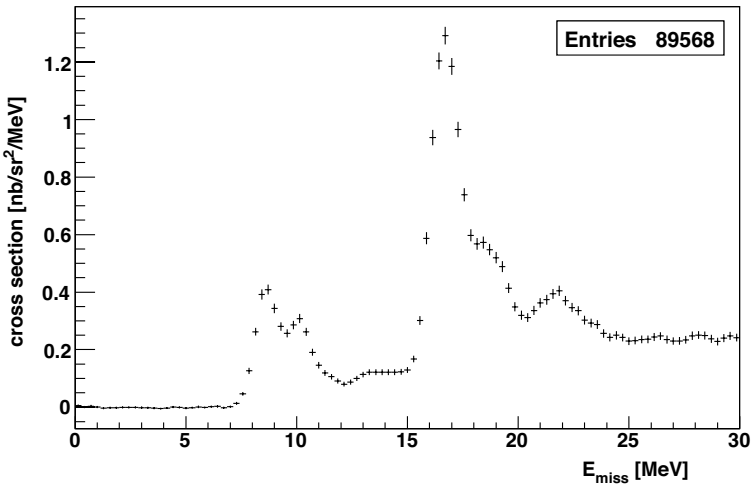

Figure 88: ^{208}Pb$(e,e'p)^{207}$Tl, e_{miss} for the $p_{miss} = 0$ setting. The two ^{207}Tl states at 10 MeV in e_{miss} are the $3s_{1/2}$ ground state and the excited $2d_{3/2}$ state at 1.683 MeV.

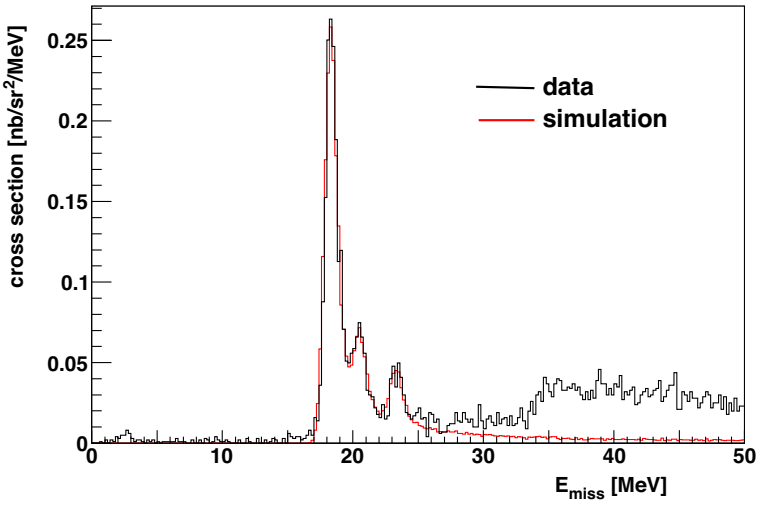

Figure 89: ^{12}C$(e,e'p)^{11}$B, e_{miss} for the $p_{miss} = 0$ setting illustrating the best resolution obtained for the ^{12}C target. A fit to the ground state and some excited states of ^{11}B is shown.

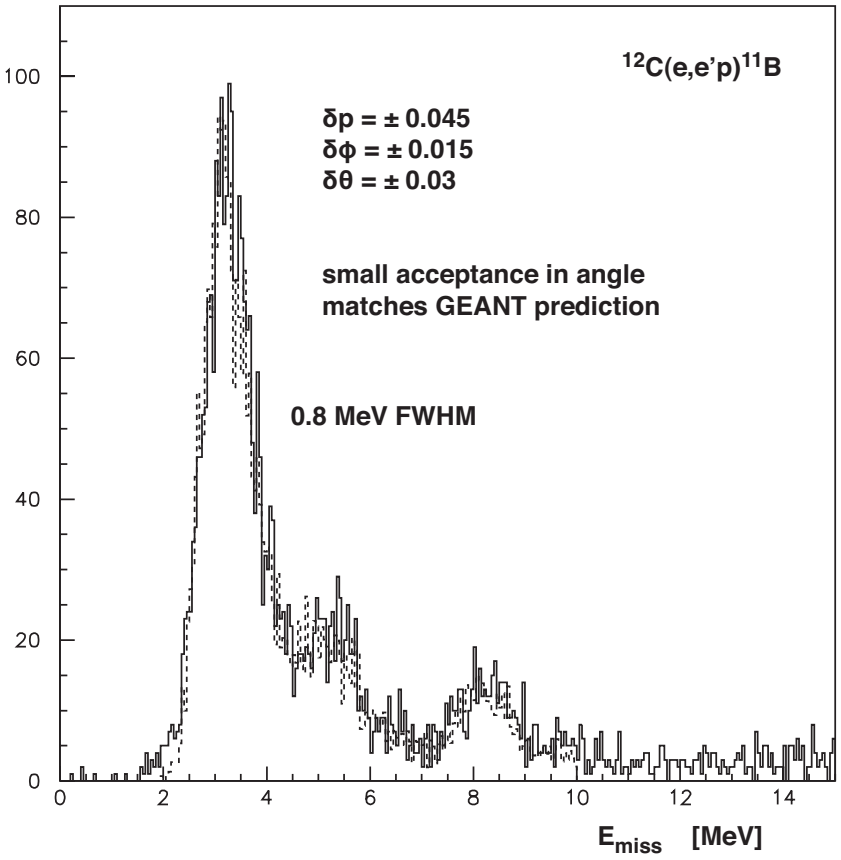

Figure 90: $^{12}\mathrm{C}(e,e'p)^{11}\mathrm{B}$, $p_{miss} = +100$ setting, restricted solid angles. The fit to the spectrum is shown.

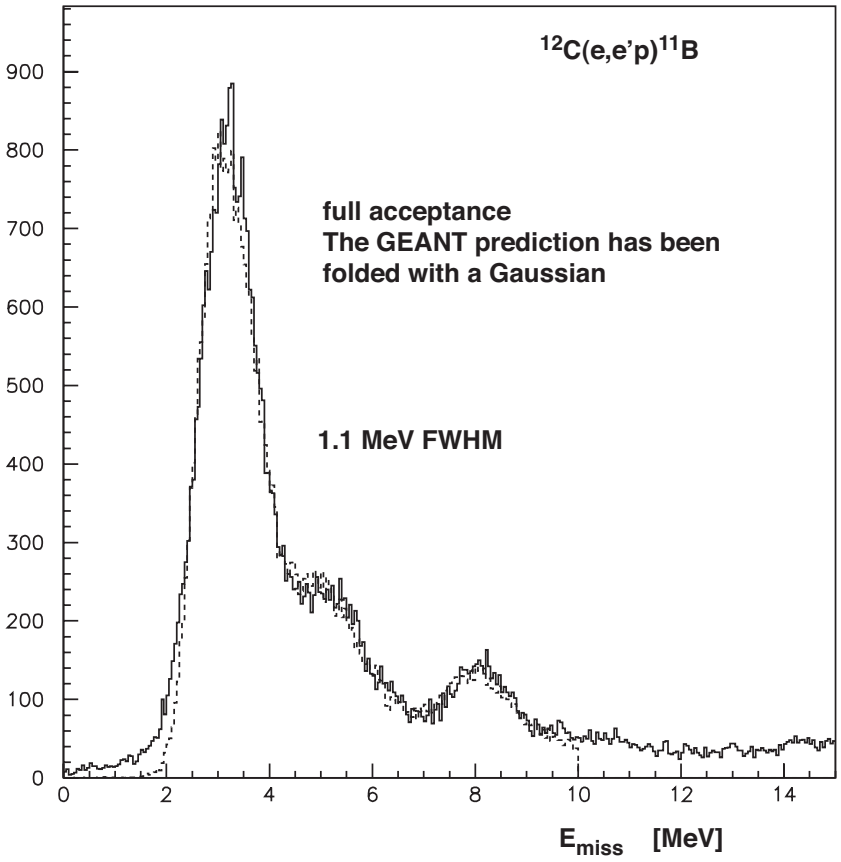

Figure 91: ^{12}C$(e,e'p)^{11}$B, $p_{miss} = +100$ setting, full solid angles. The fit to the spectrum is shown.

^{12}C(e,e'p)^{11}B preliminary cross sections at p_{miss} = 100 MeV/c
Raster off, |dp|<0.045

^{11}B state (MeV)	dphi,dtheta full	|dphi|<0.02, |dtheta|<0.04
Gs	2.92	3.30
2.124	0.44	0.45
5.020	0.26	0.36

Units 10^{-33} cm^2/MeV/sR^2

The average cross section as a function of acceptance should change.

Figure 92: ^{12}C$(e,e'p)^{11}$B, $p_{miss} = +100$ setting, Extracted cross sections for different solid angle cuts.

^{12}C(e,e'p)^{11}B$_{gs}$ average cross sections and theory

|dp|<0.045	Raster off results	
phi wide open theta wide open	1.10 MeV, FWHM sig = 2.92e-33 cm^2/sr^2/MeV <theory> = 5.03e-33 data/theory = 0.58	Theory assumes there are 4.0 protons in the 1p3/2 shell.
|phi| < 20 |theta| < 40	0.95 MeV, FWHM sig = 3.30e-33 <theory> = 5.13e-33 data/theory = 0.64	Theory is averaged over the acceptance to the entrance of the spectrometers.
|phi| < 15 |theta| < 30	0.79 MeV, FWHM sig = 3.35e-33 <theory> = 5.16e-33 data/theory = 0.65	

Figure 93: $^{12}\mathrm{C}(e,e'p)^{11}\mathrm{B}$, $p_{miss} = +100$ setting, theory vs data for different solid angle cuts for the ground state of ^{11}B. These cross sections imply that there are 2.4 to 2.6 protons in the $1p_{3/2}$ ground state, consist with previous results from NIKHEF and Saclay.

Comparison of raster on/off cross sections for ^{12}C(e,e'p)^{11}B

phi wide open theta wide open dp - no cut	1.10 MeV, FWHM sig = 2.92e-33 cm^2/sr^2/MeV <theory> = 5.03e-33 data/theory = 0.58	1.41 MeV, FWHM sig = 2.80e-33 <theory> = 5.03e-33 data/theory = 0.56
|phi| < 20 |theta| < 40 dp -no cut	0.95 MeV, FWHM 3.30e-33 <theory> = 5.13e-33 data/theory = 0.64	1.21 MeV, FWHM sig = 3.30e-33 <theory> = 5.13e-33 data/theory = 0.64
	Raster is off	Raster is on

Raster on/off cross sections agree but FWHM is larger for raster on.

Figure 94: $^{12}\mathrm{C}(e,e'p)^{11}\mathrm{B}$, $p_{miss} = +100$ setting, theory vs data for different solid angle cuts for the ground state of ^{11}B with the raster on or off. These cross sections imply that there are 2.4 to 2.6 protons in the $1p_{3/2}$ ground state, consist with previous results from NIKHEF and Saclay.

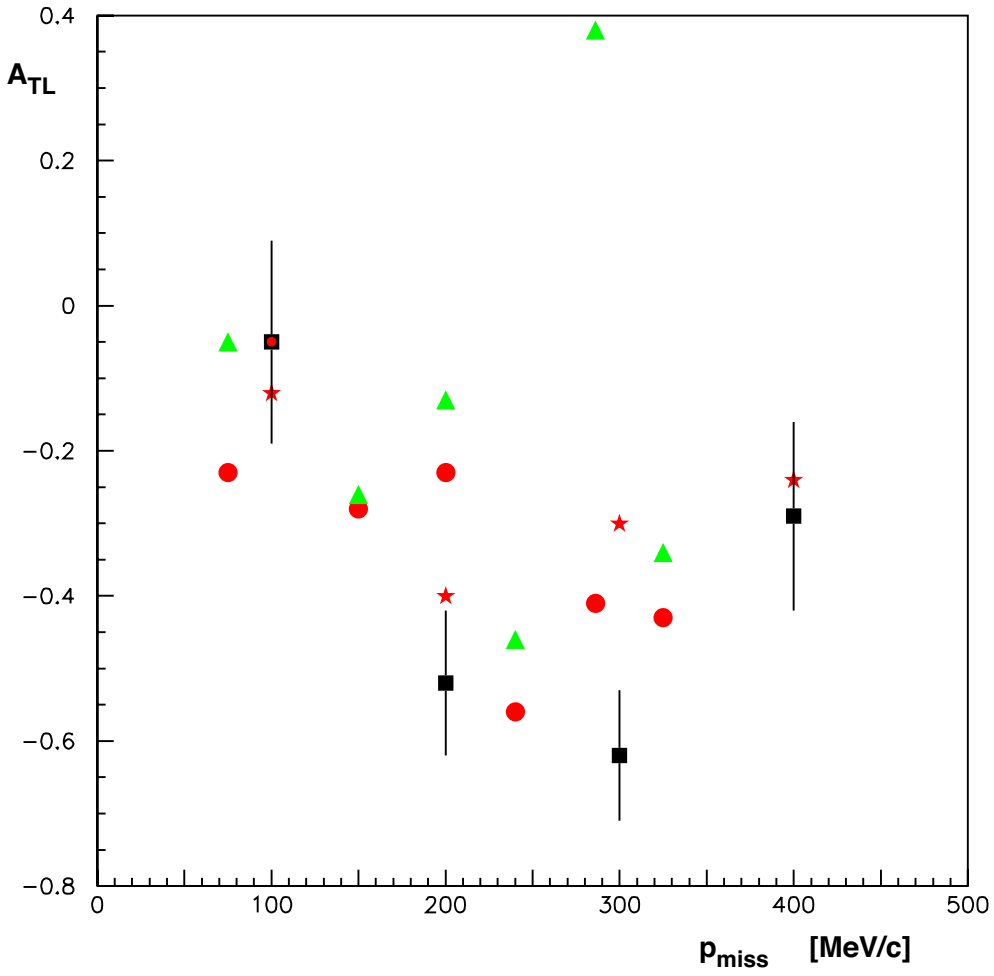

Figure 95: A_{TL} for the sum of states in ^{207}Tl for the first 6 MeV of excitation. Data (black squares), non-relativistic theory (green triangles), relativistic theory (red circles), relativistic theory with same E_{miss} cut as data (red stars).

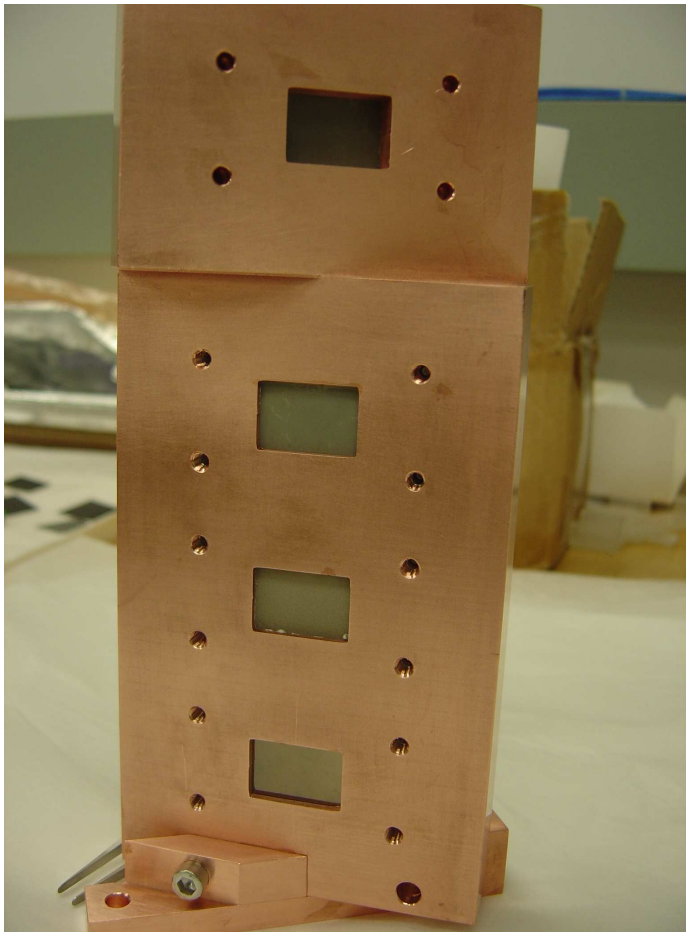

Figure 96: New target design for the 2008 E06-007 run and PREX tests. Beam exit view. Top is thick (0.5 mm) natural lead, next is thick (0.5 mm) ^{208}Pb, then thin (0.17 mm) ^{208}Pb, bottom ^{209}Bi, (0.207 mm).

Figure 97: New target design for the 2008 E06-007 run and PREX tests. Beam entrance view with flared windows.

E06007 – Run 2 (Jan 2008)

Charge in Coulombs (time) Run Nos.

Kinematics (Pmiss)	Thick Pb	Thin Pb	Bi	C
Kin 8 (+400)	2.723 (919) 3151-3184	2.329 (605) 3337-3354		
Kin 9 (−400)	1.469 (572) 3236-3272	0.632 (158) 3367-3373		
Kin 10 (+500)	2.592 (849) 3185-3221	0.177 (55) 3273-3275 1.132 (258) 3355-3364		
Kin 11 (−500)		2.130 (646) 3276-3306		
Kin 1 (0)	0.201 (57.4) 3228-3230 0.048 (14.5) 3310-3311 0.054 (15.2) 3366	0.229 (78) 3232-3234 0.110 (32) 3309 0.047 (16.6) 3365		0.202 (59) 3231
Kin 2 (+100)	0.215 (60.5) 3222-3227			
Kin 3 (-100)		0.21 (60) 3307-3308		
Kin 4 (+200)			0.562 (183) 3312-3336	

Figure 98: List of targets and charge collected for the January 2008 run

Table 10: Preliminary cross sections from the March 2007 data, $Q^2 = 0.81$ GeV^2. For the lead target the cross sections for the integral up to 6 MeV in excitation energy in ^{207}Tl are listed. The theoretical cross sections are adjusted to account for the loss of counts in the radiative tails beyond 6 MeV in excitation. For the carbon and bismuth targets the ground state cross sections are based on spectrum fitting including the full radiative tail. At this point in the analysis an over all systematic error of 20% is assigned to the cross sections. Cross sections measured in nb/MeV/sr^2.

p_{miss} MeV/c setting	lead data 0<E<6 MeV	lead theory† 0<E<6 MeV	carbon data ground state	carbon theory† ground state	bismuth data ground state	bismuth theory† ground state
0	4.07	3.6	2.8	2.07		
+100	3.23	5.56	3.3	3.6		
-100	2.94	4.22				
+200	4.50	4.52	1.45	1.22	0.37	0.38
-200	1.42	1.88				
+300	0.23	0.23				
-300	0.054	0.12				
+400	0.020	0.015				
-400	0.011	0.0087				

†The preliminary results quoted here include most of the range of values of ϕ (the angle between electron and nucleon scattering planes) present in the data, given the acceptance of the experiment. For the kinematics setting with lowest value of p_{miss}, ϕ can differ significantly from 0 or π. While the theory results quoted here include to some extent the effect of this finite ϕ range, further work is required to test whether: a) the ϕ range included in the simulation is similar to the one seen in the data. This requires a good control on the radiation effects in the simulation. b) The dependence of the observed cross-section data on ϕ can be explained by the theoretical predictions for R_{tt} and R_{tl}. Thus, from all the preliminary results shown in this report, the theoretical predictions for the lowest p_{miss} kinematics are the ones that will most likely change as the analysis progresses.

Table 11: Preliminary cross sections from the March 2007 data, $Q^2 = 0.81, 1.40, 1.97$ GeV^2 for the $p_{miss} = 0$ setting. For the lead target the cross sections for the integral up to 6 MeV in excitation energy in ^{207}Tl are listed. The theoretical cross sections are adjusted to account for the loss of counts in the radiative tails beyond 6 MeV in excitation. For the carbon target the ground state cross sections are based on spectrum fitting including the full radiative tail. At this point in the analysis an over all systematic error of 20% is assigned to the cross sections. Cross sections measured in nb/MeV/sr^2.

Q^2 GeV^2	lead data 0<E<6 MeV	lead theory† 0<E<6 MeV	carbon data ground state	carbon theory† ground state
0.81	4.07	3.6	2.8	2.07
1.40	0.745	0.90	0.54	0.24
1.97	0.246	0.18	0.20	0.06

†The preliminary results quoted here include most of the range of values of ϕ (the angle between electron and nucleon scattering planes) present in the data, given the acceptance of the experiment. For the kinematics setting with lowest value of p_{miss}, ϕ can differ significantly from 0 or π. While the theory results quoted here include to some extent the effect of this finite ϕ range, further work is required to test whether: a) the ϕ range included in the simulation is similar to the one seen in the data. This requires a good control on the radiation effects in the simulation. b) The dependence of the observed cross-section data on ϕ can be explained by the theoretical predictions for R_{tt} and R_{tl}. Thus, from all the preliminary results shown in this report, the theoretical predictions for the lowest p_{miss} kinematics are the ones that will most likely change as the analysis progresses.

4.14 E08-007

Measurement of the Proton Elastic Form Factor Ratio at Low Q^2

J. Arrington, R. Gilman, A.Sarty, G. Ron, D.W. Higinbotham, D. Day
and
the Hall A Collaboration
contributed by Xiaohui Zhan

4.14.1 Physics Motivation

The goal of E08-007 is to vastly improve the knowledge of the proton form factor ratio at low Q^2 (0.3 GeV^2 - 0.7 GeV^2) through the recoil polarization method. In combination with separate cross section data, it will also allow significant improvements in the knowledge of the individual form factors. Figure 99 shows recent high-precision world data sets [1, 2, 3] at low Q^2. The most recent set [3] shows substantial deviations of the ratio from unity, and indicates form factor parameterizations generally overestimate the proton electric form factor. The new E08-007 high precision measurement will either confirm or refute such deviations. Beyond the intrinsic interest in the structure of the nucleon, improved knowledge of the form factor also has implications for DVCS, the proton Zemach radius, and the extraction of the strange quark content of the nucleon through parity violation experiments.

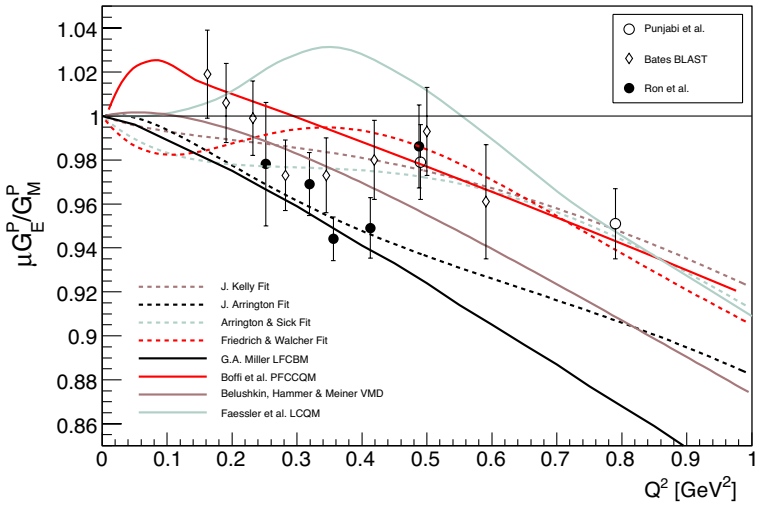

Figure 99: Most recent world data compared to several fits and parameterizations.

4.14.2 Overview of the Experiment

The experiment started running May 15, 2008 and ended on June 9, 2008. With beam polarization ~80%, we were able to achieve $< 1\%$ statistical uncertainties for all the kinematics. We used HRSL to detect the recoil protons in coincidence with the elastic scattered electrons detected by BigBite. The focal plane polarimeter installed in HRSL was used to measure the recoil polatization of the proton. The BigBite calorimeter was used to tag the electrons and form the coincidence

trigger. Table 12 lists the measured kinematics. For data taking, only selected shower blocks

Table 12: Kinematics for HRSL and BigBite. For each Q^2, there are 3 different spectrometer momentum settings (centering the protons at about δ=-2%, 0%, and +2%) to cover different regions on the focal plane.

Setting	Q^2 [GeV/c]^2	θ_p [deg]	P_p [GeV/c]	θ_e [deg]	P_e [GeV/c]
1	0.3505	57.5	0.6162	30.0	1.0072
2	0.2995	60.0	0.5648	30.0	1.0344
3	0.4512	53.0	0.7097	35.0	0.9536
4	0.4051	55.0	0.6680	35.0	0.9782
5	0.5494	49.0	0.7936	40.0	0.9012
6	0.4993	51.0	0.7515	40.0	0.9279
7	0.6013	47.0	0.8359	45.0	0.8736
8	0.6958	43.5	0.9131	50.0	0.8232

on BigBite were turned on for each setting to reduce the background rate. Figure 100 shows an example of the elastic spectrum in HRSL. For each setting, aluminium dummy data were taken for background estimation, and the preliminary analysis shows the inelastic background is less than 0.3%. The accidental background is also small ($< 0.3\%$) with a proper coincidence timing cut – see Figure 101.

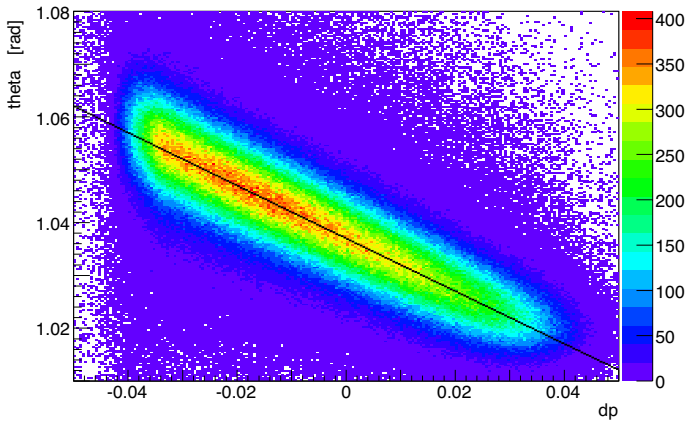

Figure 100: Proton scattering angle vs. δ for $Q^2 = 0.5$ GeV^2. The expected elastic peak position is shown as a solid black line.

The FPP chambers were used to detect the angular distribution of the protons after scattering in the carbon analyzer. The interaction between polarized protons and carbon nuclei induces an asymmetric distribution along the azimuthal scattering angle ϕ. Including false asymmetries, the angular distribution for a sample of incident protons is represented by equation 9:

$$f(\theta,\phi) = \frac{1}{2\pi}[1 + (a_0 - A_y P_x^{fpp})\cos\phi + (b_0 + A_y P_y^{fpp})\sin\phi + c_0\cos 2\phi + d_0 \sin 2\phi] \quad (9)$$

By taking the difference between the distributions with different beam helicity states, the false asymmetry terms cancel out, and the difference distribution has the simple form

$$f^{diff}(\theta,\phi) = f^{+}(\theta,\phi) - f^{-}(\theta,\phi) \approx \frac{1}{\pi}[A_y(P_x^{fpp}\cos\phi - P_y^{fpp}\sin\phi)] = C\cos(\phi+\delta) \quad (10)$$

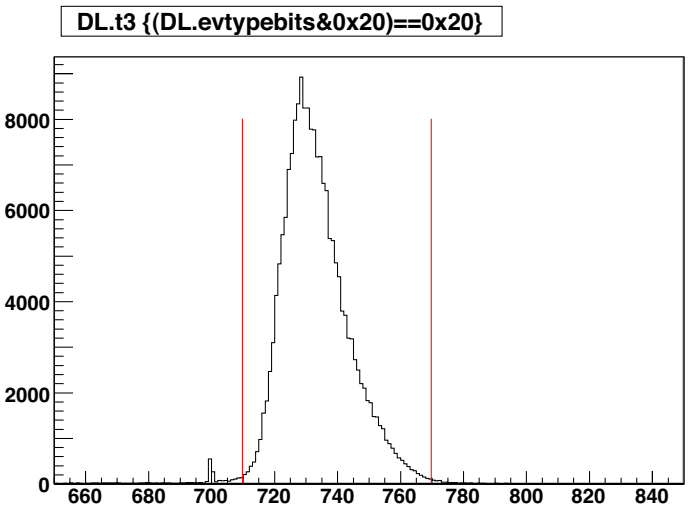

Figure 101: Coincidence timing on T3.

where

$$C = \frac{1}{\pi} A_y \sqrt{(P_x^{fpp})^2 + (P_y^{fpp})^2}, \text{ and} \tag{11}$$

$$\tan\delta = \frac{P_y^{fpp}}{P_x^{fpp}}. \tag{12}$$

The phase shift δ is a measure of G_E^p/G_M^p. Figure 102 shows the fit for kinematics 6, $\delta = -2\%$. The red dashed line is a hypothetical distribution assuming $\mu_p G_E^p/G_M^p = 1$, as predicted by form factor scaling. A small, but clear, phase shift can be seen. Although the proton polarization com-

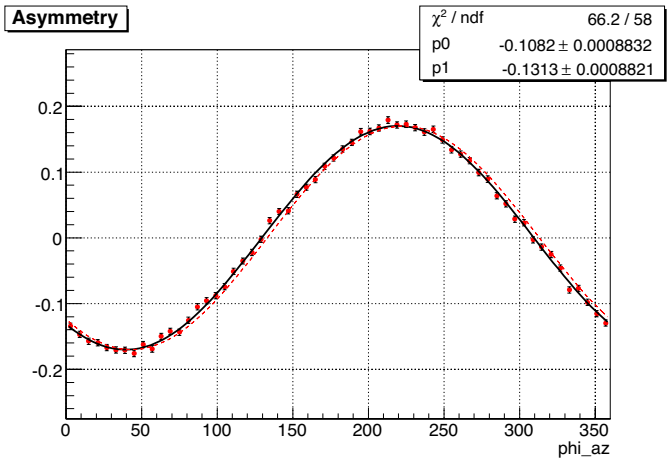

Figure 102: Difference distribution at the focal plane between the two helicity states, as a function of the azimuthal scattering angle. The data are at $Q^2 = 0.50$ GeV^2. The solid curve is a sinusoidal fit to the data. The dashed line indicates the distribution expected if $\mu_p G_E^p/G_M^p = 1$.

ponents can be obtained from the focal plane asymmetry, the relationship between the polarization components at the target and at the focal plane is complicated. The dipole approximation is too naive to describe the HRS magnetic system. The full precession matrix is given by COSY, which is

a differential algebra based code for the simulation, analysis and design of partical optics systems. The full matrix that relates the focal plane and target polarizations takes the general form:

$$\begin{pmatrix} P_x^{fpp} \\ P_y^{fpp} \end{pmatrix} = \begin{pmatrix} S_{xy} & S_{xz} \\ S_{yy} & S_{yz} \end{pmatrix} = \begin{pmatrix} P_y^{tg} \\ P_z^{tg} \end{pmatrix}$$

The S_{ij} coefficients depend on the trajectory of the proton in the spectrometer. The matrix is fully calculated for each event using the coordinates of the individual proton at the target:

$$S_{ij} = \sum_{k,l,m,n,p} C_{ij}^{klmnp} x^k \theta^l y^m \phi^n \delta^p.$$

The precise extraction of the form factor ratio is by a maximum-likelihood technique, described in [4].

4.14.3 Preliminary analysis

After several months of data analysis, we are able to give preliminary projected statistical uncertainties (see Fig. 103 and Table 13). We are still working on the systematic uncertainty analysis. The major source of uncertainty comes from the proton spin precession inside the spectrometer, which is crucial in determining the form factor ratio. Also, these statistical errors were calculated by ignoring the carbon analyzing power. With proper analyzing power, the statistical uncertainty could be further reduced.

Table 13: E08-007 projected statistical uncertainties.

Q^2[GeV^2]	Δ_r[%]
0.30	0.99
0.35	0.71
0.40	0.58
0.45	0.71
0.50	0.48
0.55	0.62
0.60	0.58
0.70	0.51

References

[1] V. Punjabi *et al.*, Phys. Rev. C **71**, 055202 (2005).

[2] C.B. Crawford *et al.*, Phys. Rev. Lett. **98**, 052301 (2007).

[3] G. Ron *et al.*, Phys. Rev. Lett. **99**, 202002 (2007).

[4] G. Quéméner *et al.*, Nucl. Phys. **A**, 654:543 (1999).

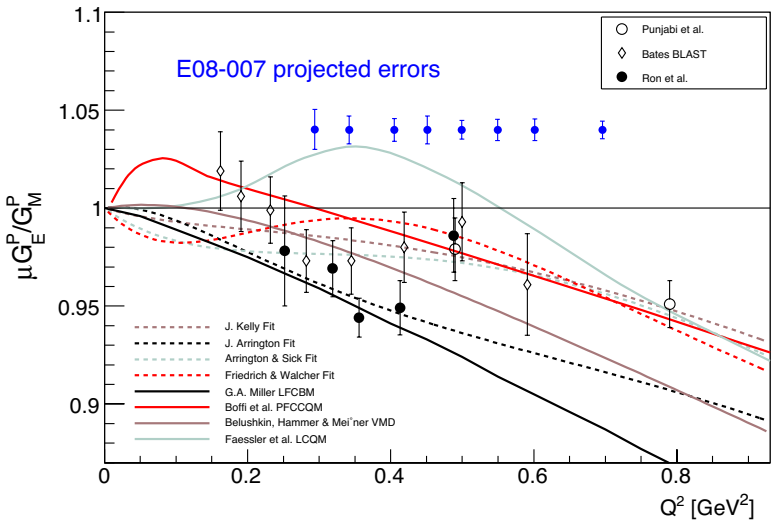

Figure 103: E08-007 projected statistical uncertainties together with the world data and several fits.

5 Hall A Collaboration Member List

Argonne National Lab:
John Arrington
Frank Dohrmann
Paul Reimer
Patricia Solvignon
Krishni Wijesooriya

Budker Institute of Nuclear Physics:
Dima Nikolenko
Igor Rachek

Cairo University:
Hassan Ibrahim

California Institute of Technology:
Steffen Jensen
Cathleen Jones

California State University:
Konrad A. Aniol
Juan Carlos Cornejo
Martin B. Epstein
Dimitri Margaziotis

Carnegie Mellon University:
Gregg Franklin
Diana Parno
Brian Quinn
Luminita Todor

China Institute of Atomic Energy (CIAE):
Shuhua Zhou

College of William and Mary:
David S. Armstrong
Todd Averett
Keith Griffioen
Joe Katich
Aidan Kelleher
Lubomir Pentchev
Charles Perdrisat

Dapnia/SphN:
Etienne Burtin
Christian Cavata
Nicole d'Hose
Jean-Eric Ducret
Stephanie Escoffier
Bernard Frois
Sophie Kerhoas
David Lhuillier
Jacques Marroncle
Damien Neyret
Stephane Platchkov
Thierry Pussieux
Franck Sabatie
Antonin Vacheret
Pascal Vernin

Duke University:
Steve Churchwell
Haiyan Gao
Calvin Howell
Xin Qian

Yi Qiang
Richard Walter

Faculte des Sciences de Monastir (Tunisia):
Malek Mazouz

Florida International University:
Armando Acha
Werner Boeglin
Luminiya Coman
Marius Coman
Laird Kramer
Pete Markowitz
Brian Raue
Jeorg Reinhold

Fudan University:
Xiaofeng Zhu

General Electric:
Jianguo Zhao

Gent State University:
Natalie Degrande
Luc Van de Hoorebeke
Robert Van de Vyver

Gesellschaft fur Schwerionenforschung (GSI):
Javier Rodriguez Vignote

Hampton University:
Leon Cole
Ashot Gasparian
Peter Monaghan

Harvard Medical School:
Hong Xiang

Harvard University:
Richard Wilson

INFN/Bari:
Raffaele de Leo

INFN/Roma:
Francesco Cusanno
Salvatore Frullani
Franco Garibaldi
Guido Maria Urciuoli

INFN/Roma, gruppo collegato Sanita:
Evaristo Cisbani

INFN/Roma2:
Rachel di Salvo

INFN/Roma3:

Mauro Iodice

Institut de Physique Nucleaire:
Louis Bimbot

ISN Grenoble:
Serge Kox
Gilles Quemener
Jean Mougey
Eric Voutier

Jefferson Lab:
Alexandre Camsonne
Jian-Ping Chen
Kees de Jager
Ed Folts
Javier Gomez
Douglas Higinbotham
Mark K. Jones
Bert Manzlak
Bob Michaels
Noel Okay
Yves Roblin
Jack Segal
Mark Stevens
Vincent Sulkosky
Bogdan Wojtsekowski
Larry Cardman
Eugene Chudakov
Alexandre Deur
David Gaskell
Ole Hansen
Tanja Horn
John Lerose
David Meekins
Sirish Nanda
Lester Richardson
Arun Saha
Dennis Skopik
Riad Suleiman
Stephanie Tysor

Jozef Stefan Institute:
Miha Mihovilovic
Simon Sirca

Kent State University:
Bryon Anderson
Elena Khrosinkova
Richard Madey
Gerassimos G. Petratos
John Watson
Mina Katramatou
Elena Long
Mark Manley
Andrei Semenov

Kharkov Institute of Physics and Technology:
Oleksandr Glamazdin
Roman Pomatsalyuk
Viktor Gorbenko

Kharkov State University:
Pavel Sorokin

Lanzhou University:
Yi Zhang

Longwood University:
Tim Holmstrom

Los Alamos Laboratory:
Lei Guo
Han Liu
Xiaodong Jiang
Ming Xiong Liu

LPC Clermont-Ferrand France:
Pierre Bertin
Bernard Michel
Helene Fonvielle
Carlos Munoz Camacho

Mississippi State University:
Dipangkar Dutta

MIT:
Bill Bertozzi
Jin Huang
Andrew Pucket
Wang Xu
Shalev Gilad
Bryan Moffit
Nikos Sparveris
Xiaohui Zhan

MIT/Center for Theoretical Physics:
Cesar Fernandez Ramirez

Negev Nuclear Research Center:
Sharon Beck
Arie Beck

NIKHEF:
Jeff Templon

Norfolk State University:
Vina Punjabi

North Carolina Central University:
Benjamin Crowe
Branislav (Branko) Vlahovic

Northwestern University:
Issam Qattan
Ralph Segel

Ohio University:
Julie Roche

Old Dominion University:
Gagik Gavalian
Jeff Lachniet
Wendy Hinton
Larry Weinstein

Old Dominion University and LPC Clermont-Ferrand France:
Charles Hyde

Pacific Northwest National Lab:
Kathy McCormick
Brian Milbrath

Princeton University:
Ioannis Kominis

Regina University:
Alexander Kozlov

Renaissance Tech:
Robert Lourie
Joseph Mitchell
Paul Ulmer

Rutgers University:
Lamiaa El Fassi
Ron Gilman
Gerfried Kumbartzki
Ronald Ransome
Elaine Schulte

Saint Norbert College:
Michael Olson

Seoul National University:
Seonho Choi
Byungwuek Lee

Smith College:
Piotr Decowski

St Mary's University:
Adam Sarty

St Mary's University and Dalhousie University:
Jackie Glister

SUBATECH:
Jacques Martino

Syracuse University:
Zafar Ahmed
Richard Holmes
Abdurahim Rakhman
Paul A. Souder

Tel Aviv University:
Nathaniel Bubis
Eli Piasetzky
Ishay Pomerantz
Ran Sheyor

Temple University:
Sebastian Incerti
Zein-Eddine Meziani
Brad Sawatzky
Huan Yao

Tohoku University:
Kouichi Kino
Kazushige Maeda

Teijiro Saito
H. Tsubota
Tatsuo Terasawa

Universidad Complutense de Madrid (UCM):
Joaquin Lopez Herraiz
Maria Christina Martinez Perez
Luis Mario Fraile
Jose Udias Moinelo

Universitat Pavia:
Sigfrido Boffi

University of Glasgow:
John Annand
Dave Ireland
Dan Protopopescu
David Hamilton
Ken Livingston
Guenther Rosner

University of Illinois:
Ting Chang
Alan Nathan
Mike Roedelbronn
Areg Danagoulian
J.C. Peng

University of Illinois at Urbana Champaign:
Youcai Wang
Lindgyan Zhu

University of Kentucky:
Kalyan Allada
Chiranjib Dutta
Wolfgang Korsch
Dan Dale
Tim Gorringe
Piotr Zolnierczuk

University of Lund:
Kevin Fissum

University of Maryland:
Elizabeth Beise
Herbert Breuer
Nicholas Chant
Philip Roos
Fatiha Benmokhtar
George Chang
Harry Holmgren

University of Massachusetts, Amherst:
Krishna S. Kumar
Luis Mercado
Dustin McNulty

University of New Hampshire:
John Calarco
Maurik Holtrop
Karl Slifer
Bill Hersman
Mark Leuschner
Timothy Smith

University of Regina:
Ed Brash
Garth Huber

George Lolos — Zisia Papandreou

University of Saskatchewan:
Ru Igarashi — Norm Kolb

University of Science and Technology of China (USTC):
Yi Jiang — Hai-jiang Lu
Yunxiu Ye

University of South Carolina:
Mike Paolone — Steffen Strauch

University of Virginia:
Khem Chirapatpimol — Brandon Craver
Mark Dalton — Gordon D. Gates
Mitra Hashemi Shabestari — Ge Jin
Sudirukkuge Tharanga Jinasundera — Richard Lindgren
Nilanga Liyanage — Vladimir Nelyubin
Blaine Norum — Kent Paschke
Seamus Riordan — Oscar Rondon
Jaideep Singh — Ramesh Subedi
Kebin Wang — Xiaochao Zheng
Jiayao Zhou

Weizmann Institute of Science:
Guy Ron

Yamagata University:
Seigo Kato — Hiroaki Ueno

Yerevan Physics Institute:
Nerses Gevorgyan — Edik Hovhannisyan
Armen Ketikyan — Vahe Mamyan
Samvel Mayilyan — Artush Petrosyan
Albert Shahinyan — Hakob Voskanian

Past Members:
Mattias Anderson — Maud Baylac
Hachemi Benaoum — J. Berthot
Tim Black — Alexander Borissov
Vincent Breton — Zhengwei Chai
Pibero Djawotho — Kim Egiyan
Catherine Ferdi — Robert Feuerbach
Mike Finn — Oliver Gayou
Charles Glashausser — Brain Hahn
Riccardo Iommi — Stephanie Jaminion
Lisa Kaufman — James D. Kellie
Ameya Kolarkar — Kevin Kramer

Elena Kuchina
Serguei Kuleshov
Geraud Lavessiere
Antonio Leone
Meihua Liang
Justin McIntyre
Wilson Miller
Pierre Moussiegt
Roberto Perrino
Bodo Reitz
Rikki Roche
David Rowntree
Gary Rutledge
Marat Rvachev
Neil Thompson
Dan Watts
Jingdong Yuan
Jingdong Zhou

6 Publications

P. Solvignon *et al., Quark-Hadron Duality in Neutron (3He) Spin Structure*, PRL **101**, 182502 (2008), 0803.3845 [nucl-ex]

R. Subedi *et al., Probing Cold Dense Nuclear Matter*, Science **320**, 1476 (2008)

Geraud Laveissiere *et al., Virtual Compton Scattering and Neutral Pion Electroproduction in the Resonance Region up to the Deep Inelastic Scattering Region at Backward Angles*, PRC **79**, 015201 (2009), 0811.3867 [nucl-ex])

F. Cusanno *et al., High Resolution Spectroscopy 12NL by Electroproduction*, submitted to PRL, arXiv:0810.3853 [nucl-ex]

A. Shahinyan *et al., The Electromagnetic calorimeter in JLab Real Compton Scattering Experiment*, submitted to NIMA, arXiv:0704.1830

S. Marrone *et al., Performance of the Two Aerogel Cherenkov Detectors of the JLab Hall A Hadron Spectrometer*, submitted to NIMA, 0810.4639 [physics.ins-det]

E. Cisbani *et al., Upgrade of the proximity focusing RICH at JLab.*, Nucl. Instrum. Meth. **A595**, 44 (2008)

S. Malace, M. Paolone, and S. Strauch, for the Jefferson Lab Hall A Collaboration, *Medium Modifications from* $^4He(\vec{e}, e'\vec{p})^3H$, AIP Conf.Proc.1056:141-147,2008. e-Print: arXiv:0807.2252 [nucl-ex]

7 Theses

1. "*Precision Measurements of the Neutron Electric Form Factor at High Momentum Transfers*"
   Ameya Kolarkar, University of Kentucky

2. "*Study of the* $^{12}C(e,e'p)$ *Reaction in a Correlations Dominant Regime with* $Q^2 = 2.0$ $(\mathrm{GeV/c})^2$ *and* $x_B > 1$"
   Peter Monaghan, Massachusetts Institute of Technology

3. "*Polarization Transfer in* $^4He(\vec{e},e'\vec{p})^3H$"
   Michael Paolone, University of South Carolina

4. "*Measurements of the Electric Form Factor of the Neutron at* $Q^2 = 1.7$ *and* 3.5 GeV^2"
   Seamus Riordan, Carnegie Mellon

5. "*The Proton Elastic Form Factor Ratio* $\mu_p G_E^p/G_M^p$ *at Low* Q^2"
   Guy Ron, Tel Aviv University

6. "*The Generalized GDH Sum Rule and the Spin Structure of the Neutron*"
   Jing Yuan, Rutgers University